

STATUS OF THESIS

Title of thesis

Investigation of Thickened Supercritical Carbon Dioxide for Waterless Fracturing of Shale Formation

I MUHAMMED RASHIK MOJID

hereby allow my thesis to be placed at the Information Resource Center (IRC) of Universiti Teknologi PETRONAS (UTP) with the following conditions:

1. The thesis becomes the property of UTP
2. The IRC of UTP may make copies of the thesis for academic purposes only.
3. This thesis is classified as

Confidential

Non-confidential

If this thesis is confidential, please state the reason:

The contents of the thesis will remain confidential for _____ years.

Remarks on disclosure:

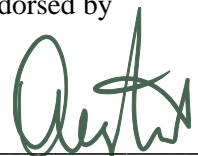


Signature of Author

Permanent address: 4-5, Batali road,
Ideal Niloy Tower, Flat-A8, Enayet
Bazar, Chittagong, 4000, Bangladesh

Date : 30/11/2021

Endorsed by



Signature of Supervisor

Name of Supervisor
Dr. Berihun Mamo Negash

Date : 06/Dec/2021

UNIVERSITI TEKNOLOGI PETRONAS

INVESTIGATION OF THICKENED SUPERCRITICAL CARBON DIOXIDE FOR
WATERLESS FRACTURING OF SHALE FORMATION

by

MUHAMMED RASHIK MOJID

The undersigned certify that they have read and recommend to the Postgraduate Studies Programme for acceptance this thesis for the fulfillment of the requirements for the degree stated.

Signature:

 06/Dec 2021.

Main Supervisor:

Dr. Berihun Mamo Negash

Signature:

 6 December, 2021

Co-Supervisor:

Dr. Shiferaw Regassa Jufar

Signature:



Head of Department:

Assoc. Prof. Dr. Khaled Abdalla Elraies

Date:

07/Dec/2021

INVESTIGATION OF THICKENED SUPERCRITICAL CARBON DIOXIDE FOR
WATERLESS FRACTURING OF SHALE FORMATION

by

MUHAMMED RASHIK MOJID

A Thesis

Submitted to the Postgraduate Studies Programme

as a Requirement for the Degree of

MASTER OF SCIENCE

DEPARTMENT OF PETROLEUM ENGINEERING

UNIVERSITI TEKNOLOGI PETRONAS

BANDAR SERI ISKANDAR,

PERAK

DECEMBER 2021

DECLARATION OF THESIS

Title of thesis

Investigation of Thickened Supercritical Carbon Dioxide for Waterless Fracturing of Shale Formation

I MUHAMMED RASHIK MOJID

hereby declare that the thesis is based on my original work except for quotations and citations which have been duly acknowledged. I also declare that it has not been previously or concurrently submitted for any other degree at UTP or other institutions.

Witnessed by



Signature of Author



Signature of Supervisor

Permanent address: 4-5, Batali road,
Ideal Niloy Tower, Flat-A8, Enayet Bazar,
Chittagong, 4000, Bangladesh

Name of Supervisor
Dr. Berihun Mamo Negash

Date : 30/11/2021

Date : 06-Dec-2024

DEDICATION

To my beloved parents and lovely wife.

ACKNOWLEDGEMENTS

I would like to say ALHAMDULILLAH for all those blessings I have been bestowed upon. The Almighty ALLAH has been very kind throughout my M.Sc. journey.

I would like to express my profound gratitude to my supervisor Dr. Berihun Mamo Negash for his tremendous support, noteworthy guidance, and valuable suggestions towards the accomplishment of my research. I am indebted to Universiti Teknologi PETRONAS (UTP) for providing me financial support through Graduate Research Assistantship (GRA) and research facilities to continue the research journey smoothly. I like to thank the Centralized Analytical Laboratory (CAL) for assisting me in the characterization experiments of my research.

I am also grateful to my co-supervisor Dr. Shiferaw Regassa Jufar who spent a significant amount of time guiding my work. I am eternally thankful to my friend Babatunde Kawthar Adewumi for her constant encouragement and support over the last two years. I would also like to felicitate my parents, wife, teachers, and friends for their inspiration and support.

ABSTRACT

Much attention is given to supercritical carbon dioxide (Sc-CO₂) as a fracturing fluid for hydrocarbon recovery from shale. However, poor proppant carrying capacity, high frictional resistance, large displacement, and sand plugging have limited its application. This research aims to investigate the thickening of Sc-CO₂ by using viscoelastic surfactants (VES) for increasing Sc-CO₂'s proppant carrying capacity using molecular simulation. It also stimulates the preferential adsorption of thickened Sc-CO₂ over methane (CH₄) to investigate potential sequestration. Shale samples from Eagle Ford, Mancos, and Wolfcamp formations are characterized by using field emission scanning electron microscope, surface area analyzer and porosimetry system, X-ray diffraction, helium porosimeter, and total carbon analyzer. The density, surface area, and volume of the shale samples range from 2.06 - 2.67 g/cm³, 368.8871 - 540.2255 m²/g, and 0.3515 - 0.4914 cm³/g, respectively. These results are used to validate a heterogeneous shale model which was developed to carry out adsorption simulation studies. A molecular simulation study on the thickening of Sc-CO₂ was carried out at temperatures and pressures ranging from 298 K to 305 K and from 100 kPa to 7400 kPa, respectively. Fluorinated VES, N-ethyl perfluorooctyl sulfonamide (N-ETFOSA), and non-fluorinated VES, N,N,N'-Trimethyl-1,3-propanediamine (N,N,N'-TM-1,3-PDA) were used as thickening agents. As a result, N,N,N'-TM-1,3-PDA shows better solubility in Sc-CO₂ than N-ETFOSA. However, N,N,N'-TM-1,3-PDA increases the viscosity of Sc-CO₂ by 36 times while N-ETFOSA increases the viscosity of Sc-CO₂ by 156 times. Moreover, the adsorption study has shown that the selectivity of N-ETFOSA thickened Sc-CO₂ at higher pressure and temperature is better than methane and N,N,N'-TM-1,3-PDA thickened Sc-CO₂ as well. In addition, both thickening and adsorption simulation results were validated using literature data. In conclusion, the results indicate that thickened Sc-CO₂ has the potential to become a viable alternative to the conventional water-based fracturing fluid.

ABSTRAK

Banyak perhatian telah diberikan kepada karbon dioksida superkritikal (Sc-CO₂) sebagai cecair peretakan untuk perolehan hidrokarbon dari syal. Walau bagaimanapun, keupayaan tampung proppant yang lemah, rintangan geseran yang tinggi, sesaran yang besar, dan penyumbatan pasir telah menghadkan aplikasinya. Penyelidikan ini bertujuan untuk mengkaji pemekatan Sc-CO₂ dengan menggunakan surfaktan viscoelastik (VES) untuk meningkatkan keupayaan tampung proppant Sc-CO₂ menggunakan simulasi molekul. Ia juga dijangka mampu merangsang penjerapan Sc-CO₂ yang dipekatkan menjadi lebih utama daripada penjerapan metana (CH₄) untuk menyelidik potensi sekuestrasi. Sampel syal dari formasi Eagle Ford, Mancos, dan Wolfcamp dicirikan dengan menggunakan mikroskop elektron pengimbasan pancaran medan, penganalisis luas permukaan dan sistem porosimetri, pembelauan sinar-X, porosimeter helium, dan penganalisis jumlah karbon. Ketumpatan, luas permukaan, dan isipadu sampel syal masing-masing berkisar antara 2.06 - 2.67 g/cm³, 368.8871 - 540.2255 m²/g, dan 0.3515 - 0.4914 cm³/g. Dapatan ini digunakan untuk mengesahkan model syal heterogen yang kemudiannya dikembangkan untuk menjalankan kajian simulasi penjerapan. Kajian simulasi molekul mengenai pemekatan Sc-CO₂ dilakukan pada suhu dan tekanan masing-masing dari 298 K hingga 305 K dan dari 100 kPa hingga 7400 kPa. VES berfluorinasi, N-etil perfluorooctyl sulfonamide (N-ETFOSA), dan VES, N, N, N'-Trimethyl-1,3-propanediamine (N, N, N'-TM-1,3-PDA) digunakan sebagai agen pemekat. Hasilnya, N, N, N'-TM-1,3-PDA menunjukkan keterlarutan yang lebih baik dalam Sc-CO₂ daripada N-ETFOSA. Walau bagaimanapun, N, N, N'-TM-1,3-PDA meningkatkan kelikatan Sc-CO₂ sebanyak 36 kali ganda sementara N-ETFOSA meningkatkan kelikatan Sc-CO₂ sebanyak 156 kali ganda. Selain itu, kajian penjerapan menunjukkan bahawa kepilihan Sc-CO₂ yang dipekatkan dengan N-ETFOSA pada tekanan dan suhu yang lebih tinggi adalah lebih baik daripada metana dan Sc-CO₂ yang dipekatkan dengan N, N, N'-TM-1,3-PDA. Selain itu, hasil simulasi

pemekatan dan penyerapan telah disahkan menggunakan dapatan daripada kajian literatur. Kesimpulannya, dapatan menunjukkan bahawa Sc-CO₂ yang dipekatkan berpotensi menjadi alternatif yang sesuai sebagai cecair peretakan yang konvensional berasaskan air.

In compliance with the terms of the Copyright Act 1987 and the IP Policy of the university, the copyright of this thesis has been reassigned by the author to the legal entity of the university,

Institute of Technology PETRONAS Sdn Bhd.

Due acknowledgement shall always be made of the use of any material contained in, or derived from, this thesis.

© Muhammed Rashik Mojid, 2021

Institute of Technology PETRONAS Sdn Bhd

All rights reserved.

TABLE OF CONTENT

ABSTRACT.....	vii
ABSTRAK.....	viii
LIST OF FIGURES	xiv
LIST OF TABLES.....	xvii
NOMENCLATURE	xviii
CHAPTER 1 INTRODUCTION.....	1
1.2 Problem Statement.....	6
1.3 Research Objectives.....	7
1.4 Scope of the Study	7
1.5 Research Significance.....	8
1.6 Outline of the Thesis.....	9
CHAPTER 2 LITERATURE REVIEW	10
2.1 Introduction	10
2.2 Waterless Fracturing Technologies	10
2.2.1 Fracturing by Liquified Petroleum Gas (LPG).....	11
2.2.2 Fracturing by Liquified Natural Gas (LNG)	14
2.2.3 Fracturing by Foam.....	15
2.2.4 Fracturing by Liquid Nitrogen.....	20
2.3 Carbon Dioxide Fracturing Technologies.....	22
2.3.1 Fracturing by Carbon Dioxide.....	22
2.3.2 Fracturing by Supercritical Carbon Dioxide	26
2.4 Factors Affecting Supercritical Carbon Dioxide Fracturing	29
2.4.1 Low viscosity and Proppant Carrying Capacity	29
2.4.2 High Frictional Pressure.....	30
2.4.3 Fast Filtration Loss and Large Displacement.....	31
2.4.4 Preferential Adsorption over Methane	31
2.5 Comparison of Waterless Fracturing Technologies	32
2.6 Viscoelastic Surfactants for Supercritical Carbon Dioxide Fracturing	37
2.7 Molecular Dynamic Simulation of Adsorption	38
2.7.1 Adsorption.....	39

2.7.2 Molecular Simulation Study of Methane and Carbon Dioxide	
Adsorption	42
2.8 Carbon Dioxide Sequestration on Shale	43
2.9 Summary and Recommendations	50
CHAPTER 3 RESEARCH METHODOLOGY	51
3.1 Introduction	51
3.2 Shale Samples	53
3.3 CO ₂ , CH ₄ , and Surfactants Model	54
3.4 Characterization of Shale Samples	55
3.4.1 Imaging and Qualitative Analysis Using FESEM	56
3.4.2 Mineralogy determination using XRD	57
3.4.3 Micro Surface Area and Micro Pore Volume Determination using SAP	59
3.4.4 Porosity Measurement using Helium Porosimeter	60
3.4.5 Total Organic Carbon (TOC) Measurement	62
3.5 Molecular Simulation and Modelling	62
3.5.1 Basic Molecular Simulation	63
3.5.2 Molecular Shale Model Preparation	64
3.5.2.1 Molecular shale model	64
3.5.2.2 Simulation details	66
3.5.3 Viscosity Enhancement of Sc-CO ₂ using VES	68
3.5.3.1 Solubility screening of VES in Sc-CO ₂	68
3.5.3.2 Viscosity measurement	69
3.5.3.3 Experimental validation of viscosity simulation	70
3.5.4 Adsorption Simulation Details	71
3.5.4.1 Adsorption simulation	71
3.5.4.2 Experimental validation of adsorption simulation	71
3.6 Summary	72
CHAPTER 4 RESULTS AND DISCUSSION	73
4.1 Introduction	73
4.2 Characterization of Shale Samples and Model Validation	73
4.2.1 Imaging and Qualitative Analysis and Mineralogy Evaluation	74

4.2.2 Elemental Analysis	80
4.2.3 Micro Surface Area and Micro Pore Volume determination	81
4.2.4 Porosity and Density Measurement	82
4.2.5 Total Organic Carbon (TOC)	83
4.3 Molecular Simulation and Modelling	84
4.3.1 Forcefield Validation	84
4.3.2 Viscosity Enhancement of Carbon Dioxide using Viscoelastic Surfactant	85
4.3.2.1 Solubility screening of VES in Sc-CO ₂	85
4.3.2.2 Viscosity calculation	86
4.3.2.3 Experimental validation of viscosity simulation	88
4.3.3 Adsorption Simulation	90
4.3.3.1 Adsorption of thickened carbon dioxide	90
4.3.3.2 Experimental validation of adsorption simulation	96
4.3.4 Isotheric Heat of Thickened Carbon Dioxide	98
4.3.5 Selectivity of Thickened Carbon Dioxide over Methane	99
4.4 Summary	100
CHAPTER 5 CONCLUSIONS AND RECOMMENDATIONS	101
5.1 Conclusions	101
5.2 Recommendations	103
LIST OF PUBLICATIONS	104
REFERENCES	105

LIST OF FIGURES

Figure 1.1: Technically recoverable shale gas around the globe	2
Figure 1.2: Production profile of shale gas in the USA [10, 11]	2
Figure 1.3: Different stages of conventional fracturing	3
Figure 1.4: Flowchart of problems associated with supercritical CO ₂ fracturing.....	4
Figure 2.1: Comparison between the effective length of fracture of hydraulic and LPG fracturing [45].....	13
Figure 2.2: Hydraulic fracturing with foam up to 98% in quality [48].....	16
Figure 2.3: Schematic diagram of liquid N ₂ fracturing [58]	20
Figure 2.4: Conceptual mechanism of carbon dioxide injection in shale reservoirs [70]	24
Figure 2.5: Phase diagram of carbon dioxide	26
Figure 2.6: Schematic diagram of Sc-CO ₂ fracturing for improved shale gas recovery and sequestration of CO ₂ [93].....	28
Figure 2.7: Publication count related to waterless fracturing fluids from the Scopus database	33
Figure 2.8: Adsorption isotherm types according to BET classification [124]	41
Figure 2.9: Publication count related to CCS from the Web of Science database	44
Figure 2.10: Schematic of carbon dioxide trapping mechanisms over time [132]	45
Figure 2.11: Active countries with CCS program [132]	49
Figure 3.1: Flowchart of the overall methodology	52
Figure 3.2: Shale samples from Eagle ford, Mancos, and Wolfcamp formation in powder form	53
Figure 3.3: 3D structures of (a) Sc-CO ₂ , (b) CH ₄ (c) N-ethyl perfluorooctyl sulfonamide, and (d) N,N,N'-Trimethyl-1,3-propanediamine (where red, grey, white, blue, yellow and paste ball represent oxygen, carbon, hydrogen, nitrogen, sulfur and fluorine respectively)	54
Figure 3.4: Flowchart of experimental methodology.....	55
Figure 3.5: Field emission scanning electron microscopy (SUPRA 55VP).....	57
Figure 3.6: Schematic diagram of a typical FESEM [158]	57

Figure 3.7: X-Ray powder diffraction machine	58
Figure 3.8: Schematic diagram of a typical XRD [159]	58
Figure 3.9: Surface area analyzer and porosimetry system	59
Figure 3.10: Schematic diagram of a typical SAP [160]	60
Figure 3.11: Helium Porosimeter	61
Figure 3.12: Schematic diagram of helium porosimeter [162]	61
Figure 3.13: Total organic carbon analyzer	62
Figure 3.14: A basic molecular dynamic simulation cycle.....	64
Figure 3.15: Structural unit cell of (a) kerogen type II D [164], (b) montmorillonite, (c) illite, and (d) quartz	65
Figure 3.16: Final shale model in layers.....	66
Figure 3.17: Sequential of building heterogeneous shale in Materials Studio environment.....	68
Figure 4.1: FESEM images of (a) EF-1, (b) EF-2, (c) MC, and (d) WF shale samples in 7K and 10K magnification (left to right) respectively	77
Figure 4.2: EDX spectra of (a) EF-1, (b) EF-2, (c) MC, and (d) WF shale samples showing elemental composition with an embedded FESEM images.....	79
Figure 4.3: The pore size distribution of (a) EF-1, (b) MC, and (c) WF shale samples	82
Figure 4.4: Peak graph of TOC of (a) EF-1, (b) EF-2, (c) MC, and (d) WF shale samples.....	83
Figure 4.5: TOC percentage of shale samples	84
Figure 4.6: An amorphous cell of the mixture of (a) Sc-CO ₂ and N-ethyl perfluorooctyl sulfonamide, and (b) Sc-CO ₂ and N,N,N'-Trimethyl-1,3- propanediamine.	86
Figure 4.7: Viscosity as a function of shear rate at 305 K and 7400 kPa	88
Figure 4.8: Viscosity variation with increasing pressure at 380, 400, and 420 k temperature.....	90
Figure 4.9: Adsorption isotherm of (a) thickened CO ₂ using N-ETFOSA and CH ₄ , (b) thickened CO ₂ using N,N,N'-TM-1,3-PDA, and CH ₄ , and (c) CO ₂ , thickened CO ₂ using N-ETFOSA, thickened CO ₂ using N,N,N'-TM-1,3-PDA, and CH ₄ on molecular shale model (Langmuir fitting is represented by the line).....	93

Figure 4.10: Adsorption isotherm of (a) thickened CO₂ using N-ETFOSA and CH₄, (b) thickened CO₂ using N,N,N'-TM-1,3-PDA, and CH₄, and (c) CO₂, thickened CO₂ using N-ETFOSA, thickened CO₂ using N,N,N'-TM-1,3-PDA, and CH₄ on type II-D kerogen model (Langmuir fitting is represented by the line).95

Figure 4.11: Comparison of the excess adsorption capacity of (a) CH₄, and (b) CO₂ on shale samples between simulation results and experimental results.....97

Figure 4.12: Isothermic heat on molecular shale model.....98

Figure 4.13: Thickened CO₂/CH₄ selectivity on molecular shale model 100

LIST OF TABLES

Table 2.1: Development of foam fracturing fluid technology [45]	18
Table 2.2: Typical Formation Data for Fracturing in West Virginia Devonian Shale and Eastern Kentucky Berea [49].....	19
Table 2.3: Typical Fracturing Design for West Virginia Devonian Shale and Eastern Kentucky Berea [49].....	19
Table 2.4: Fracture characteristics computed for typical designs of Table 2 [49]	19
Table 2.5: Effect of Stimulation Method on Gas Production from the Big Sandy reservoir [73].....	24
Table 2.6: Required parameters for field test [102]	31
Table 2.7: Comparison of the viscosity of water and supercritical carbon dioxide at reservoir condition [102]	31
Table 2.8: Comparison of waterless fracturing fluids	34
Table 2.9: Summary of recent advancements in fracturing	35
Table 2.10: Chemical reactions between minerals acidified CO ₂ water [136]	46
Table 2.11: Physical and chemical approaches to CCS [146]	47
Table 4.1: Mineralogy of shale samples	78
Table 4.2: The experimental and simulated weight percentage of elements	80
Table 4.3: Surface area and cumulative volume of shale samples and shale model... ..	82
Table 4.4: Experimental and simulated matrix density	83
Table 4.5: The viscosity of different structures using Forcite Shear simulation.	87
Table 4.6: Comparison of experimental and simulated viscosity	89
Table 4.7: Langmuir fitting parameters for (a) CH ₄ and Thickened CO ₂ using N-ethyl perfluorooctyl sulfonamide, and (b) CH ₄ and Thickened CO ₂ using N,N,N'-Trimethyl-1,3-propanediamine adsorption on molecular shale model.	96
Table 4.8: Average and limit isosteric heat of CH ₄ , CO ₂ , and thickened CO ₂ on molecular shale model	99

NOMENCLATURE

Abbreviations

2D	Two Dimensional
3D	Three Dimensional
Al	Aluminum
BET	Brunauer Emmet Teller
C	Carbon
Ca	Calcium
CCS	Carbon Capture and Sequestration
CO ₂	Carbon Dioxide
CH ₄	Methane
DNA	Deoxyribonucleic Acid
EDX	Energy Dispersive X-Ray Analysis
EF-1	Eagle Ford-1 Shale Sample
EF-2	Eagle Ford-1 Shale Sample
EIA	Energy Information Agency
Fe	Iron
FESEM	Field Emission Scanning Electron Microscope
H	Hydrogen
H ₂ O	Water
HFDA	Heptadecafluorodecyl Acrylate
K	Potassium
LNG	Liquified Natural Gas
LPG	Liquified Petroleum Gas
MC	Mancos Shale Sample
MDS	Molecular Dynamics Simulation

Mg	Magnesium
MMT	Montmorillonite
MSDS	Material Safety Data Sheet
N ₂	Nitrogen
N-ETFOSA	N-Ethyl Perfluorooctyl Sulfonamide
N,N,N'-TM-1,3-PDA	N,N,N'-Trimethyl-1,3-Propanediamine
NPT	Isobaric Isothermal Ensemble (keeping N, P, T constant)
NPV	Net Present Value
NVT	Canonical Ensemble (keeping N, V, T constant)
O	Oxygen
PME	Particle Mesh Ewald
PS	Saturation Pressure
S	Sulphur
SAP	Surface Area Analyzer and Porosimetry System
Sc-CO ₂	Supercritical Carbon Dioxide
Si	Silicon
SRV	Stimulated Reservoir Volume
SV	Selectivity
TC	Total Carbon
TIC	Total Inorganic Carbon
TOC	Total Organic Carbon
USA	United States of America
VBe	Vinyl Benzoate
VES	Viscoelastic Surfactants
WF	Wolfcamp Shale Sample
WML	Wormlike Micelles
XRD	X-Ray Diffraction

Expressions

ρ	Density
a	Acceleration
b	Langmuir Constant

C	Ratio of $\frac{K_1}{K_L}$
E	Constant Energy
E ₁	Heat of Adsorption for 1 st Layer
E _L	Heat of Liquefaction for Rest of the Layers
F	Force
H	Constant Enthalpy
K ₁	Constant of Equilibrium when Each Vacant Site Adsorb Single-Molecule
K _L	Equilibrium Constant to the Saturated Vapor-Liquid Equilibrium
k & n	Constant Values Dependent on Gas and Adsorbent at Temperature
M	Molar Mass of the Gas
N	Constant Number of Molecules
n ^a	Absolute Adsorption Capacity
n ^a _{max}	Langmuir Maximum Adsorption Capacity
n _{ab}	Absolute Adsorption
n _{ex}	Excess Adsorption
P	Pressure/Constant Pressure
P _c	Critical Pressure
SA _{FiB}	Breakthrough Surface Area
T	Temperature/Constant Temperature
T _c	Critical Temperature
V	Volume/Constant Volume
v	Velocity/Speed
V _{mono}	Volume of Adsorbed Gas to Cover Unilayer Surface at High Pressure
V _{gas}	Gas Volume
V _{total}	Total Volume
Units	
Å	Angstrom

°C	Degree Celcius
°F	Degree Fahrenheit
>	Greater than
<	Less than
µm	Micrometer
%	Percent
bbl	Barrel
BPM	Barrel per Minute
cm	Centimeter
cm ²	Centimeter Square
cm ³	Cubic Centimeter
cP	Centi Poise
fs	Femtosecond
ft	feet
ft ²	Square Feet
g	Gram
g/cm ³	Gram per Cubic Centimeter
GT	Giga Tonne
in	Inches
K	Kelvin
Kg/m ³	Kilogram per Cubic Meter
kPa	Kilo Pascal
Kg/ton	Kilogram per Tonne
lb	Pound
m	Meter
m ²	Meter Square
m ² /g	Meter Square per Gram
m ³	Cubic Meter
mD	Milli Darcy
Mgal	Mega Gallon
min	Minute
mL	Milli Litre

mm	Millimeter
MMcf	Million Cubic Feet
mmol/g	Millimole per Gram
MPa	Mega Pascal
mPa-s	Millipascal-Seconds
Mt/year	Mega Tonne per Year
nm	Nano meter
ns	nanosecond
ps	Picosecond
psi	Pound per Square Inch
s	Second
scf	Standard Cubic Feet
tcf	Trillion Cubic Feet

CHAPTER 1

INTRODUCTION

1.1 Background

The energy crisis has been a huge challenge for many nations globally. Due to depleting conventional resources and increased world demand for energy, there is an urge to produce more from unconventional resources such as shale gas, tight gas, and coal seam gas. Low matrix permeability is the most common characteristic of these unconventional reservoirs [1]. Of the unconventional resources, shale gas is the most abundant hydrocarbon. Shale formations are characterized by thin grains and thin lamina breaking with an irregular curving fracture parallel to the bedding plane [2].

The United States Energy Information Agency (EIA) estimated that unconventional shale reservoirs in the United States of America and China have 827 and 1115 trillion cubic feet (tcf) of recoverable natural gas respectively [3-5]. Figure 1.1 gives a vivid picture of technically recoverable shale gas around the world [6] where Figure 1.2 indicates a steady rise in the production profile of shale gas in the United States of America from the year 1999 to 2019. In 2011, the worth of shale gas in the USA was \$34 billion whereas in 2020 the dry shale gas production of the USA was 26.3 tcf which is almost 79% of the total natural gas production [7]. Shale gas is considered a viable route for transforming fossil fuels from high-carbon energy resources into low-carbon energy resources [8, 9].

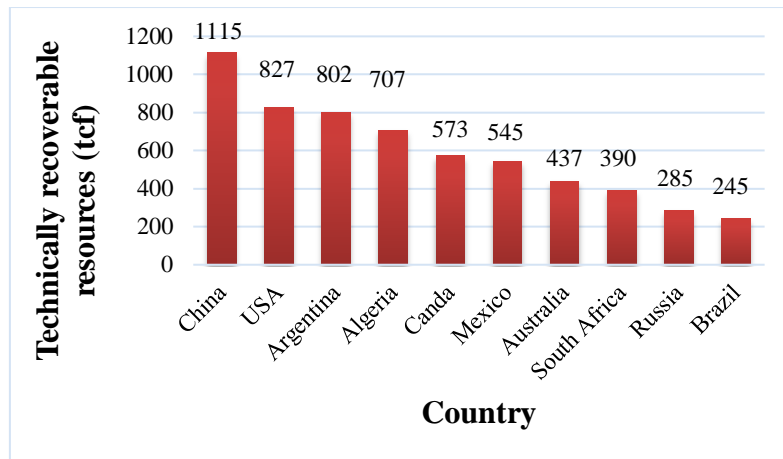


Figure 1.1: Technically recoverable shale gas around the globe

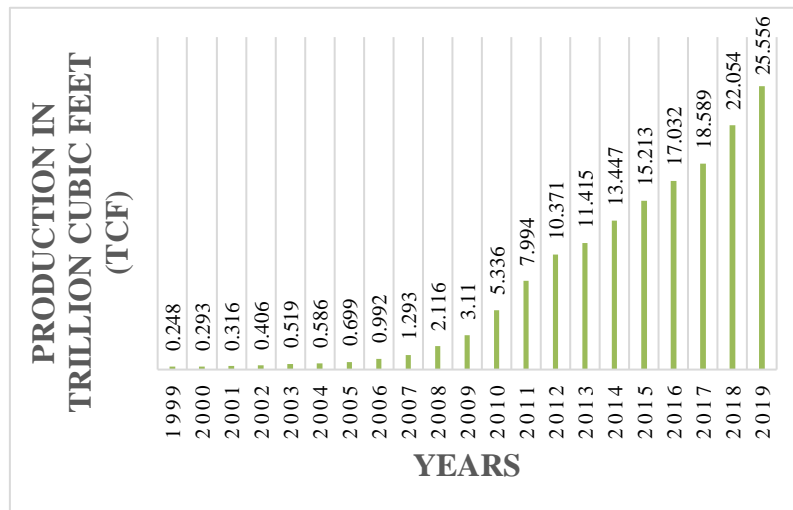


Figure 1.2: Production profile of shale gas in the USA [10, 11]

Undoubtedly, hydraulic fracturing has transformed the exploitation of unconventional oil and gas resources. It is based on pumping pressurized fracturing fluid at higher flow rates into the reservoir. The fracturing fluid contains proppants and chemical additives. Figure 1.3 demonstrates the different stages of conventional hydraulic fracturing. Initially, fracturing fluid is hydraulically pumped in stages into the formation via perforations. Then a fluid carrying proppants is pumped to keep the fractures open. The efficiency of the fracturing fluid directly influences the production rate and resulting in fracturing effects.

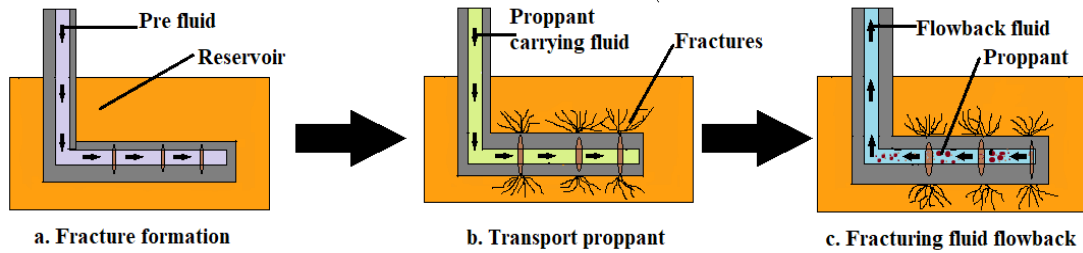


Figure 1.3: Different stages of conventional fracturing

Hydraulic fracturing has undergone many advances and is also widely used in many regions of the world to extract natural gas from tight formations [12, 13]. Despite these enormous economic benefits and wide application globally, conventional hydraulic fracturing fluids are encumbered with several problems [14]. Significant damage to the formation develops capillary end effects which reduce the production rate and recovery efficiency. Fracturing can also lead to mineral hydration and water imbibition. These cause a cutback in effective permeability and increase clay swelling. Inappropriate dumping and treatment of a huge volume of flowback fluids containing chemical additives is another major drawback of hydraulic fracturing. According to the statistics derived from all over the USA in 2014, based on the number of wells drilled in different unconventional reservoirs, a yearly median water volume of 19425 and 15275 m³ are required for hydraulic fracturing in horizontal gas and oil wells, respectively [15]. Hence, hydraulic fracturing becomes troublesome for formations with a higher margin of clay material, of huge burial depth, and areas with a water deficiency [16, 17].

These drawbacks have triggered the search for new fracturing fluids and methods. The most common waterless fracturing fluids are gelled Liquefied Petroleum Gas (LPG), Liquefied Natural Gas (LNG), liquid Carbon dioxide (CO₂), and liquid nitrogen (N₂). Waterless fracturing has significant benefits over the hydraulic fracturing method. In waterless fracturing, there can be a minimal fluid loss that implies a nearly hundred percent recovery of the fracturing fluids. LPG and LNG are mutually soluble with hydrocarbon, these will be fully compatible with reservoirs. Similarly, minimal formation damage and rapid clean-up after fracturing are two main advantages related to waterless fracturing by liquid CO₂. Besides, cryogenic fracturing by an inert gas such as liquid N₂ reduces the cost of reservoir stimulation. In addition, the absence of water in waterless fracturing methods excludes the possibility of rock swelling and water

Many researchers used organic compounds which combine in solution to "thicken" carbon dioxide. The initial endeavor of CO₂ thickening was unsuccessful as a result of low CO₂ solubility in conventional organic polymers, organometallic compounds, and ammonium carbamates [19]. At 50°C, 6.7 weight % of poly (1,1-dihydro-perfluorooctyl acrylate) was soluble in carbon dioxide and provided a significant increase in CO₂ viscosity from 0.08 to 0.2-0.6 cP [22]. This was the first successful attempt at CO₂ thickening. However, since filter cake is formed by polymer-based fluids, there have been evident formation damage and poor conductivity which limits its application. Moreover, researches show that cross-linked polymers cause severe damage to formation permeability [23, 24].

Viscoelastic surfactant (VES) is free of solids and has great viscosity. It exhibits viscous and elastic efficiency in brine and thus increases the viscosity by VES micelles entanglement, but at high-temperature viscosity is lessened considerably. At a condition of high temperature and pressure, added inorganic/organic nanoparticles have been found to help stabilize the viscosity of these VES fluids. Adding internal breakers to the viscoelastic surfactants helps to break the fluid into low viscosity fluid once the fracturing operation is completed and also to ease the flow-back of viscoelastic surfactant to the surface [20]. Thus it presents very few cleanup issues of formation fractures compared with polymer-based fracturing fluids [25]. It retains the desirable characteristics of viscoelastic surfactant fluids to make big effective half-lengths through higher retained conductivity, great proppant carrying capacity, less friction pressure, and simple operational procedure [26].

Molecular dynamics simulation (MDS) is a computer simulation technique where the evolution of time of a set of interacting atoms is followed by integrating their equations of motion. In recent times, MDS has been used to understand and explain phase behavior, fluid behavior under confinement, fluid-fluid interaction, and shale mineral interaction with fluids. Adsorption studies of carbon dioxide and methane have been carried out using MDS. However, variation of the experimental adsorption and the simulation adsorption data has been noted in several works [27]. These variations occur due to the differences in shale components present in the molecular model used.

In 2020 Chen et al. expressed the urge to research the adsorption using molecular models incorporating both organic and inorganic nanopores [28].

To eradicate this research gap, a dry heterogeneous molecular shale model consisting of kerogen type II D, montmorillonite (MMT), illite, and quartz model has been proposed in this study. Moreover, to validate this molecular shale model characterization of actual shale samples from Eagle ford (EF-1, EF-2), Mancos (MC), and Wolfcamp (WF) formations has also been carried out. Furthermore, VES such as N-ethyl perfluorooctyl sulfonamide has been used to increase the viscosity of Sc-CO₂. These VES are selected on extensive literature review and having the higher presence of fluorine which has high carbon affinity. N,N,N'-Trimethyl-1,3-propanediamine a non-fluorinated CO₂ soluble VES has also been used in this study to compare with the result of viscosity enhancement using N-ethyl perfluorooctyl sulfonamide. Molecular simulation of the adsorption study of thickened Sc-CO₂ and CH₄ has also been performed on the molecular shale model.

1.2 Problem Statement

CO₂ achieves its supercritical state over the point of critical pressure, $P_c = 1070.38$ psi and critical temperature, $T_c = 31.05^\circ\text{C}$. However, Sc-CO₂ exhibits the same viscosity as its gaseous state which ranges from 0.003 cP to 0.10 cP which impedes its proppant carrying capacity. Moreover, this low viscosity of Sc-CO₂ results in the closure of the fractures soon after the fracturing operation is completed. This entirely fails the aim of the fracturing and overall hydrocarbon recovery is reduced to a great extent. Therefore, there is a need to thicken the Sc-CO₂ to ensure good proppant carrying capacity. Polymeric thickeners and cationic surfactants are used as thickeners to increase the viscosity of Sc-CO₂. Nonetheless, under the effect of mechanical shear or breakage of chemical bonds of long polymeric chains, polymeric thickeners degrade and contribute to loss of viscosity. Moreover, cationic surfactants tend to have high toxicity and very low biodegradability. Thus, there prevails a research gap in the thickening of Sc-CO₂.

Molecular simulation studies from literature shows that shale was represented by organic and inorganic single components such as kerogen, and montmorillonite.

However, models incorporating organic and inorganic matters kept those at opposite end of the slit pore without combining them. This means the minerals are not mixed nor interacting with each other but rather they exist at different ends of the slit pore. Therefore, variation between the experimental and the simulation adsorption data prevailed. Although, CO₂ is preferentially adsorbed in the shale surface before methane, the preferential adsorption behavior of thickened Sc-CO₂ is not clearly understood. Moreover, commonly used simple isotherm adsorption models often may not accurately fit the adsorption data of Sc-CO₂. Besides, the adsorption study of thickened Sc-CO₂ in shale requires great attention as it paves the way for CO₂ sequestration in the shale formation.

Therefore, the viscosity and preferential adsorption-related issues of Sc-CO₂ are necessary to be studied. This study fills the gap by investigating the thickening of Sc-CO₂ using viscoelastic surfactants and the preferential adsorption of thickened Sc-CO₂ over methane on shale.

1.3 Research Objectives

1. To develop a realistic heterogeneous shale model in a molecular environment and validate it by characterizing the physical properties of actual shale samples.
2. To investigate the thickening of supercritical carbon dioxide by using viscoelastic surfactants.
3. To analyze the preferential adsorption of thickened supercritical carbon dioxide over methane on molecular shale model using molecular dynamics simulation.

1.4 Scope of the Study

In this study, Field-Emission Scanning Electron Microscope (FESEM), X-Ray Diffraction (XRD), surface area analyzer and porosimetry system, Helium Porosimeter and TC analyzer has been used to characterize the shale samples. A heterogeneous

molecular shale model consisting of organic matter (kerogen type II D), clay minerals (montmorillonite, and illite), and non-clay minerals (quartz) have been developed using molecular dynamic simulation (MDS) and its properties have been validated by characterization results of actual shale samples. The shale model has the cell parameters $a=30.07 \text{ \AA}$, $b=30.07 \text{ \AA}$, and $c=119.17 \text{ \AA}$ and a slit pore of 50 \AA . Although shale consists of many other clay and non-clay minerals, this study does not consider all minerals due to its complexity and time-consuming simulations. The thickening simulation of supercritical CO_2 with two VES (N-ethyl perfluorooctyl sulfonamide and N,N,N'-Trimethyl-1,3-propanediamine) in the molecular level is carried out at 298 K to 305 K temperature and 100 kPa to 7400 kPa pressure to investigate the change in its viscosity thus better proppant carrying capacity. A loading ratio of 10:1 has been used for the mixture of Sc- CO_2 and VES. Moreover, adsorption simulation has been studied using thickened supercritical carbon dioxide and methane on the heterogeneous molecular shale model at a temperature of 305 K and pressure ranging from 10 kPa to 7400 kPa. Temperature and pressure in both thickening and adsorption simulations are considered up to the mentioned range as these resemble the supercritical condition for CO_2 and higher temperature and pressure require high computational time. Thickening and adsorption simulations have been validated using literature data from Xiong et al., Rexer et al., and Liu et al, respectively. The current study will pave the way for insightful future directions to the implementation of supercritical CO_2 as an alternative to the conventional hydraulic fracturing fluid.

1.5 Research Significance

This research can help to further improve Sc- CO_2 fracturing in terms of technological advances to establish it as a better alternative to predominant water-based fracturing. The enhancement of the low viscosity of Sc- CO_2 will increase its proppant carrying capacity and opening period of fractures after the fracturing operations. Furthermore, CO_2 is known as the prominent cause of global warming. Adsorption study of thickened Sc- CO_2 will also provide a theoretical ground of geologic sequestration of CO_2 in shale reservoirs. Therefore, the improved gas recovery and CO_2 sequestration can be achieved by using Sc- CO_2 based fracturing, and economic

feasibility may also be well justified. Thus, this research can contribute to a great extent in terms of green and sustainable technology.

1.6 Outline of the Thesis

The work is divided into five chapters. In chapter 1, there is a brief description of problems related to Sc-CO₂ as fracturing fluid and the use of VES to eradicate the low proppant carrying capacity of Sc-CO₂. Chapter 2 is the review of previous works which is related to the waterless fracturing fluid. There is also a brief description of CO₂ sequestration on shale. The methodology used for experimental and simulation study is in chapter 3. The results and discussions are mentioned in chapter 4. Conclusion along with the recommendation for future study is summarized in chapter 5.

CHAPTER 2

LITERATURE REVIEW

2.1 Introduction

Water reservation, especially in remote and drought-prone areas and environmental concerns, are two major drawbacks of water-based fracturing. Waterless fracturing technologies, however, also referred to as green hydraulic fracturing, are friendly to the environment and have the potential to replace water-based fracturing. This article critically reviews such technologies. More attention is given to supercritical carbon dioxide (Sc-CO₂), as it is the most viable option with the potential to mitigate global warming. Waterless fracturing technologies cause minimal formation damage, have high fluid compatibility, increase production, exhibit a quick flowback rate, and utilize reusable materials. However, an in-depth understanding of the mechanisms and limitations of technologies is required to extract the maximum benefit and to de-risk projects. While some of the problems related to these technologies have been addressed, field-wide applications are yet challenging. Waterless fracturing technologies have high initial costs but, over a longer period, these technologies, in particular Sc-CO₂ fracturing fluid, offer excellent economic efficiency. However, poor proppant carrying capacity, high frictional resistance, high displacement, and easy sand plugging are problems associated with Sc-CO₂ fracturing. Trending research in the field of Sc-CO₂ fracturing involves an understanding of its adsorption in shale, developing the best fit adsorption isotherm, and increasing its viscosity to improve the carrying ability of the proppants.

2.2 Waterless Fracturing Technologies

The most common waterless fracturing fluids are gelled Liquefied Petroleum Gas (LPG), Liquefied Natural Gas (LNG), liquid Carbon dioxide (CO₂), and liquid nitrogen

(N₂). In the sub-sections of this section these waterless fracturing technologies have been described in detail.

2.2.1 Fracturing by Liquefied Petroleum Gas (LPG)

GasFrac Energy Services Inc., a North American-based company, started using LPG gel to stimulate tight shale reservoirs in 2007. Since then, more than 1500 applications of this technique have been carried out in Canada and the United States alone [18]. In LPG fracturing technology, propane is used as the standard high-pressure gas. Usually, LPG is gelled before fracturing, this facilitates the transportation of proppant into fractures. Fracturing LPG persists in its liquid form but vaporizes at the end of the operation and thus blends well with the gases in the reservoir [15, 29]. EcopStim company in Houston, Texas developed and promoted liquefied LPG technology as a new variant. The use of buoyant proppants such as fine sand and carbon fullerenes, in this variant, is modern technology and its application range needs to be investigated, analyzed, and proven [29].

Research on hydrocarbon-based fracturing fluid has been the focus of many USA researchers since the early 1970s. The LPG micellar solution was manufactured in 1974 and its utilization was also investigated by Gogarty and Haws [30]. In 1978, the gellification of LPG fracturing fluid was studied by Gay et al. [31]. In 1989, a new approach and material were proposed to develop an LPG gel by Huddleston. This hydrocarbon gel comprises of liquid hydrocarbon; a gelling agent consisting of a reaction product of (a) a polyphosphate intermediate produced by reacting triethyl phosphate and phosphorous pentoxide and (b) mixed alcohol comprising from about 13 percent to about 92 percent by weight hexanol; and an effective amount of an alkaline metal aluminate activator [32]. Gelled LPG can evenly distribute proppants due to its consistent and predictable viscosity. No special cooling or venting is required in LPG fracturing, so it is relatively cost-effective. Geib introduced a new type of hydrocarbon fracturing fluid enhancer in 2000. This new enhancer is composed of a non-nitrogen component known as alkyl amine and ether phosphate which improved viscosity and crosslinking time [33].

A type of coarse-grained solid wax gel-breaking agent, which remains solid at normal temperature and becomes soluble at subsurface temperature was invented by Acker in 2001 [34]. Dawson developed a slowed-down gel-breaking system in 2002 to trigger the gel breaker in the reservoir [35]. Inert gas was introduced into the LPG fracturing system by Loree in 2007 [36]. This breakthrough helped reduce the possibility of explosion and was a significant step towards the industrialization of low-carbon fracturing technology.

In McCully, Canada's first fracturing experiments were carried out in 2008 by using a hundred percent LPG [37]. The operation and the effect of the fracturing were good. From Figure 2.1 it can be inferred that the effective length of the fracture using LPG is above one hundred meters which is quite higher than the hydraulic fracturing fluid. GasFrac has developed a fracturing fluid that is made of LPG crosslinked gel and has been practiced in McCully gas-field situated in Canada. It has been reported that the effective length of fracture of LPG fracturing is two times greater than conventional fracturing [38]. Advanced Stimulation technologies company of the United States used the purest form of propane in its liquid state in the shale block of Eagle Ford formation in 2012. After the pilot test of fracturing operation, they proclaimed that stimulation at a depth of 5950 ft was safe and effective [39]. An LPG fracturing fluid together with a well-performing crosslinking agent was developed by Hou in 2013. The performance of this new crosslinking agent outperformed two common agents, namely, aluminum sulfate and ferric sulfate.

Recently, a noteworthy low carbon hydrocarbon-based phosphate gelling agent was found by Mao, and it exhibits strong shear and heat resistance. It also maintains good viscosity at temperatures of up to 150°C [40]. Hisham et al. listed mineral compositions, mechanical properties, distribution of natural fractures, and horizontal stress fields are the main geological factors to be taken into considerations [41]. Zhao et al. investigated the stimulated reservoir volume (SRV) in the FL shale reservoir and found $2.92 * 10^6 \text{ m}^3$ and $19.5 * 10^6 \text{ m}^3$ SRV for single-stage and multi-stage hydraulic fracturing and also estimated the average SRV of different wells $20\text{-}40 * 10^6 \text{ m}^3$ [42]. Zhang et al in 2018 carried out 4 large scale true tri-axial fracturing simulation experiments on shale outcrops and found that LPG fracturing provides not only a complex fracture network

by activating discontinuities but also long fracture length and large SRV [43] which are similar findings from the study of Soni, 2014 [44]. It is obvious by now that the prospect of LPG as a fracturing fluid is promising. Overall, technological advancements can make LPG more implementable in the field, but high initial costs, high flammability in nature, and low net present value in a short period are major hindrances to its economic viability.

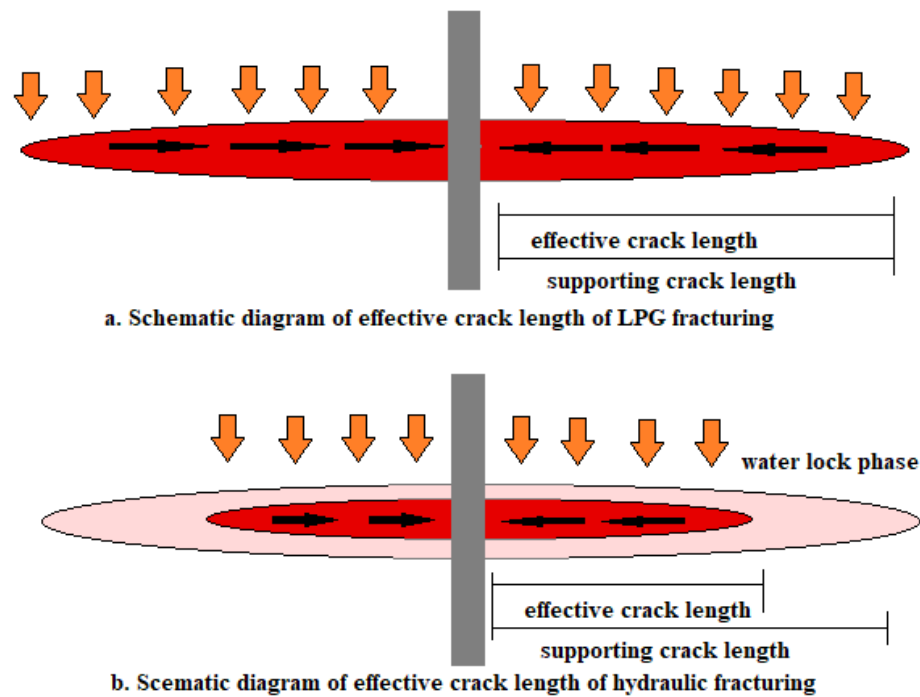


Figure 2.1: Comparison between the effective length of fracture of hydraulic and LPG fracturing [45]

During fracturing with LPG, there is low energy consumption because the density and viscosity of the fluid are low. Due to the high affinity of LPG with reservoir fluid and its low surface tension, there is no water phase trapping and clay expansion. Moreover, at high temperatures and pressure, the fractures exhibit great circulation time and provide enough space for vaporization. As a consequence, a free flow of gas, impeded only by the proppants, is expected. Using a simple separation process the flowback can be recycled as the flowback rate is high. Clean-up and initial well performance are also very high in the case of LPG fracturing in comparison to the conventional one [37]. It also decreases the need to flare the initial production from the well to clean up conventional fracturing fluids and thereby reducing CO₂ emissions. However, LPG is pumped at a higher pressure and reliquefaction is required after each

fracturing stage. Hence, the investment cost of LPG fracturing is very high when compared to the cost of conventional fracturing, and the cost of propane is also higher than conventional fluid as all the propane does not return to the surface after each fracturing operation [15]. As LPG is an explosive it must be stored in high-pressured tanks. In addition, LPG poses health hazards to animals and humans because it is thicker than air. Therefore, the possibility of accumulation and persistence at low ground points prevails. No such obvious geological or geochemical limitations are found in the literature which can limit the application of LPG fracturing technology.

2.2.2 Fracturing by Liquified Natural Gas (LNG)

In 2011 ENFRAC Inc. was the first to recognize LNG as a fracturing fluid. LNG is produced from natural gas obtained from several sources such as gas well and a pipeline. It is often stored in closed vessels at a temperature of -162°C for easy transportation to the well site [18]. LNG is like liquid N_2 (-196°C) but it is not fully anhydrous. Therefore, fracturing using LNG is not a completely waterless one but more of a water-diminishing fracturing method. Depending on the type of fluid added together with LNG, the percentage of the volume can differ. For instance, if LNG is combined with water only, it could constitute 50% of the total volume. On the other hand, if it is water-based foam the combined volume can be up to 60-95% or 10-70% volume if the fluid is oil-based. The conventional fluid slurry containing proppants is combined with LNG at the wellhead and then sent to the reservoir via wellbore. Thus, it hydraulically fractures the formation.

The hydrostatic pressure change is very close to friction pressure loss in this technology and as a result surface pressure is slightly lower than the bottom tubing pressure [18]. LNG also has a handling procedure like the well-established liquid N_2 handling. It is heated up to a temperature of 15°C and pressurized to less than 7000 psi for fracturing operation. The volume of LNG remains almost unchanged with increased pressure and temperature. LNG fracturing services and new technologies were explored by Linde at a workshop in Houston in 2013. Based on the solid experience of twelve long months, Twymon was persuaded that LNG as a fracturing fluid is safe, reliable, and cost-effective [45]. In the year 2014, Baker-Hughes filed a patent claiming they

invented a new technology for LNG fracturing using gelled LNG. This novel gelled LNG fracturing fluid consists of non-aqueous fluid containing proppants and phosphate ester as gellant [46]. Gatlin et al. developed a crosslinking portion for LNG fracturing in 2015, which they claim to be efficient at a very low temperature. Their findings indicate that the shearing of fracturing fluid and resistance to high temperature becomes strong when the length of the carbon chain is increased [47]. Becky suggested a novel foamed LNG-based fluid in 2017 and was then extensively tested in the laboratory [18].

There are many advantages to the use of LNG as a fracturing solvent. LNG being readily dissolved in reservoir hydrocarbon fluid; does not cause any harm to the structure. LNG is reusable without any treatment after the fracturing operation. High transportation cost is also offset as it can easily be found near well sites. However, LNG being a modern technology and possessed by a single service providing company there is quite a narrow scope to gather technical information about it. While numerous studies have been carried out on making a feasible LNG fracturing technology, there is no evidence of the implementation of these inventions in the field. Therefore, this new technology still cannot be referred to as a viable one on the ground of publications available to date. No such obvious geological or geochemical limitations are found in the literature which can limit the application of LNG fracturing technology.

2.2.3 Fracturing by Foam

Foam-based fracturing fluid is comprised of acid, gel, alcohol, oil, or linear glue as its dispersing medium and N₂, CO₂, or air as the dispersed medium. Foam fracturing fluid has a less aqueous phase compared to the conventional hydraulic fracturing fluid. Various additives are also added to the foam-based fracturing fluid. The quality of the foam is determined by the ratio of total gas volume to total foam volume. Higher quality foam has a higher viscosity. The interfacial structure of foam bubbles causes the foam to have high apparent viscosity. Foams used in foam-based fracturing fluid are within the quality range of (65-80)%, this aids the transportation of proppants. The foam also supports proppants after the creation of fractures. This results in a uniform distribution of proppant within the fracture.

Water usage in conventional hydraulic fracturing can be reduced by using ultra-dry foams. Figure 2.2 shows the overview of the synergies required for the stabilization and use of ultra-dry foams in hydraulic fracturing. Ultra-dry foams are classified as foams with 90% or higher volumetric gas content or quality. The purpose of using ultra-dry foam is to reduce or eliminate the water content of fracturing fluids.

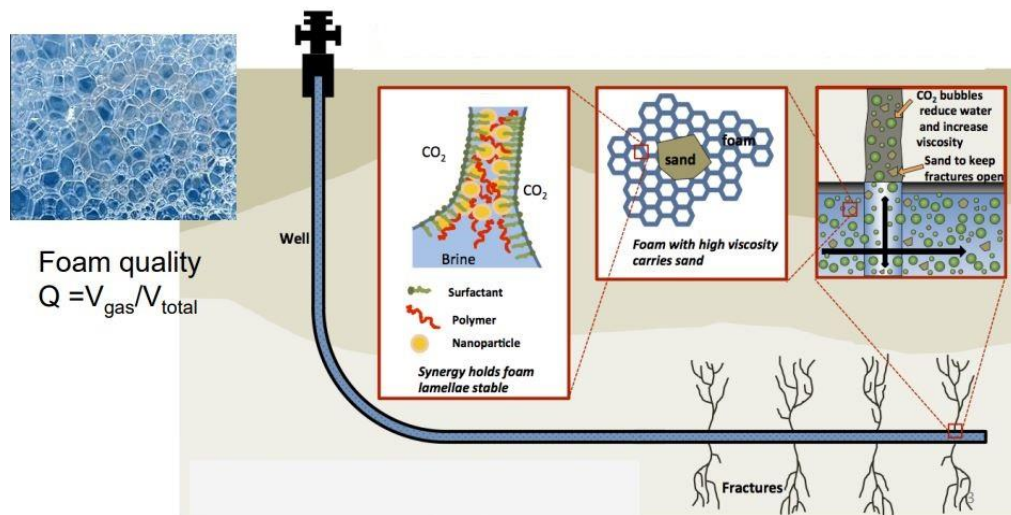


Figure 2.2: Hydraulic fracturing with foam up to 98% in quality [48]

Foam possesses good fluid loss properties for formations with low permeability. The absence of natural fractures eliminates the need for fluid loss additives. But the presence of high natural fractures requires coarse fluid loss additives such as 70/170 mesh sand as it helps to bridge natural fractures and newly created or extended fractures. A successful fracturing treatment in a formation becomes a general standard for that locality. The time length of fluid recovery is also different for the foam and gelled water. A well fractured with foam can be prepared for testing and production purposes in 2-3 days, while the well fractured with a gel can take a long time, along with some swabbing to be cleaned up.

The quality of a foam determines its characteristics during fracturing. For low-quality foams (<50% quality), the bubbles are spherical and have fewer restrictions from the adjacent bubbles, hence high freedom to move within the fluid. A quality of above 50% implies that the volume of gas is higher and that the bubbles are more likely to encounter neighboring bubbles and surrounding fluid. As a result, the foam bubbles

have less chance of movement. Similarly, quality higher than 75% will result in crowded foams with no chance of movement and will thus lose their spherical shape [49]. The remaining substance on the top gets a quality increase when the liquid is drained from the fluid in the static foam. Viscosity increases with an increase in the quality of the foam. With increasing quality, foam structure holds sand particles in place and does not allow them to settle through it.

By 1968 use of foam fracturing fluid had started in Lincoln County, West Virginia, USA. Small scale fracturing projects were in progress using foam fracturing fluid in North America in the 1970s. Full-scale foam-based hydraulic fracturing fluid was first introduced in 1976. Between 1977 and 1978 methanol was used as a base fluid in order to reduce formation damage [45]. In the 1980s, research and manufacturing of foam-based fracturing fluid were in full swing [50].

In 1980 Gaydos and Harris had studied the West Virginia Devonian Shale and Kentucky Berea Sandstone formations thoroughly and found that both formations have natural fractures [49]. These natural fractures can drain off fluids and the result of the fracturing treatment be vain. 70/170 mesh sand was used as a bridging agent to prevent such fluid loss. Issues related to acid crosslinking in carbon dioxide-based foam fracturing were solved by Harris towards the end of the 1980s. This invention increased the viscosity and upgraded the sand/proppant carrying capacity thus bringing forth the vast application of foam-based fracturing fluid [51].

After the adoption of a slowed crosslinking approach, crosslinked nitrogen-based foam fracturing fluid was developed in 1983 using crosslinking agents [52]. Craighead et al. proved that non-crosslinked foam fracturing fluid has very low viscosity and poor sand carrying ability than crosslinked foam fracturing fluid [53]. In high temperature deep well CO₂ based crosslinked foam fracturing fluid was used earlier than the N₂ based fluid though it appeared later [54]. The 2D model of an aqueous state foam bubble structure was studied by Sun and Hutzler in 2004 [55].

Table 2.1 shows different development timeframes and their attributes. At present, the foam fracturing fluid is widely used in western Canada, southern Alberta, San Juan Basin, Xinjiang, and the Ordos Basin in China [45]. In Tables 2.2 and 2.3, necessary

formation parameters for the design of fracturing treatment and rates and pumping volumes of foam and gelled water treatment are given, respectively. Calculated fracture designs are compared in Table 2.4. For both gelled water and foam computer designs predicted similar results for each location. This design only predicted the creation and distribution of proppants in a fracture, and it assumed that the completion of recovery of the fracturing fluids. Clay swelling, fluid retention by the formation damage, capillary imbibition, or some other mechanisms may occur. Although foam-based fracturing fluid technology has gone through many advancements, the requirement of larger logistics, high initial cost, and less tolerance of the increasing temperature are some drawbacks of it. In 2017 Wanniarachchi et al. thoroughly reviewed foam-based fracturing on shale formation and no such obvious geological or geochemical limitations are found in the literature which can limit the application of foam-based fracturing technology [56]. Further research needs to concentrate on these and how they can become a viable alternative to conventional fracturing fluids.

Table 2.1: Development of foam fracturing fluid technology [45]

Timeframes	Attributes
First-generation (the 1970s)	<ul style="list-style-type: none"> • Foam fracturing fluid was mostly based on water. • The stability of the foam was very low. • Sand bearing capacity was limited to 120 ~ 240 kg/m³.
Second generation (the 1980s)	<ul style="list-style-type: none"> • The stability of the foam was favorable. • Viscosity was heightened. • Sand bearing capacity was improved to 400 kg/m³
Third generation (the 1980s-1990s)	<ul style="list-style-type: none"> • Foam fracturing fluid was mostly crosslinked. • Greater uniformity and stability in the dispersion of bubbles were achieved. • Sand bearing capacity was greater than 600 kg/m³
Fourth and current generation (after the 1990s)	<ul style="list-style-type: none"> • Foam fracturing fluid was resistant to the high temperature. • Resistance to shear was improved. • Improved stability of foam was achieved. • Better sand-bearing capacity was attained. • Economic viability in large sand fracturing operations

Table 2.2: Typical Formation Data for Fracturing in West Virginia Devonian Shale and Eastern Kentucky Berea [49]

Formation Data	West Virginia Devonian Shale	Eastern Kentucky Berea
Permeability (mD)	0.01	0.01
Porosity (%)	10	10
Bottom hole treating pressure (psi)	1500	2500
Reservoir fluid pressure (psi)	900	700
Closure pressure (psi)	1000	1100
Net fracture height (ft)	150	30
Well spacing (acres)	100	40
Depth (ft)	4000	3500
Bottom hole temperature (°F)	85	85

Table 2.3: Typical Fracturing Design for West Virginia Devonian Shale and Eastern Kentucky Berea [49]

Foam Treatments	West Virginia Devonian Shale	Eastern Kentucky Berea
Foam quality	75	75
Foam rate (BPM)	40	25
Water rate (BPM)	10	6.25
N ₂ rate (scf/min)	17700	17800
The volume of injected foam (bbl)	1000	800
Sand 70/170 mesh (lb)	15000	15000
Sand 20/40 mesh (lb)	45000	30000
Ground Water Treatments	West Virginia Devonian Shale	Eastern Kentucky Berea
Water rate (BPM)	40	25
Polymer gel (lb/Mgal)	20	20
The volume of injected water (bbl)	1000	800
Sand 70/170 mesh (lb)	15000	15000
Sand 20/40 mesh (lb)	45000	30000

Table 2.4: Fracture characteristics computed for typical designs of Table 2 [49]

Fracture Characteristics	Foam		Water	
	West Virginia Devonian Shale	Eastern Kentucky Berea	West Virginia Devonian Shale	Eastern Kentucky Berea
	Length (ft)	288	560	484
Height (ft)	250	50	219	27
Flow capacity (mD-ft)	933	1342	954	1499
Bed concentration (lb/1000 ft ²)	417	804	282	903
Production increase	3.1	7.1	4.1	6.6
Fluid efficiency (%)	88	88	89	87

formation characteristic for hydraulic fracturing by liquid nitrogen. Liquid N₂ is environment-friendly, and its low temperature helps the rock to fracture. These features make it a good anhydrous fracturing fluid [59].

To date, cryogenic fracturing is new to the petroleum industry and there is limited research in this field. Liquid N₂ is a common cryogen with a boiling point of -196°C. Cryogenic fracturing eliminates the exertion of high hydraulic pressure and uses thermal shock produced by cryogenics to activate high contraction for breaking reservoir rocks [60]. When liquid N₂ comes into contact with rock walls, a thermal contraction of 7050 psi occurs. This contraction is 5050 psi over the minimum horizontal stress. Tensile strength is also exceedingly greater than the typical sandstone and shale [61]. Liquid N₂ has an extremely low temperature which helps in the extension of the initial fractures and the formation of new fractures in hot naturally fractured reservoirs. Due to the thermal stresses, the formation deforms. These added fractures increase the fracture density and enhance reservoir reconstruction volume. Thus, the fracturing process continues from the main cracks to secondary cracks. Secondary cracks are perpendicular to the main crack. When constant temperature and pressure are maintained at the main crack surface these cracks continue to propagate into the formation [62].

McDaniel found that when liquid N₂ is used in fracturing for the first time it creates extra stress on the rock because it has high interaction with formation fluid and nearby area of fracture [63]. A process for increasing production was proposed by Tenneco Oil Company in 1971. First, the temperature of the formation was reduced to the reservoir fluid freezing temperature by injecting low-temperature brine and liquid N₂ inside the injection wells. Then high-temperature steam was injected into the formation for the thermal recovery process. Finally, after these two cycles, the rock structure is shattered, creating micro-fractures which in the end yielded enhanced production [64].

Grundmann reported that the low temperature (-160°C to -149°C) of liquid N₂ leads to hot tensile stress which causes micro-fractures in the rock wall [65]. According to Gupta et al.'s suggestion use of liquid N₂ helps proppant to be speedy and effective in traveling through fractures and boreholes along with the turbulence of fluid [66]. N₂ based fracturing fluids are most suitable for shallow formation depth. N₂ is relatively

cheap than other fracturing fluids as it is found in the atmosphere (78 percent in volume) and thus liquid N₂ can be manufactured easily. Being readily available does not pollute the reservoir. For reservoir protection and fracturing operation, liquid N₂ shows good performance. Problems related to filtration and hydration expansion are also effectively reduced.

Although it has many advantages high leak-off rate while using as a cryogenic fluid, high pumping pressure relative to conventional fracturing fluid is the major hindrances to its practical implementation and it also escalates the cost. Moreover, the placement of proppant in a high-velocity gas stream creates problems in design and field application which may cause erosion. N₂ fracturing cannot be applicable where the bottom hole treating pressure is less or equal to the minimum horizontal stress of the formation. The large-scale geo-mechanical regime controls this minimum horizontal stress of the formation and it enhances with overburden stress [18]. Moreover, formations in which stimulation causes self-propping fractures i.e., fragmentation at fracture surface, low proppant carrying ability of nitrogen reduces its application. But this feature also allows N₂ fracturing to be more applicable for shallow formation of quartz and dolomite i.e., high brittleness index rock by leading to small fragments, and thus the fractures remain open.

2.3 Carbon Dioxide Fracturing Technologies

Carbon dioxide is one of the prominent waterless fracturing fluids which is cost-effective, readily available, and environment-friendly. In the subsections of this section the green and sustainable carbon dioxide fracturing technology has been described in detail.

2.3.1 Fracturing by Carbon Dioxide

In the 1960s liquid CO₂ was used as a sand-carrying fluid in the petroleum industry [67]. Its first use in fracturing operation was reported in July 1981 [68] in Glauconite sandstone reservoir, Canada. Liquid CO₂ was blended with sand/proppant to go into the

reservoir and to induce fractures. According to Bullen's proposal in 1982, liquid CO₂ shown better performance in formations with low permeability and pressure and is sensitive to water. It had been widely used in the development of tight gas in the US and Canada since then [69].

A specially designed pressurized blender is required for pumping liquid CO₂. Proppant and liquid CO₂ are mixed in the blender under high pressure. This method needs high pressure to keep CO₂ in liquid form, initiate fractures in the reservoir rock, and increase proppant transportation. Proppant carrying ability is important to keep fractures open after the release of pressure. Before the main fracturing operation proppant is preloaded in a CO₂ blender which is a closed pressurized vessel. Blender has a diversified system that blends liquid CO₂ streams with proppants before they are introduced into high-pressure fluid pumps. At a temperature and pressure of -17.78°C and 300 psi respectively, liquid CO₂ is introduced into the closed blender. To force the liquid CO₂ into the closed blender effectively, N₂ gas is utilized as a positive displacement "blanket". Fracturing operations need an injection rate ranging from 30 BPM to 55 BPM, based on tubular constraints and frictional effects [18].

Figure 2.4 shows the conceptual mechanism of the injection of carbon dioxide in the shale reservoir. The first step is to inject CO₂ into the fractures rapidly. Then CO₂ begins to enter the rock based on the pressure gradient in the second step. In the third step, CO₂ permeates into the rock, depending on swelling and reduced viscosity hydrocarbon transfers to bulk carbon dioxide in fractures. CO₂ pressure equalizes the rock at the final step. Then concentration gradient-driven diffusion drives the hydrocarbon production and this hydrocarbon is swept through fractures by bulk carbon dioxide to the production well [70]. In 1985 Settari et al. invented the carbon dioxide fracturing model utilizing a less viscous fluid. With the help of numerical simulation, they proved that CO₂ fracturing can support the fracture network [71]. A higher concentration of proppant along with CO₂ fracturing was patented by Luk in 1994 and it was successfully implemented in Canada [72].

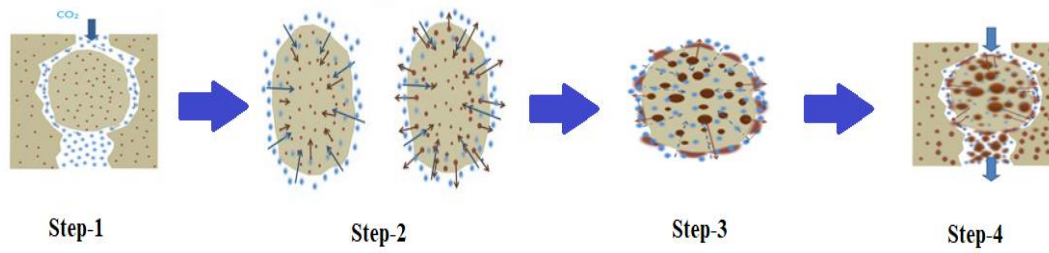


Figure 2.4: Conceptual mechanism of carbon dioxide injection in shale reservoirs [70]

In 1993 The U.S Department of Energy started unique waterless hydraulic stimulation using CO₂/sand, N₂ gas, and N₂ foam technology at Big Sandy gas fields which occurs in water-sensitive Devonian shale of eastern Kentucky. They also ran the stimulation tests in three wells in the Galbraith reservoir in 1995 and reported the same results. From their results, it can be inferred that due to increased gas production CO₂/sand technology is superior to other waterless methods featured in Table 2.5 [73]. The surface flow process and design of liquid CO₂ fracturing fluid technology were invented by Campbell et al. to carry proppant and this process has gone through many advancements to date [74].

Table 2.5: Effect of Stimulation Method on Gas Production from the Big Sandy reservoir [73]

Stimulation Type	Average 5-Year Cumulative (MMcf/Stage)
CO ₂ /Sand	68.3
N ₂ gas	22.9
N ₂ foam	10.5

In 2002, a field trial was performed in Milk River and Medicine Hat formations which are in Southern Alberta, Canada. To enhance the understanding of the economics of increased production several CO₂ energized fracturing fluids were used. In the study, it was found that the use of energized CO₂ fracturing fluids significantly increases the production rate over a longer period [75].

In 2011, Enfrac Inc, Ferus Inc, and RPS Energy Canada Ltd performed a collaborative study on 66 horizontal wells to compare slick-water fracturing fluids and energized fracturing fluids using CO₂ and N₂. According to the production, data CO₂-based energized fracturing fluids exhibit better performance than others [76]. Burke et

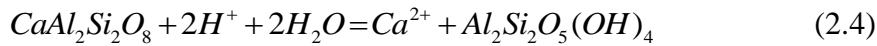
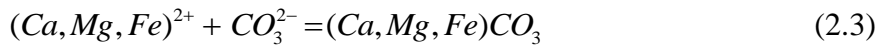
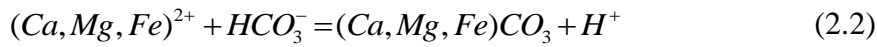
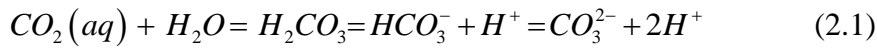
al. added that less water consumption and quick cleanup are some other advantages of CO₂-based energized fracturing fluid [77].

In 2019, Song et al. calculated the fracturing-induced breakthrough surface area (SA_{FIB}). Water fracturing increased the perfect bi-wing splitting with a SA_{FIB} value of 1800 cm² to 1934 cm² which is 7.4% greater than the baseline value. Whereas CO₂ fracturing reached a promising value of 3518 cm² which is 95.4% greater than the baseline value. Thus, CO₂ fracturing provides 81.9% more increase than conventional fracturing and this is evidence of higher SRV can be achieved by CO₂ which also indicates more effective fracturing and enhance production [78].

CO₂-based fracturing fluids also provide better fracturing results among the waterless fracturing fluids. Being environmentally friendly and with a better net present value over long-term production, it is a viable alternative to conventional fracturing fluids. CO₂ is quite compatible with reservoir fluid. Moreover, damage caused by water phase trapping which is an effect of clay swelling will be reduced to a great extent by CO₂-based fracturing fluid. Evaluation of wells is less time-consuming, no swabbing of well, and no disposal of the recovered fracturing fluid is required. In reservoir conditions, CO₂ vaporizes and dissolves in crude oil. Thus, it reduces crude oil viscosity and enhances production efficiency. Using a simple separation technique CO₂ can be reused in fracturing operation when it returns to the ground with the flowback fluid.

Nevertheless, the low viscosity hence poor proppant carrying capacity is a major problem that needs to be addressed in future research. High treatment costs, high pumping requirements, and associated frictional losses raise horsepower requirements as well are also some great drawbacks [79]. However, Sinal et al. stated CO₂ fracturing to be economical as the cost of clean-up and associated rig time is quite less than the conventional fracturing fluids [68]. Besides, ease in filtration makes it unsuitable for formation with higher permeability. Carbon dioxide doesn't react or reacts in a very long span of time with the minerals of the reservoir. But it can precipitate as carbonate minerals when water and bivalent anions are present. This leads to pore clogging, reduction in permeability, and porosity hence reduction in stimulation efficiency and production. This precipitation will only occur with the presence of feldspars [80].

Overall scenario has been presented in form chemical reactions through Equation 2.1-2.4 [18].



2.3.2 Fracturing by Supercritical Carbon Dioxide

At pressure and temperature beyond the critical point, the substance that has no separation between gas and liquid phase is known as a supercritical fluid and it is unique in many aspects [81]. The phase diagram shown in Figure 2.5 demonstrates that when the pressure and temperature of CO₂ are over the critical points (critical pressure and temperature of CO₂ $P_c = 1070.38$ psi and $T_c = 31.05^\circ\text{C}$), CO₂ will achieve its supercritical state (Sc-CO₂).

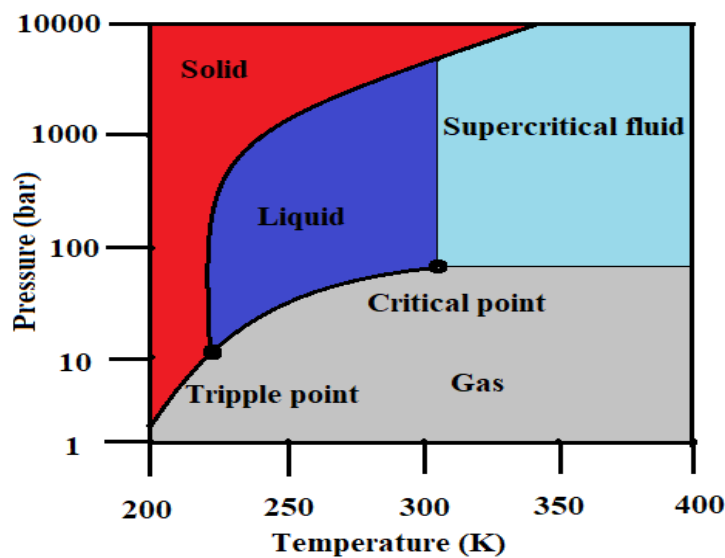


Figure 2.5: Phase diagram of carbon dioxide

High diffusivity and low viscosity are some of the properties of Sc-CO₂, which makes it an ideal non-aqueous fracturing and drilling fluid [82, 83]. Unique properties of Sc-CO₂ which are favorable for unconventional gas reservoirs fracturing can be summarized as follows: (a) Sc-CO₂ has a viscosity similar to gaseous CO₂ and density like the liquid CO₂. (b) Sc-CO₂ has zero surface tension and at a critical point, it is adjustable and interchangeable. (c) While in compression density increases but no liquid is formed [84]. Compared with aqueous fluids, the unique properties of Sc-CO₂ present more advantages for shale gas development. Sc-CO₂ jet has a high penetration rate and less threshold pressure compared with water jet for rock breaking. Furthermore, due to its low viscosity, it can induce more complex fractures, displace adsorbed CH₄ in shale to increase gas recovery, and minimize environmental impacts [85-88]. Moreover, the reservoir is not damaged by supercritical carbon dioxide. Thus, relative to water based fracturing Sc-CO₂ possesses properties suited for the stimulation of reservoirs with low permeability and water sensitivity [89].

In 2019, Zhou et al. reported on the concept of using Sc-CO₂ to replace the water as a fracturing fluid and increase the permeability of the shale gas reservoir. Preferential adsorption of carbon dioxide over methane in shale can be utilized to increase the recovery of shale gas while concurrently sequestering it in the formation [90]. This is illustrated in Figure 2.6. The potential sequestration of carbon dioxide in shale gas reservoirs is a great opportunity in Sc-CO₂-based fracturing technology [91, 92]. Based on the advantages of supercritical carbon dioxide in shale gas development, an innovative idea that integrated the Sc-CO₂ fracturing technology for CO₂ sequestration and shale gas recovery was proposed.

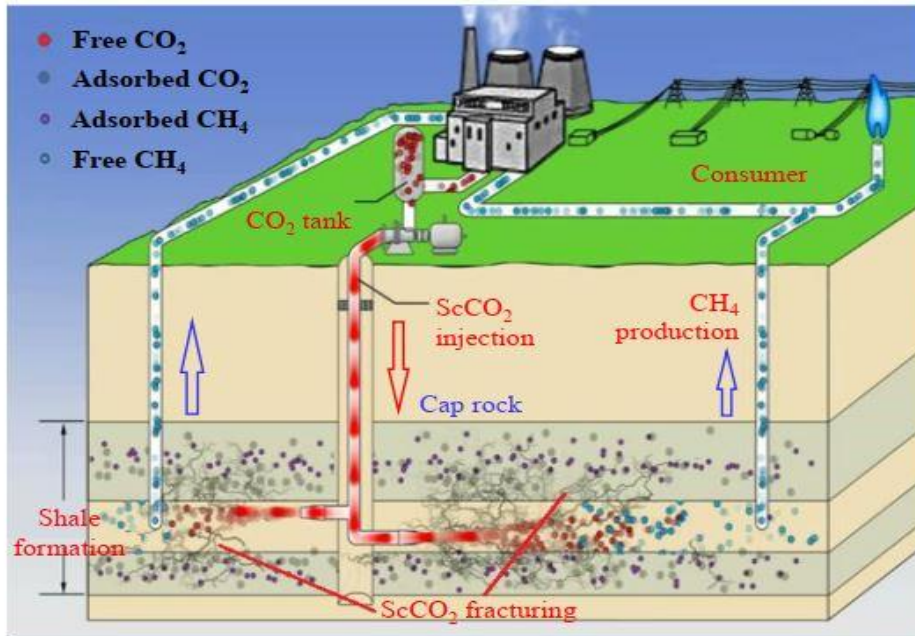


Figure 2.6: Schematic diagram of Sc-CO₂ fracturing for improved shale gas recovery and sequestration of CO₂ [93]

Using granite as a sample in a 30 mL/min condition, Ishida et al. experimented with the source of acoustic emission of liquid and supercritical carbon dioxide respectively in 2012. The fractured pressure produced by liquid CO₂ was 10-11 MPa and 8-9 MPa by Sc-CO₂. These results show that Sc-CO₂ can create more fractures than liquid CO₂ [94]. In 2014, Inui et al. studied fracturing acoustic monitoring experiments that were studied over granite blocks using Sc-CO₂, viscous oil, and water. They compared the viscosity influence of these 3 types of fracturing fluid on the formation and showed that Sc-CO₂ creates more fracture branches and is, therefore, more conducive to fracture network [95]. Sc-CO₂ is the most economically viable alternative candidate to conventional fracturing fluids. Low formation damage, good compatibility with reservoir fluid, quick flowback rate, and higher net present value are some of the properties that make it attractive to researchers in this field. If all the problems associated with Sc-CO₂ fracturing fluids can be solved, then this could be the future of fracturing fluids.

In summary, high diffusion coefficient, low viscosity, zero surface tension are some of the characteristics of supercritical CO₂. These properties enable it to access small fractures more easily and to produce more microfractures than the conventional

hydraulic fracturing fluid. No water phase trap damage or clay swelling is caused by Sc-CO₂ as it doesn't have water in it. There is no formation damage as it has a quick and thorough back row and a brief construction period. In 2012 Wang et al. reported that Sc-CO₂ fracturing offers cost reduction as a reason for gas enhancement [84]. However, Sc-CO₂ allows ease in filtration as gaseous CO₂ and is not suitable for high permeability formation. The viscosity of Sc-CO₂ is very low for fracturing operations and thus possesses weak proppant carrying capacity. Sc-CO₂ fracturing has the same geological limitation as mentioned in carbon dioxide fracturing. Besides, the transportation cost is also very high.

2.4 Factors Affecting Supercritical Carbon Dioxide Fracturing

Factors affecting Sc-CO₂ fracturing such as low viscosity and low proppant carrying capacity, high frictional pressure, fast filtration loss and large displacement, and preferential adsorption over methane have been described in the following subsections.

2.4.1 Low viscosity and Proppant Carrying Capacity

For enhanced proppant carrying capacity of fluid, viscosity is the most critical criterion. The viscosity of water is 10 times higher than that of supercritical CO₂ and thus the proppant carrying capacity of supercritical CO₂ is worse than that of conventional fracturing fluids [96-98]. The viscosity of reservoir oil and reservoir gas ranges from 0.1 to 50 cP and 0.015-0.003 cP, respectively. Whereas carbon dioxide viscosity varies between 0.003–0.10 cP at reservoir conditions. This is the most critical drawback of using CO₂ for improved gas recovery [19]. Viscosification of CO₂ is related to the enhancement of its proppant carrying capacity. Investigation on the difference in the molecular structure of the polymers such as polymeric thickeners and cationic surfactants reveals that higher viscosity will be achieved at lower concentrations (<1 weight %) of CO₂. Reducing the weight percentage of fluorine in the related molecules or removing fluorine with advance and cost-effective CO₂-philic groups is also another aspect of this investigation [19, 21]. Polymeric thickeners may

degrade under the effect of mechanical shear or breakage of chemical bonds of long polymeric chains. This contributes to loss of viscosity and thus suspension balance. Cationic Surfactants also tend to have high toxicity and very low biodegradability [25, 99, 100]. On the other hand, viscoelastic surfactants are free of solids and have great viscosity. Fewer cleanup issues of formation fractures are associated with viscoelastic surfactants compared to polymer-based fracturing fluids [25]. Viscoelastic surfactants also have desirable characteristics including big effective half-lengths through higher retained conductivity, great proppant carrying capacity, less friction pressure, and simple operational procedure [26].

2.4.2 High Frictional Pressure

Carbon dioxide is highly compressible in both the gaseous and supercritical states. Storage tanks, an airtight blender, manifold trucks, and high-pressure pumps are essential equipment used in Sc-CO₂ fracturing. A heating device is also needed in the case of shallow wells where CO₂ cannot attain its supercritical state [17]. To attain a supercritical state at high pressure, liquid CO₂ needs to be injected using a plunger pump in place of pumping gaseous or SC-CO₂ directly. This is due to the low efficiency and small displacement of the gas booster pump. With increasing depth, liquid carbon dioxide is constantly heated to obtain a supercritical phase. He et al. reported that carbon dioxide flowing in the tubing of 7.3 cm, at a discharge rate of 2.2 m³/min to 7 m³/min friction pressure drop increases 8.6 MPa /1000 m 48 MPa / 1000m [17]. The drag reducer is generally used to reduce friction. Polymer drag reducers for water-based fracturing fluids and drag reducers for carbon dioxide foam fracturing fluids are not suitable for liquid or supercritical CO₂ [101]. Table 2.6 shows the required parameters for the field test which shows that frictional resistance was higher than the pressure loss in slickwater fracturing. This makes increased high-pressure pumps ineffective and the occurrence of overpressure becomes a frequent phenomenon for the ground equipment [102].

Table 2.6: Required parameters for field test [102]

Depth (m)	Cementation	Injection	Fracturing tool	Displacement (m ³ /min)	Frictional resistance (MPa)	Local head loss (MPa)
2500	Cementing to wellhead with surface case (5-1/2")	Injection from tubing case (3-1/2")	Jet fracturing tool with 8-hole 6.5 mm diameter nozzle	2.7	7.5	27

2.4.3 Fast Filtration Loss and Large Displacement

The viscosity of Sc-CO₂ and water at reservoir conditions is tabulated in Table 2.7. From the table, the viscosity of Sc-CO₂ is observed to be only one-fourth or one-fifth of that of water. Due to the seepage of fluid in a porous medium, lower viscosity is preferable for easier flow. Thus Sc-CO₂ has less flow resistance than water and besides, it has zero surface tension. Therefore, it can flow without overcoming the capillary force and can invade any space larger than its molecular size. The filtration rate of Sc-CO₂, liquid N₂, and water in the shale reservoir was compared by previous researchers and they found that the Sc-CO₂ filtration rate is double that of water. According to the information it is easier for Sc-CO₂ to infiltrate the reservoir. Therefore, higher injection displacement is required for Sc-CO₂ fracturing.

Table 2.7: Comparison of the viscosity of water and supercritical carbon dioxide at reservoir condition [102]

Fracturing fluids	60°C		70°C		80°C		90°C	
	40 MPa	60 MPa						
Sc-CO ₂ (mPa-s)	0.089	0.1	0.0823	0.1023	0.0762	0.0957	0.0708	0.0899
Water (mPa-s)	0.476	0.4813	0.4143	0.4197	0.365	0.3705	0.3252	0.3306

2.4.4 Preferential Adsorption over Methane

Many researchers have analyzed the economic viability of, and issues related to the use of CO₂ in shale gas exploration from the aspect of carbon dioxide sorption. Recent research in this field has summarized findings on this and expressed possible future

directions. The adsorption-desorption process of carbon dioxide and methane is similar except for the disparity in maximum adsorption capacity. To characterize carbon dioxide adsorption in the shale Langmuir model is inapplicable at pressures greater than 6 MPa [103]. Other adsorption models are also focused on gases in their critical state; however, the physical properties of supercritical gas are different from subcritical status. This is due to a lack of distinction between the gas and liquid phases in supercritical fluids. This challenges the description, interpretation, and behaviour of gas adsorption in this state. Most of the researchers work on the adsorption of pure gas components so sorption studies of mixed gas are fewer. For the implementation of Sc-CO₂ in shale gas recovery and sequestration of carbon dioxide, both adsorption and desorption results are required to get considerable information on sorption hysteresis. In 2019, Rani et al. reviewed the adsorption of methane and carbon dioxide on shale for the recovery of methane and concurrent carbon dioxide sequestration. This article thoroughly discussed different adsorption mechanisms, adsorption isotherms, geologic controls of shale gas system including organic matter content (kerogen types), shale mineralogy, pore structure, and moisture. Moreover, this article discussed the pore structure affecting carbon dioxide/methane adsorption and its relationship with shale composition [104].

2.5 Comparison of Waterless Fracturing Technologies

Table 2.8 presents a comparison of the waterless fracturing fluids discussed in previous sections. Although these fracturing fluids have their benefits, comparative studies indicate that supercritical CO₂ has the upper hand. It provides a better economic net present value (NPV) over a long period. Despite this, it is also associated with problems such as low viscosity and hence poor proppant carrying capacity. To compare LPG, LNG, N₂, and CO₂ fracturing, the Scopus database has been thoroughly explored within the timeframe of January 2005 to August 2020, and Figure 2.7 shows the high research interest in carbon dioxide fracturing in the recent past. Contemporary advancements in the field of fracturing including the authors and their contributions have been summarized in Table 2.9.

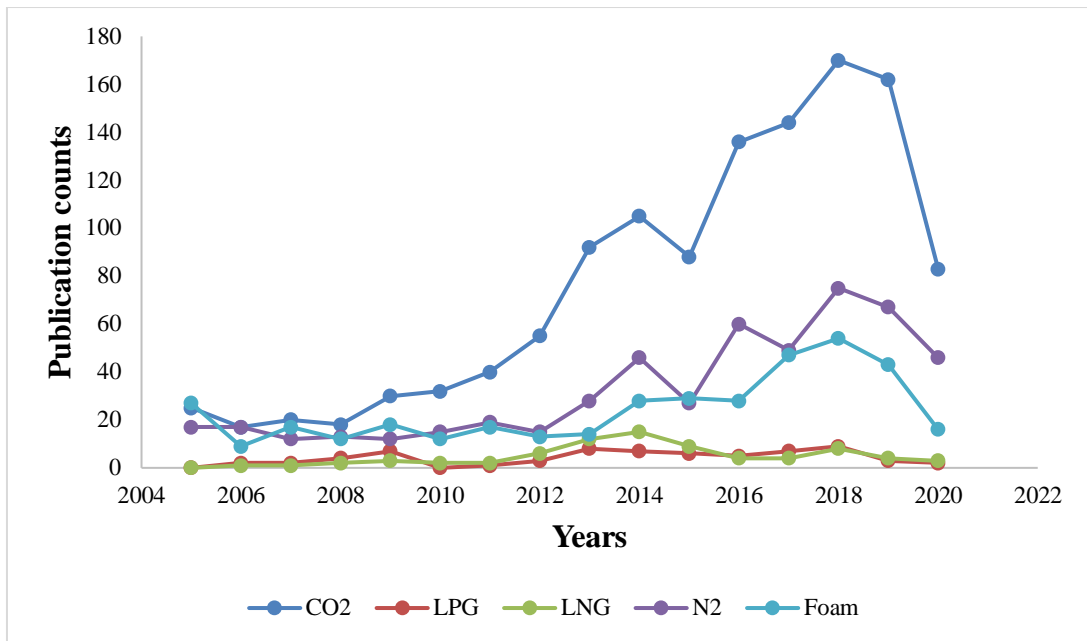


Figure 2.7: Publication count related to waterless fracturing fluids from the Scopus database

Table 2.8: Comparison of waterless fracturing fluids

Contents	Liquified Petroleum Gas (LPG)	Liquified Natural Gas (LNG)	Liquid Nitrogen (N₂)	Carbon dioxide (CO₂)	Supercritical Carbon dioxide (Sc-CO₂)
Surface Tension	Low surface tension	Low surface tension	Higher surface tension than CO ₂	Ultra-low surface tension	Zero surface tension
Formation Depth	Compatible for both shallow and deeper depth	Compatible for both shallow and deeper depth	Only compatible for shallow depth	Compatible for both shallow and deeper depth	Compatible for both shallow and deeper depth
Viscosity & Proppant Carrying Capacity	Moderate viscosity hence good proppant carrying ability	Low viscosity hence poor proppant carrying capacity	Moderate viscosity and has better proppant carrying ability than CO ₂	Low viscosity hence poor proppant carrying capacity	Low viscosity hence poor proppant carrying capacity
Separation Process & Flowback	Simple separation process and high flowback rate	Reusable and high flowback rate	Easier treatment and quick clean-up process	Difficult separation process but rapid and complete flowback	Reusable along with thorough and quick flowback
Hazardous	Very hazardous	Non-hazardous	Being inert gas, it is non-hazardous	Slightly hazardous	Slightly hazardous
Environment-Friendly	Need very less water thus eliminates pollution	Very nature-friendly	No environmental impact	Not very environmentally friendly due to loss of CO ₂ to the atmosphere	Environment-friendly when Sc-CO ₂ is reused in fracturing
Initial Cost	High initial cost	Low initial cost	Medium category initial cost is required	High costing is required for the initial establishment	The highest initial cost is required
Transportation Cost	Moderate cost is required	Very low cost is required	High cost due to pressure-temperature-controlled storage needed	High cost due to storage in pressurized containers	Very high transportation cost
Economic Viability	Lowest NPV with a short period	Moderate NPV over a short period	High NPV but less than CO ₂	High NPV over a long period	Best NPV over a long period

Table 2.9: Summary of recent advancements in fracturing

Contribution Topics	Authors	Contributions	Remarks
Reviews on hydraulic & waterless fracturing	[105]	Problems associated with hydraulic fracturing was discussed.	No possible solution was proposed for the problems.
	[106]	A new family of fluids was created for both conventional and unconventional reservoirs.	Needed to address the concern about large quantities of produced water and their dumping.
	[18]	Reviewed state-of-the-art analyses of waterless fracturing including Liquid CO ₂ /Sand Fracturing, Straight N ₂ Fracturing and LPG, and LNG Fracturing.	It helped to understand the processes, advantages, and disadvantages of the probable waterless fracturing method.
	[107]	Reviewed theoretical and practical aspects of gas production from shale using CO ₂ , LPG, N ₂ technologies.	Technical issues were not addressed.
Experimental study of supercritical carbon dioxide	[103]	Analysis of methane displacement mechanism in nonporous shale.	Provided information on supercritical CO ₂ and its use as a fracturing fluid on shale gas extraction.
	[88]	A renovation of EOR technology based on CO ₂ that focuses on using huff and puff injection at high pressure to improve oil recovery from the fractured tight reservoir.	No focus on existing problems associated with CO ₂ fracturing.
Simulation study of supercritical carbon dioxide	[108]	Describes the behavior of fluids in the nanopore.	Interaction with groundwater was not addressed.
	[109]	The adsorption patterns and mechanism for methane and CO ₂ in shale organic nanopores is analyzed.	In the presence of binary gases, the preferential adsorption of CO ₂ over CH ₄ was not taken into count.
Viscosity of supercritical carbon dioxide	[110]	Introduced an accurate explicit numerical correlation for calculating the viscosity of pure CO ₂ at the supercritical region.	The developed correlation has the advantages of simplicity and low prediction error.
	[89]	Presented the relationship between structure and performance of the co-polymers in Sc-CO ₂ by combining experiment and molecular simulations	Didn't consider the use of viscoelastic surfactants to improve the viscosity of Sc-CO ₂ .

	[20]	Application of VES in hydraulic fracturing stimulation, it's a setback, and mitigation approach adopted in the industry such as using nanoparticles to stabilize its viscosity at high temperatures.	Different pressures were not considered.
Adsorption of carbon dioxide and methane	[104]	Reviewed CH ₄ and CO ₂ adsorption in shale and its dynamic relationship with different geochemical parameters.	It provides great insight into adsorption.
	[111]	CH ₄ and CO ₂ diffusion properties in shales and their modeling.	The modified unipore model is a better model to represent the diffusion of methane and CO ₂ in shales.

2.6 Viscoelastic Surfactants for Supercritical Carbon Dioxide Fracturing

For addressing the complexities of designing a stable fracking fluid using Sc-CO₂, the proprietary viscoelastic surfactant (VES) package is well designed. VES is free of solids and has great viscosity. It exhibits viscous and elastic efficiency in brine and thus increases the viscosity by VES micelles entanglement. Moreover, it presents very few cleanup issues of formation fractures when it is compared to polymer-based fracturing fluids [25]. It retains the desirable characteristics of viscoelastic surfactant fluids to make big effective half-lengths through higher retained conductivity, great proppant carrying capacity, less friction pressure, and simple operational procedure [26].

However, at high-temperature viscosity is lessened considerably. At a condition of high temperature and pressure, added inorganic/organic nanoparticles have been found to help stabilize the viscosity of these VES fluids. For stabilizing the viscosity of viscoelastic surfactants at the very harsh condition of higher pressure and temperature, additional inorganic or organic nanoparticles have been used. By adding a very small amount of inorganic crystals-35 nm zinc oxide this can be achieved [20]. These nanoscale particles possess high surface area and high Van Der Waals and electrostatic forces of attraction. Pseudo crosslinking of surfactant micelles similarly as the crosslinked polymers, nanoparticles give the VES better viscosity. Adding internal breakers to the viscoelastic surfactants helps to break the fluid into low viscosity fluid once the fracturing operation is completed and also to ease the flow-back of viscoelastic surfactant to the surface [20].

Many researchers used organic compounds which combine in solution to "thicken" carbon dioxide. The initial endeavor of CO₂ thickening was unsuccessful as a result of low CO₂ solubility in conventional organic polymers, organometallic compounds, and ammonium carbamates [19]. Although there were occasions where viscosity improvements were observed in the introduction of an organic cosolvent such as toluene and ethanol [112], detection of CO₂ viscosity-increasing agent was not sufficient. Generally, polymer-based fluids have been used to address this concern. Homogeneous polymerizations in CO₂ and Sc-CO₂ were conducted by DeSimone et al.

and fluoropolymers and silicones were found highly soluble in carbon dioxide [113]. At 50°C, 6.7 weight % of poly (1,1-dihydro-perfluorooctyl acrylate) was soluble in carbon dioxide and provided a significant increase in CO₂ viscosity from 0.08 to 0.2-0.6 Cp [22]. This was the first successful attempt at CO₂ thickening. Carbon dioxide soluble fluorinated polyurethane disulfates were synthesized by Shi et al and found that at room temperature, 4 weight % concentration, and 34.5 MPa pressure, it enhanced the solution viscosity 2.7 times than actual CO₂ [114]. However, since filter cake is formed by polymer-based fluids, there have been evident formation damage and poor conductivity which limits its application. Moreover, researches show that cross-linked polymers cause severe damage to formation permeability [23, 24].

CO₂ soluble, cationic, amine-based surfactant has a distinguished feature of dissolving capacity in Sc-CO₂ and forming Wormlike Micelles (WML) at high salinity. The presence of wormlike micelles led to an increase in the viscosity of the aqueous surfactant solution [115]. In high permeability formation and higher temperatures, a methyl quaternized erucyl amine is convenient for VES-based fracturing fluids [116]. Typical VES are like N-erucyl-N,N_bis (2-hydroxyethyl)-n-methyl ammonium chloride, and potassium oleate solution which forms a gel when mixed with appropriate activators such as sodium salicylate and potassium chloride [117]. For Sc-CO₂ vinyl benzoate/heptadecafluorodecyl acrylate (VBe/HFDA) copolymers were synthesized and characterized as thickening agents. When the VBe group is introduced, it reduces the polymer-carbon dioxide interaction and enhanced polymer-polymer interaction. So, this leads to a decrease in the solubility of co-polymers in supercritical carbon dioxide. P(HFDA0.67-co-VBe0.33) was capable of enhancing the viscosity of supercritical carbon dioxide by 438 times at five weight % [89].

2.7 Molecular Dynamic Simulation of Adsorption

In this section the basic adsorption, adsorption models, types of adsorption isotherms, and molecular simulation study of adsorption isotherm have been discussed in detail.

2.7.1 Adsorption

The process by which a solid holds a molecule of gas or liquid or solute as a thin film is known as adsorption and the curve is obtained by plotting at a constant temperature the quantity of adsorbent against the concentration of the substance in the original gas or solution is called adsorption isotherm. Generally, it is a graph derived by plotting the adsorbate amounts (x) by adsorbed on the adsorbent surface (m) and pressure at a constant temperature. It is shown in equation 2.5 that adsorbate gets adsorbed on adsorbent in the adsorption process.



Where this \rightleftharpoons symbol indicates adsorption & desorption is occurring simultaneously. As stated in the principle of Le-Chatelier, “the direction of equilibrium would shift in that direction where the stress can be relieved”[118]. When excess pressure will be applied to the equilibrium system, where several molecules have a cutback, the equilibrium will shift in that direction. The forward direction of equilibrium will be favored, because there is a reduction in the number of molecules in the forward direction, with increasing pressure.

In the year 1909, Freundlich presented an experimental expression that described the isothermal variation of adsorption of an amount of gas adsorbed by a unit mass of solid adsorbent with pressure. This equation 2.6 is known as Freundlich Adsorption Isotherm:

$$\frac{x}{m} = kP^n \quad (2.6)$$

Where, k & n = constants (these values are dependent on gas and adsorbent at temperature) and x = adsorbed gas mass, m = adsorbent mass, and P = pressure. Adsorption relationship at low pressure is established by this isotherm model but it couldn't manage to predict adsorption value at high pressure [119-121].

In 1916 Langmuir Adsorption isotherm was proposed. It was based on different assumptions and the most important one is that there exists a dynamic equilibrium between adsorbed and free gaseous molecules.



In equation 2.7, A(g) = gas molecule, which is not absorbed, B(s) = unoccupied metal surface, and AB is a gas molecule that is adsorbed. Equation 2.8 [121] was derived by Langmuir based on his theory which depicted a relationship between the surface having a number of active sites undergoing pressure and adsorption.

$$\theta = \frac{KP}{1+KP} \quad (2.8)$$

Where, θ = surface having several sites occupied by gaseous molecule, P = pressure, and K = equilibrium constant for distribution of adsorbate between the surface and the gas phase. This adsorption equation is only valid at low pressure, and it is the basic limitation of it. At low pressure, (1+KP) in the denominator can be avoided as KP is very small and the equation 2.8 diminishes to $\theta = KP$. The high pressure (1+KP) in the denominator is almost equal to KP as KP is very large. So, the equation reduces to $\theta = \frac{KP}{KP} = 1$ [120-122].

Multilayer formation physical Adsorption is explained through BET Theory given by Brunauer, Emmett, and Teller. Monolayer adsorption was the basic assumption of Langmuir adsorption, and it is applicable at low pressure. Higher thermal energy and the escape velocity would be possessed by gas molecules at these conditions. Availability of very few gas molecules remaining near adsorbent results from this. At low temperature and high pressure, there is a decrease in the thermal energy of gas molecules and a large number of gas molecules remain available per unit of the surface area. This causes multilayer adsorption which can be explained by Brunauer, Emmett, and Teller theory. This equation 2.9 is given as

$$\frac{P}{V_{total} (P_0 - P)} = \frac{1}{V_{mono} C} + \frac{C - 1}{V_{mono} C} \left(\frac{P}{P_0} \right) \quad (2.9)$$

Where, V_{mono} = volume of adsorbed gas to cover unilayer surface at high pressure, the ratio of $\frac{K_1}{K_L}$ is designated as C. K_1 = constant of equilibrium when each vacant site

adsorb single-molecule and K_L = equilibrium constant to the saturated vapor-liquid equilibrium [121].

In Figure 2.8, different types of adsorption isotherms are shown. Type I, II, & III occur on the non-porous adsorbent and Type IV & V occurs in the porous adsorbent. Type I curve presents monolayer adsorption which can be easily understood utilizing Langmuir Adsorption Isotherm [121]. $E_L = 0$, where E_1 = heat of adsorption for 1st layer and E_L = heat of liquefaction for rest of the layers. Adsorption of nitrogen on charcoal at temperature close to -180°C is an example of Type-I adsorption. Isothermal adsorption curve Type II shows a great detour from the Langmuir model of adsorption. Flat region in the intermediate portion of the isotherm represents monolayer formation. Value of C in BET equation should be larger than 1. Here $E_L < E_1$. Nitrogen gas adsorbed at -195°C on iron catalyst is an example of Type-II adsorption [123].

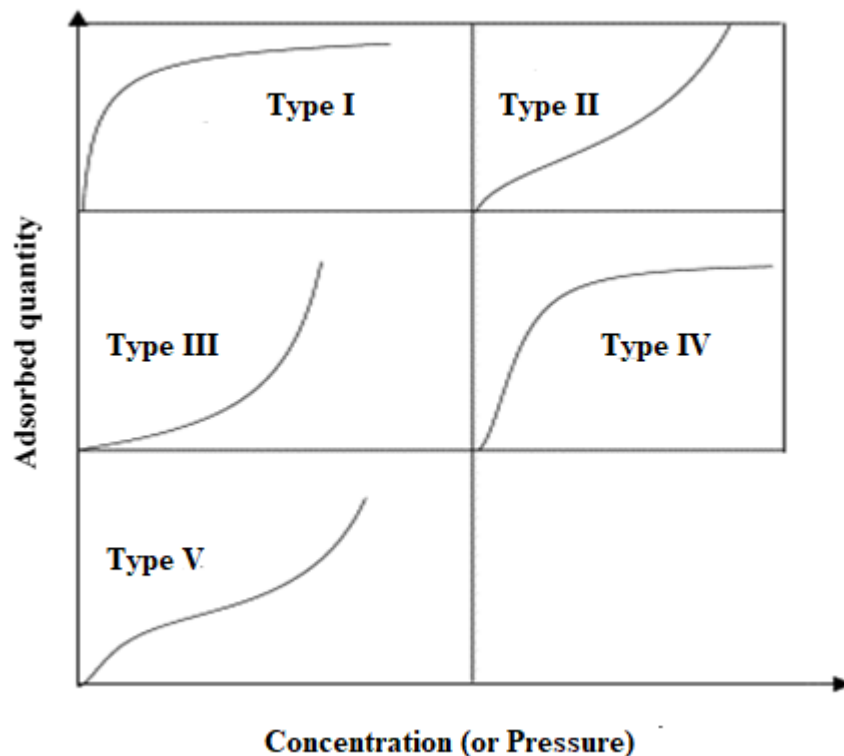


Figure 2.8: Adsorption isotherm types according to BET classification [124]

Isothermal adsorption curve Type III also shows a large deviation from the Langmuir model. In BET equation value if $C \ll 1$ Type III Adsorption Isotherm obtained. This isotherm explains the formation of the multilayer. There is no flattish portion in the curve which indicates that monolayer formation is missing. Here $E_L > E_1$. Examples of Type III Adsorption Isotherm are Bromine (Br_2) at 80°C on silica gel or Iodine (I_2) at 80°C on silica gel. At the lower pressure region of the Type, IV curve is quite like Type II. This explains the formation of a monolayer followed by a multilayer. The saturation level reaches a pressure below the saturation vapor pressure. This can be explained based on the possibility of gases getting condensed in the tiny capillary pores of adsorbent at a pressure below the saturation pressure (PS) of the gas. Here $E_L < E_1$. Examples of Type IV Adsorption Isotherm are adsorption of Benzene on silica gel at 50°C . Explanation of Type V graph is like Type IV. Here $E_L > E_1$. Example of Type V Adsorption isotherm is adsorption of Water (vapours) at 1000°C on charcoal. Type IV and V shows the phenomenon of capillary condensation of gas [121, 123] According to the research by [2] the Langmuir isotherm (Type I) demonstrated an adsorption model for CH_4 and Brunauer Emmet Teller (BET) isotherm (Type II) demonstrated adsorption model for CO_2 .

2.7.2 Molecular Simulation Study of Methane and Carbon Dioxide Adsorption

Molecular dynamics simulation (MDS) is a computer simulation technique where the evolution of time of a set of interacting atoms is followed by integrating their equations of motion. In recent times, MDS has been used to understand and explain the phase behavior, fluid behavior under confinement, fluid-fluid interaction, and shale mineral interaction with fluids.

In a calcite nanopore, MDS is used to anticipate the effect of carbon dioxide on the adsorption of n-alkanes. The calcium sites which are available on the calcite surfaces are observed to tend to preferentially adsorb CO_2 . Comparing to methane, n-octane, or n-butane portion on dense layer near to nanopore walls, CO_2 molecules are present in high proportion. Preferential adsorption selectivity of CO_2 over CH_4 can be explained experimentally that had been observed for the adsorption in limestone [108]. Moreover, a decrease in the amount of carbon dioxide and methane adsorption on the surface of

calcite is caused by higher temperatures. MDS indicates that n-octane and n-butane are willing to adsorb parallelly to the surface of calcite and their distribution of dihedral angle is not affected by under confinement of CO₂ [108]. Carbon dioxide reinjection into shale reservoirs might increase gas recovery.

Using MDS and configuration biased MC methods, reconstruction of shale nanopores molecular model was done with slit and cylindrical pore geometries and sizes of 1, 2, and 4 nm. Density distributions in organic pores for CO₂ adsorption are almost uniform whereas for CH₄ adsorption high-density adsorption regions exist [109]. Modified Brunauer Emmet Teller model provides better fitting of carbon dioxide adsorption than the Langmuir model for isotherm curve of CO₂ which takes the shape of Type-V consequently of CO₂ condensation. Carbon dioxide exhibits higher adsorption affinity comparing to methane adsorption under shale reservoir pressure and temperature [109].

MDS is demonstrating adsorbed molecules mobility has great impacts on flow enrichment in CH₄ flux at high and low pressures in nanopores. Pore width increases similarly with flux in high-pressure flow. Due to neglecting the adsorption layer and its mobility, the HP equation undervalues the flux in nanopores. Molecular velocity enhances in proportion to pore width increase and this enhanced velocity contributes to flux. A small pore having a width of 1 nm, the flux may be one order up in magnitude greater than the flux from the HP equation [125]. For low-pressure adsorption layer's molecules mobility and huge formation fluid, density distribution enhances CH₄ flux. Consequently, flux can be 1-2 orders up in magnitude greater than anticipation from the Knudsen diffusion for long-chain carbon in nanopores of having a small pore of 1 nm [125].

2.8 Carbon Dioxide Sequestration on Shale

As shale is a tight reservoir it is difficult to inject or produce any fluid from it. Due to technological advancements like hydraulic fracturing and horizontal drilling these reservoirs have now become producible. After depletion of the shale reservoir, existing fractures can serve as suitable storage for CO₂. This will also offset the cost of initial

expenses like new well drilling which is required in a saline aquifer [126]. Carbon capture and sequestration (CCS) has drawn the attention of current researchers and shale reservoirs have shown great promises in this regard. “Carbon Capture and Sequestration” as a research topic has been highly explored in the Web of Science database from January 2005 to April 2020. Over the years there has been an increasing trend of research in this field and Figure 2.9 picturizes this high research interest.

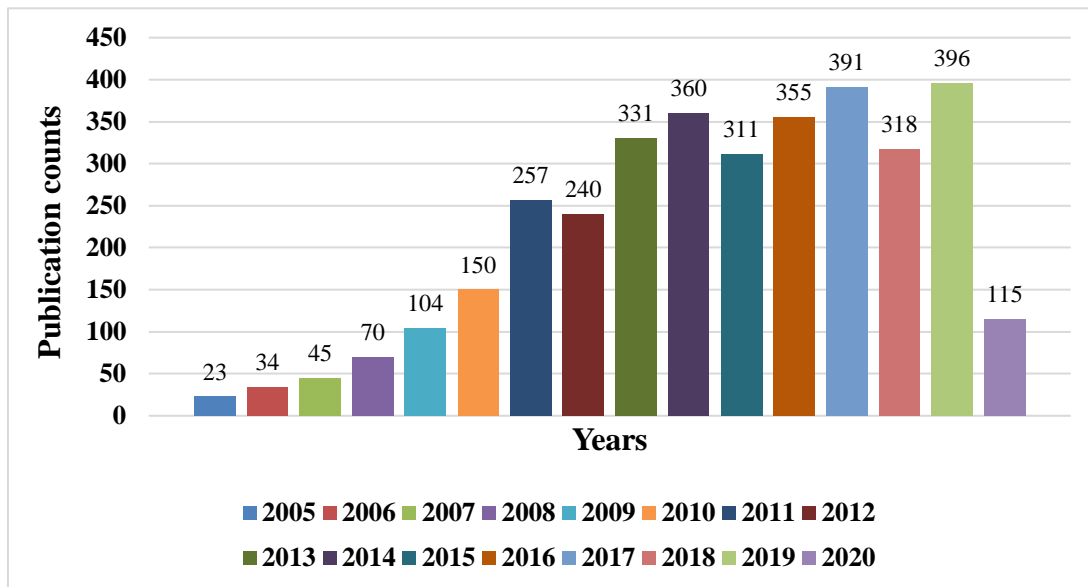


Figure 2.9: Publication count related to CCS from the Web of Science database

According to previous research, the injection time of CO₂ will be faster than the CH₄ production from the shale reservoir. It is also estimated that 14.5 billion tons of CO₂ can be stored in shale reservoirs in the upcoming 2 decades [127]. This estimated capacity is 20% of the total ejection of carbon dioxide from heavy industries in the US within the next twenty years. Numerical research shows that the maximum capacity of carbon dioxide storage is 1.12 MMT/km, whereas the capacity for the sorbed carbon dioxide storage is estimated at 0.72 MMT/km for eastern shale formation in the US [127]. While considering the sorption effect and pore compressibility, the total CO₂ storage capacity was measured in supercritical conditions and as a function of pore pressure [128]. According to the result, kerogen acts as a molecular sieve and dictates the gas sorption on shale. Clay minerals, pore structure, and total organic carbon (TOC) content have responsive effects on sorption capacity [129].

Trapping mechanisms are the most important features for any feasibility study of carbon dioxide sequestration. Four different trapping mechanisms are reported in the literature and are shown in Figure 2.10 They are termed structural and stratigraphic trapping, residual CO₂ trapping, solubility trapping, and mineral trapping. Structural and stratigraphic trapping is also known as hydrodynamic trapping which refers to captured CO₂ in its gaseous or supercritical phase under a low permeable caprock. After injecting CO₂, it becomes more buoyant than other fluids that are already in the pore space. Then CO₂ pervades through the porous rocks until it meets the impermeable layer of caprock and gets trapped. In the case of site selection for CO₂ sequestration, this physical mechanism creates a big challenge and it is greatly dependent on the sealing capacity of rock [130]. Residual trapping happens very quickly as the porous rock acts like a tight, rigid sponge. Injected CO₂ displaces the brine in the first place but at the end of injection, due to the density difference, CO₂ migrates up and brine flows downwards. Thus, brine displaces CO₂ and significant saturation of CO₂ gets trapped as an immobile phase in small clusters of pores [131].

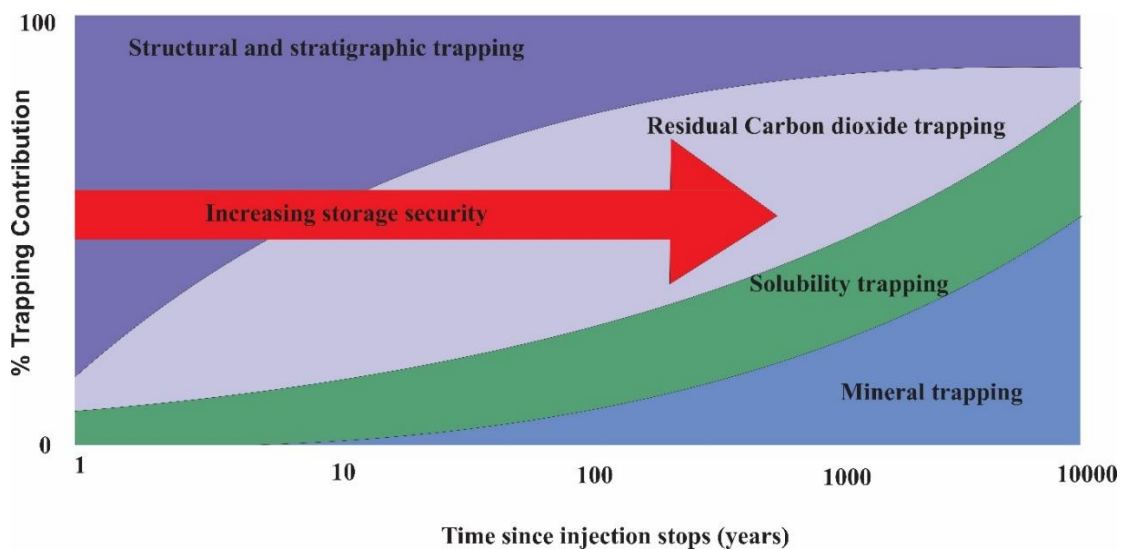


Figure 2.10: Schematic of carbon dioxide trapping mechanisms over time [132]

The solubility trapping mechanism refers to the dissolution of CO₂ in its gaseous and supercritical state into a brine. After injection, CO₂ meets the formation of brine and hydrocarbon in the interface between the reservoir and caprock. Mass transfer occurs with CO₂ dissolving into brine by molecular diffusion until the equilibrium state is reached. This solubility of CO₂ is mostly reliant on pressure, temperature, and salinity

of formation fluid [133]. As the molecular diffusion coefficient is very small this process takes thousands of years to be completed [134]. Mineral trapping is defined as the incorporation of carbon dioxide with minerals and organic matters in the formation through chemical reactions. When CO₂ dissolves in water it forms a weak carbonic acid, this weak acid can react with the minerals in the surrounding rock to form solid carbonate minerals. Mineralogy, structure, and hydrogeology of a specific lithology have a great impact on this process [135]. This process can be rapid or very slow depending on the chemical reactions of the rock and water in a specific storage site, but it effectively binds CO₂ to the rock. Espinoza et al. reported representative chemical reaction and their reaction rate [136] and these reactions have been tabulated in Table 2.10. These trapping processes take place over many years at various rates from days to years to millennia, but with time geologically stored CO₂ is generally safer to trap. Trapping time is the same as the nuclear storage project and could be up to 10000 years. It is very tough to imagine that it has been 11,000 years since the last ice age [137].

Table 2.10: Chemical reactions between minerals acidified CO₂ water [136]

Minerals	Typical reactions	Reaction rate (mol.m ⁻² .s ⁻¹)
Silicates [138]	SiO _{2(s)} + 2H ₂ O ↔ H ₄ SiO ₄ ↔ H ⁺ + H ₃ SiO ₄ ⁻ ↔ H ⁺ + H ₂ SiO ₄ ²⁻	1.26 * 10 ⁻¹⁴ [139]
Aluminosilicates [140]	Anorthite: CaAl ₂ Si ₂ O _{8(s)} + 8H ⁺ ↔ Ca ²⁺ + 2Al ³⁺ + 2H ₄ SiO ₄ Kaolinite: Al ₂ Si ₂ O ₅ (OH) _{4(s)} + 6H ⁺ ↔ 2Al ³⁺ + 2H ₄ SiO ₄ + H ₂ O	Anorthite: 1.2 * 10 ⁻⁵ Oligoclase: 1.2 * 10 ⁻⁸ Albite: 3.6 * 10 ⁻⁹ Kaolinite: 10 ⁻¹⁴ - 10 ⁻¹⁵ [141]
Carbonates [142]	CaCO _{3(s)} + H ⁺ ↔ Ca ²⁺ + HCO ₃ ⁻ CaCO _{3(s)} + CO ₂ + H ₂ O ↔ Ca ²⁺ + 2HCO ₃ ⁻	Calcite: 1.6 - 3.2 * 10 ⁻⁵ [143]

Feasibility studies of CO₂ sequestration are not dependent on one trapping mechanism. Throughout the lifetime of the project different geophysical characterizations must be performed. As an example, the sensitivity to different characteristics such as matrix permeability, initial natural fracture conductivity, and initial hydraulic fracture conductivity, might be higher at the beginning and final phases of sequestration. Therefore, it is suggested that for confirmation of secured CO₂ trapping time-lapse surveys should be conducted throughout the project's lifetime [144, 145]. All possible chemical and physical approaches to capture carbon dioxide are presented in Table 2.11.

Table 2.11: Physical and chemical approaches to CCS [146]

Separation approach	Absorption	Adsorption	Cryogenic	Membrane	Mineralization
Description	CO ₂ from the gas stream dissolves in a fluid. Subsequently, CO ₂ is released (solvent is regenerated) from the fluid by changing pressure or temperature.	CO ₂ adsorbs on a solid from the gas stream. Subsequently, CO ₂ is released (adsorbent is regenerated) by modifying pressure or temperature.	CO ₂ is refrigerated until it transforms into a solid, separating it from the gas stream.	CO ₂ is preferably transported from a pressurized gas stream via a membrane.	CO ₂ forms magnesite or calcite after binding with calcium or magnesium-bearing rocks.
Example materials	Aqueous amine solutions, Chilled ammonia, Ionic liquids.	Zeolites, Metal-organic frameworks, Activated carbon.	No specific material requirement.	Polymer membranes, Inorganic membranes.	Magnesium silicates, Alkali-rich waste streams.
Advantages	Established technology, numerous solvent options and rapid improvements in energy requirements are achieved.	Possibly lower regeneration energy is needed.	Avoid the need for solvents or sorbents, Lower energy requirements.	Avoid regeneration energy requirement.	CO ₂ is processed into a solid material that can be recycled or disposed of in surface installations as a building material.
Technological Challenges	Reducing energy for regeneration, solvent degradation.	Adsorption capacity and kinetics	Solid separation and handling	Permeability Selectivity	Rate of reactions Mass of reactants (e.g., source of Mg, Ca)
Environmental impacts	Increased water usage if aqueous solvents are used Fugitive emissions of solvents and solvent degradation products Increased fossil-fuel consumption for energy required for capture	Increased fossil-fuel consumption for energy required for capture Disposal or recycling of spent adsorbents	Increased fossil-fuel consumption for energy required for capture	Increased fossil-fuel consumption for energy required for capture	Increased fossil-fuel consumption for energy required for capture Disposal and storage of materials if markets cannot be found Impacts of mining for minerals used in the carbonation reactions

Status	Aqueous amine solvents are available and demonstrated at industrial scale (8 Mt/year). New solvents are being developed and tested at the bench and pilot scale.	Bench and small-scale pilot testing in progress	Deployed on a limited basis at an industrial scale for CO ₂ /CH ₄ separation. Bench and small pilot-scale testing is underway for flue gas separation.	Deployed on a limited basis at an industrial scale for CO ₂ /CH ₄ separation (7 Mt/year)	Under development
---------------	--	---	--	--	-------------------

Tao et al., 2013 estimated the capacity of CO₂ sequestration of shale formations utilizing the production rates of methane. Their results show that between the years 2015 and 2030 Marcellus shale alone can sequester 10.4 -18.4 GT of carbon dioxide which is more than half of the total United States CO₂ emission [147]. In 2014 Schaefer et al. investigated the economic impact of carbon dioxide utilization and storage in shale gas reservoirs. They reported that after finding suitable formations and collecting necessary experimental data for a specific shale formation, reservoir modeling is very strategic. These reservoir models assist to optimize injection rates, maximum desorption of methane, and retention of carbon dioxide volume at the field level [148]. Merey et al. analyzed CO₂ sequestration in shale formation by utilizing experimental adsorption data and models. In comparison to the Langmuir model, they found that Ono-Kondo models have a high capability for both low and high pressure. From their observation adsorption capacity decreases when there is a temperature rise, hence temperature has a great impact on adsorption. [149]. Europe and the United States are the highest contributors to CCS projects. Figure 2.11 shows the pie chart distribution of the world's CCS projects where China, Canada, Australia are also other major players.

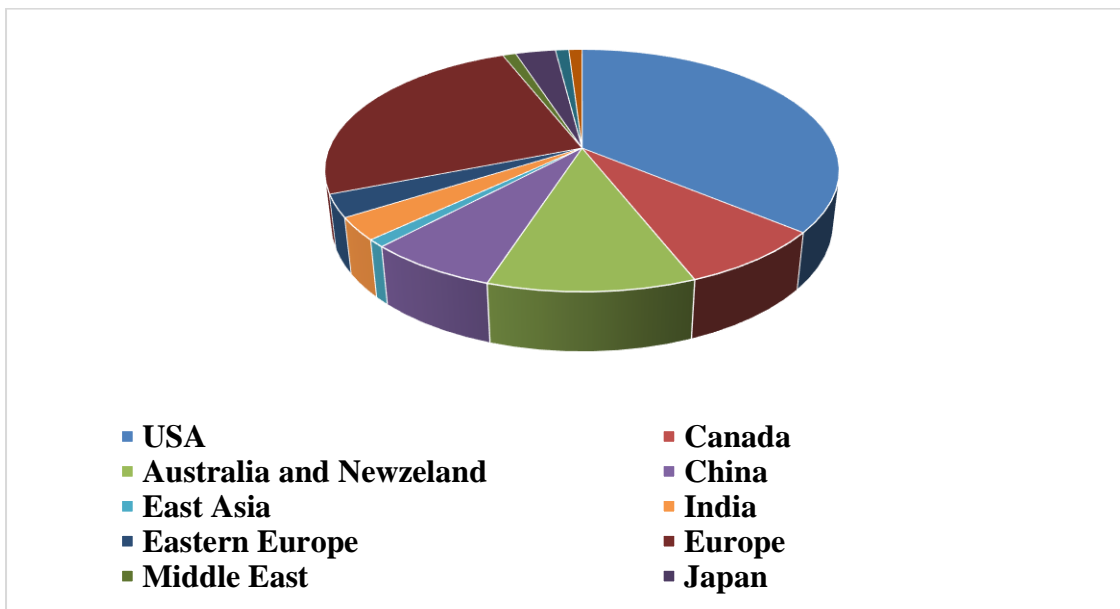


Figure 2.11: Active countries with CCS program [132]

2.9 Summary and Recommendations

Waterless fracturing technologies are gaining attention due to the dire need to protect water resources and ever-increasing environmental concerns. No formation damage, high compatibility with reservoir fluids, increased production, quick flowback rate, reusable materials, energy conservation, and environment-friendly features like less water consumption are some of the advantages of waterless fracturing technologies. The most promising among waterless fracturing fluids is SC-CO₂. In the case of an anthropogenic CO₂ source, the benefit is twofold. Nevertheless, considering the fracturing operation, poor proppant carrying capacity, high frictional resistance, high displacement, and easy sand plugging are some of the potential limitations. Therefore, to exercise Sc-CO₂ fracturing technology in the field, one must overcome these problems. Use of thickener along with Sc-CO₂ and ultra-low-density proppants can eradicate the poor proppant carrying ability and fix sand plugging. Although viscoelastic surfactant (VES) has been used in water-based fracturing fluids, its addition to Sc-CO₂ is very recent. Moreover, from this extensive literature review, it can be inferred that shale reservoirs have a great capacity for CO₂ storage (5-10 Kg/ton per formation) and CO₂ sequestration. However, long-term CO₂ storage feasibility needs extended study.

With respect to the extensive literature review, some prospects of future research can be listed to make Sc-CO₂ a strong alternative to conventional fracturing fluids.

- The adsorption mechanism of methane (CH₄) and carbon dioxide (CO₂) on shale needs to be investigated at the molecular level.
- Existing adsorption isotherm models cannot provide the best fit of CO₂ in the supercritical state. Therefore, finding the best-fit adsorption isotherm would be a great advance.
- New drag reducers can be developed, and a larger casing size should be selected to tackle the problems related to high displacement and high frictional resistance.

CHAPTER 3

RESEARCH METHODOLOGY

3.1 Introduction

This chapter explores the methods employed to obtain the objectives of the study. Flowchart in Figure 3.1 shows the outline to complete the research. Characterization study of shale samples from Eagle Ford, Mancos, and Wolfcamp formations was carried out using field emission scanning electron microscope (FESEM), surface area analyzer and porosimetry system (SAP), X-ray diffraction (XRD), helium porosimeter, and total carbon (TC) analyzer. A heterogeneous molecular shale model consisting of Kerogen type II D, montmorillonite, illite, and quartz was developed. Physical properties such as density, surface area, and cumulative volume which were determined from the characterization study were used to validate the molecular shale model. Moreover, a simulation study of Sc-CO₂ thickening was completed using fluorinated VES N-ethyl perfluorooctyl sulfonamide, and non-fluorinated VES, N,N,N'-Trimethyl-1,3-propanediamine. Nonetheless, a preferential adsorption study of thickened Sc-CO₂ and CH₄ on the molecular shale model was performed using molecular simulation. Both thickening and adsorption simulations were accomplished using Materials Studio software.

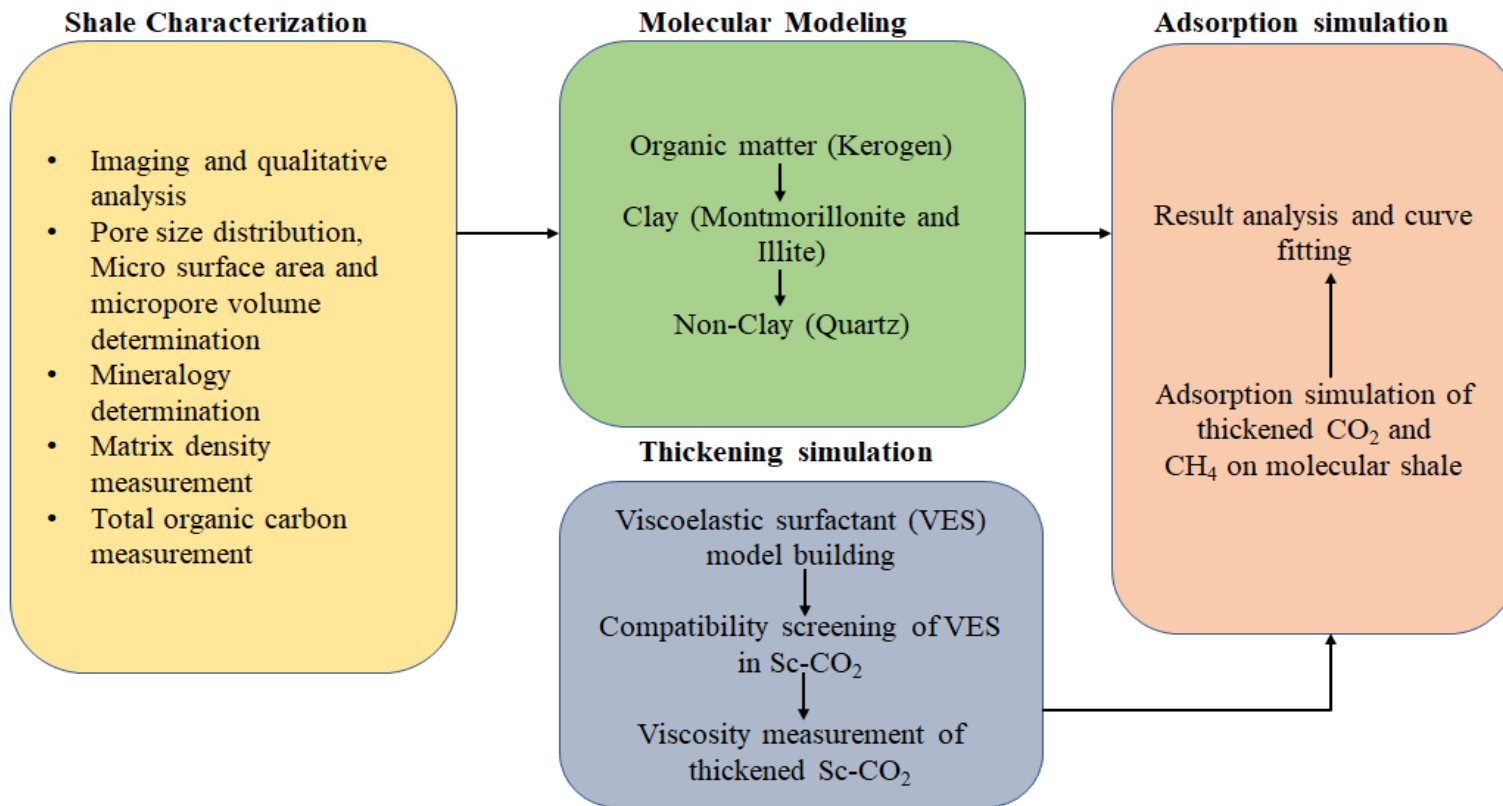


Figure 3.1: Flowchart of the overall methodology

3.2 Shale Samples

Shale samples were examined which came from well-known shale formations of the USA. Figure 3.2 presents a picture of powdered samples used in this study. Shale outcrop cores from Eagle Ford (EF-1, and EF-2), Mancos (MC), and Wolfcamp (WF) shale formations were purchased from a commercial supplier; Kocurek Industries Inc. Eagle Ford shale is a Late Cretaceous shale located in south Texas [150]. The two samples from Eagle Ford shale used are grey. Mancos shale formation is found in New Mexico, Utah, and Wyoming, and it belongs to the Late Cretaceous age [151]. The Mancos shale sample examined is grey having light grey interbedding layers throughout. Wolfcamp shale sample was black with no notable interbedding layers. Wolfcamp shale formation is a Devonian gas-producing shale found throughout the Permian Basin [152].



Figure 3.2: Shale samples from Eagle ford, Mancos, and Wolfcamp formation in powder form

3.3 CO₂, CH₄, and Surfactants Model

In this study N-ethyl perfluorooctyl sulfonamide (N-ETFOSA) [153] and N,N,N'-Trimethyl-1,3-propanediamine (N,N,N'-TM-1,3-PDA) are used as viscoelastic surfactants. The chemical formulas of N-ETFOSA and N,N,N'-TM-1,3-PDA are C₁₀H₆F₁₇NO₂S and C₆H₁₆N₂, respectively. Figure 3.3 presents the 3D structures of Sc-CO₂, CH₄, N-ETFOSA, and N,N,N'-TM-1,3-PDA. All these structures were optimized using appropriate forcefield. The density of CO₂, CH₄, N-ETFOSA, and N,N,N'-TM-1,3-PDA has been adapted from literature as 0.001836 g/cm³ [154], 0.716 g/cm³[155], 1.7 g/cm³ [155], and 0.793 g/cm³ [156], respectively. N-ETFOSA and N,N,N'-TM-1,3-PDA have the molecular weight of 527.2 and 116.2 respectively [156].

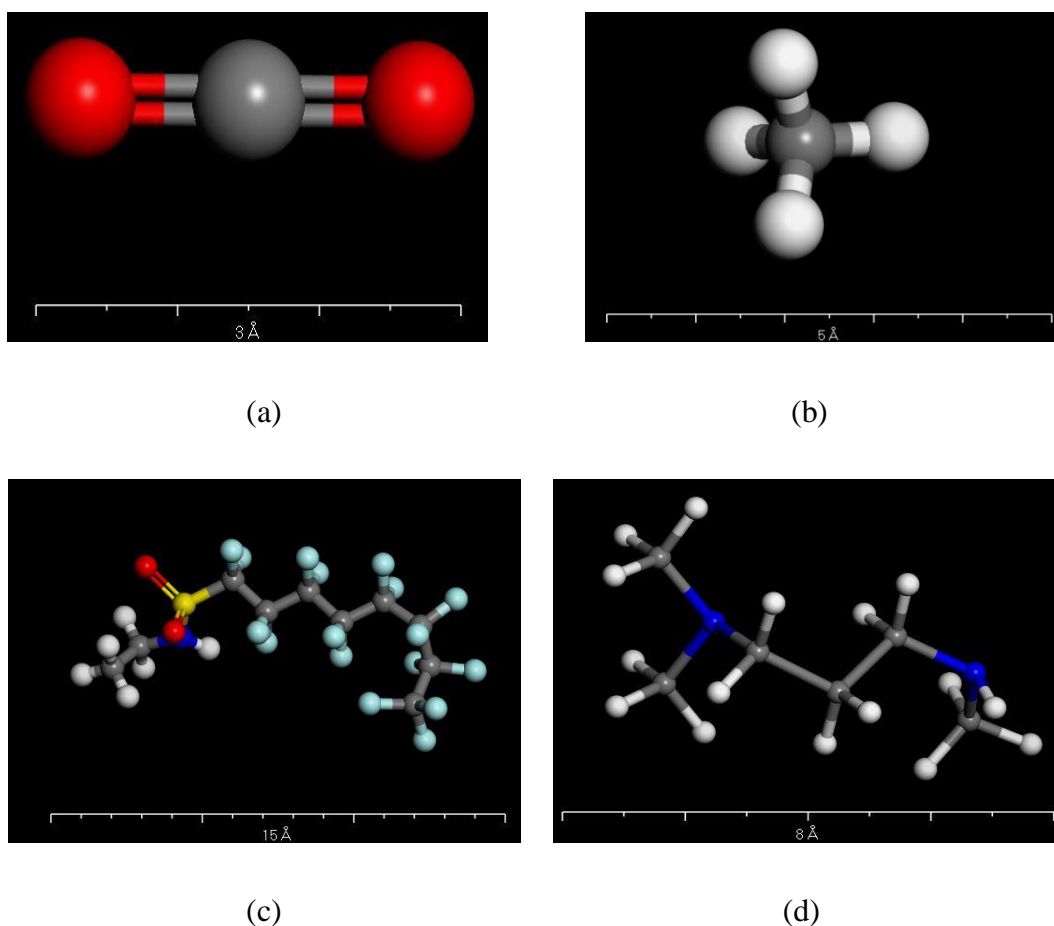


Figure 3.3: 3D structures of (a) Sc-CO₂, (b) CH₄ (c) N-ethyl perfluorooctyl sulfonamide, and (d) N,N,N'-Trimethyl-1,3-propanediamine (where red, grey, white, blue, yellow and paste ball represent oxygen, carbon, hydrogen, nitrogen, sulfur and fluorine respectively)

3.4 Characterization of Shale Samples

The main aim of the experimental study is to validate the outcome of the simulation study. Figure 3.4 illustrates the step-by-step procedure of the experimental study. In this study, experiments have been carried out to investigate the characteristics of shale samples from Eagle ford (EF-1, EF-2), Mancos (MC), and Wolfcamp (WF) shale. Using the Field Emission Scanning Electron Microscope (FESEM) the imaging and qualitative analysis of the shale samples were done. Then with the use of a surface area analyzer and porosimetry system, we will determine the surface area, micro surface area, pore-volume, micropore volume of the shale samples. Helium Porosimeter has been used to measure the porosity and matrix density of the shale samples. TOC is performed to find the total organic content in shale samples.

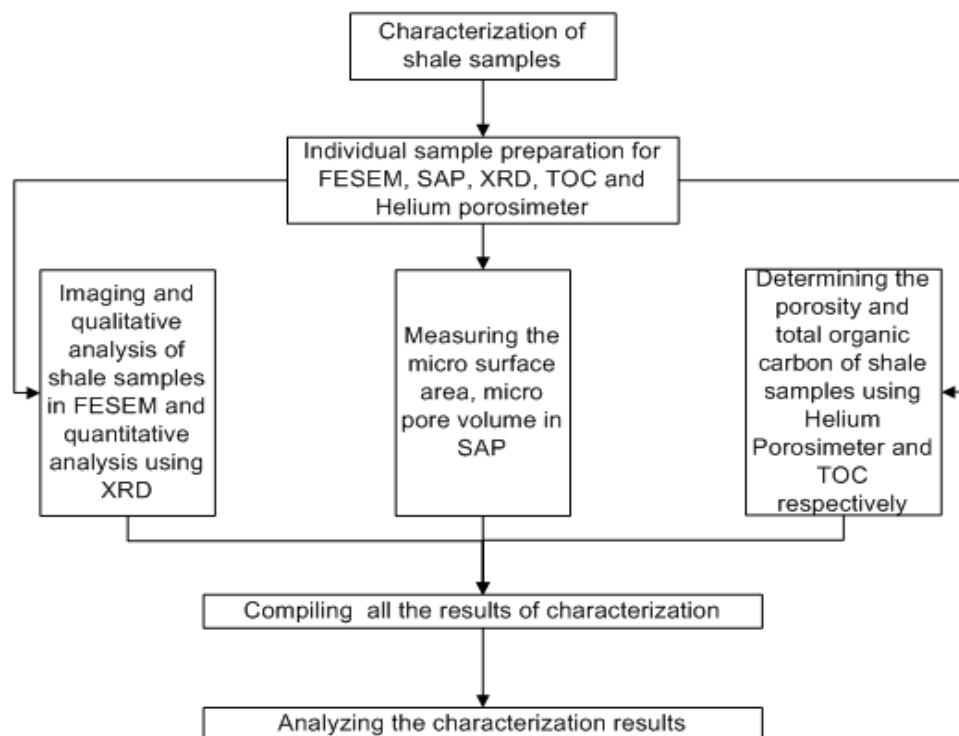


Figure 3.4: Flowchart of experimental methodology

3.4.1 Imaging and Qualitative Analysis Using FESEM

Field Emission Scanning Electron Microscope is generally known as FESEM which works with electrons in lieu of light. The field emission source liberates these electrons to scan the object in accordance with a zig-zag pattern. Microscopic topographic details on the surface and whole or fractioned objects or structures that are as small as 1 nanometre are visualized by a FESEM. To study Deoxyribonucleic Acid (DNA) material in cells, synthetic polymers, and microchips coatings FESEM can be used [157].

Provided nitrile gloves must be worn when handling a sample. Samples should be clean, as small as possible, stable in a vacuum. If needed, samples, stubs, and the specimen holder should be cleaned with isopropanol and Kim wipe papers. Having dispersed powdered shale samples, glass plate/silicon wafer, or any solid substrate must be used on which sample containing solution can be kept. Now, the sample containing substrate glass or wafer should be dried and then can go for FESEM imaging. As shale samples are nonconducting then they must be gold coated onto the sample containing a substrate for a very short time approximately 30-40 seconds. Then a coating of gold or gold-palladium is done with an ultra-thin layer of 1.5nm to 3.0 nm. Powder samples must be mounted firmly on Al-stubs using C-tape. Stubs are needed to be fixed onto the ZEISS specimen holder and eight stubs may be loaded. Thin sections should be mounted directly on the specimen holder. If necessary, maps are made to be used to locate each sample in the SEM. Salt and oils from fingerprints will contaminate the FESEM vacuum and samples if gloves are not worn. and these fingerprints can be removed with isopropanol and Kim wipe.

Figure 3.5 presents the SUPRA 55VP FESEM on which the experiment was carried out and Figure 3.6 shows the schematic diagram of a typical FESEM. FESEM mainly consists of the Field Emission Gun (3), which provides the source of the electron beam, the Condenser Lens (7), used only in special operating modes, the Beam Booster, composed of Anode (5), Vacuum Tube (6), Apertures (8), Alignment Coils (9a,b,c), Stigmator (13), and Isolating Valve (15), the Objective Lens (10,11) which focuses the electron beam onto the specimen (12), also containing the Deflecting System (14) [158].



Figure 3.5: Field emission scanning electron microscopy (SUPRA 55VP)

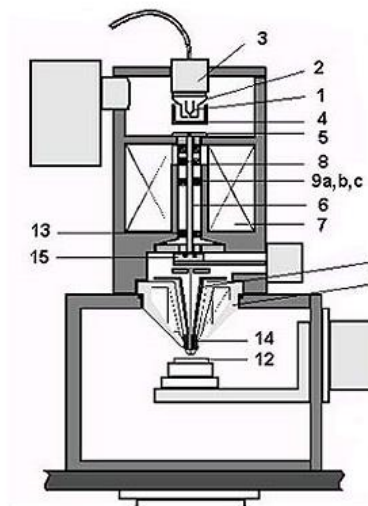


Figure 3.6: Schematic diagram of a typical FESEM [158]

3.4.2 Mineralogy determination using XRD

A quick analytical technique that is used for identifying the phase of a crystalline material and gives information on unit cell dimensions is known as X-ray diffraction. In 1912, the crystalline substances which act as 3D diffraction gratings for the wavelengths of X-ray similar to the spacing of the planes in the lattice of a crystal were discovered by Max von Laue. For studying the atomic spacing and crystal structures

XRD is now a very common experiment. Finely grounded and homogenized material is analyzed, and average bulk composition is determined.

Shale samples, sample holders, and an instrument for grinding are required for determining the unknown. Pure, a few tenths of a gram of the sample are obtained. Then by grinding the shale sample to a fine powdered form (smaller than $\sim 10 \mu\text{m}$ in size is preferred), generally in a fluid to reduce the inducing extra strain that can offset peak positions, and to randomize orientation. Then it is placed into a sample holder. Figures 3.7 and 3.8 show the equipment by which the experiment was carried out and the typical schematic diagram of XRD, respectively



Figure 3.7: X-Ray powder diffraction machine

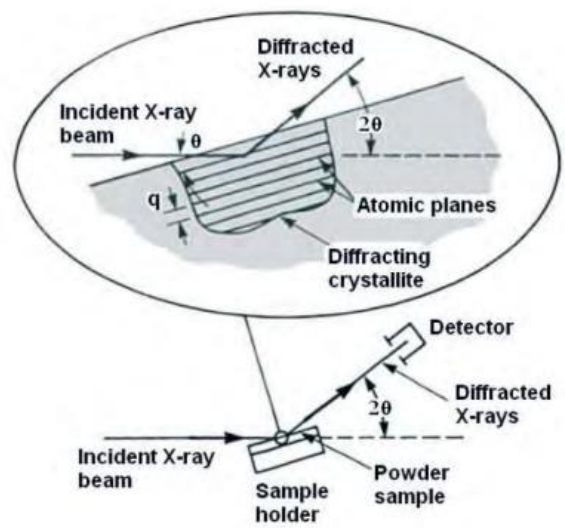


Figure 3.8: Schematic diagram of a typical XRD [159]

3.4.3 Micro Surface Area and Micro Pore Volume Determination using SAP

Surface area and pore size of aerogels and xerogels are measured using Surface Area Analyzer and Porosimetry System. The gaseous physical adsorption principle is utilized in this system. Firstly, degassing of the sample is done using vacuum, N_2 , or heat to discard contamination of surface and adsorbed species. A probe gas (generally N_2) known as aliquots, is used at cryogenic temperatures ranging between (-195.79°C to -50°C) and dosed up to saturation pressure. The instrument measures values of pressure, temperature, and volume. To calculate the properties of the porous material from this data various models are used.

Firstly, samples are needed to be prepared for degassing. Selecting a sample tube of 12.7mm diameter and seal frit. Then filling the cold trap Dewar with liquid nitrogen. Measuring the level of liquid nitrogen with a dipstick to about 5cm (2in) from the top. After that Cold trap, Dewar is then mounted to ASAP 2020. It must be checked and confirmed that the gas pressure regulators are set to 10 psi. The apparatus needed for this experiment are Micromeritics ASAP 2020, AnD Gr200 Analytical Balance, Fluke 51 Series 2 Thermometer, Digital Barometer, Sample Tube 12.7mm, Glass Filler Rod, and Seal Frit. The reagents needed for this experiment are as follows: Liquid Nitrogen (P_o is not more than 2666.45 Pa above barometric pressure), Purified Nitrogen Gas (at least 99.9% pure), Purified Helium Gas (at least 99.9% pure). Figure 3.9 and Figure 3.10 show the SAP by which the experiment was carried out and a typical schematic diagram of SAP, respectively.



Figure 3.9: Surface area analyzer and porosimetry system

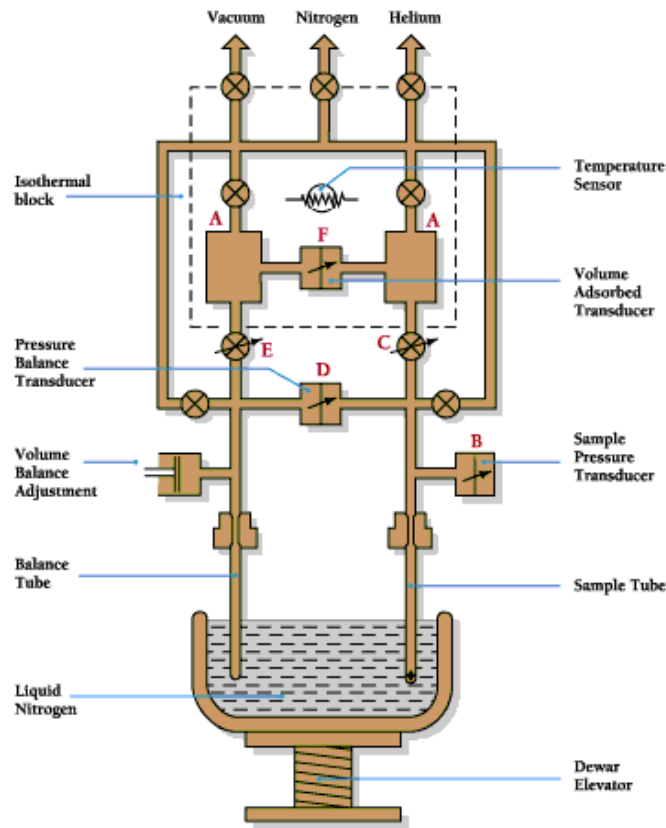


Figure 3.10: Schematic diagram of a typical SAP [160]

3.4.4 Porosity Measurement using Helium Porosimeter

Methods of porosity measurement are dependent either on fluid extraction from rock or fluid introduction into pore spaces of rock. Helium porosimeter is used for measuring the porosity of core samples that have been taken from different reservoirs, at an ambient condition. Fluids can pass through the interconnected pore space, which is expressed as a percentage of the total volume occupied by the interconnecting interstices.

Helium expansion porosimeter is designed for rapid and precise determination of the effective porosity of reservoir core samples of 1-1.5 cm diameter using Boyle's law of gas expansion. Firstly, the length and diameter of the core are measured using a caliper. Then the porosimeter is given a helium supply at a pressure of 1000 kPa. For determining the volume of the matrix cup having a core, the dried and cleaned core is kept inside the cup and is mounted in the cupholder. Then the source is opened, and helium gas is supplied. The needle is regulated at 100. After that, the source is closed

and then the supply. Then opening the core holder reading is taken on the top scale in cm^3 . Now for determining the volume of the matrix cup having no core, the core is taken out from the matrix cup, and it is mounted, cupholder. Then again, the source is opened, and helium gas is supplied. Opening the cell, the needle is regulated at 100. After that, the source is closed and then the supply. The core holder is then open and the reading is taken on the middle scale in cm^3 [161]. Figure 3.11 presents the helium porosimeter by which the experiment of the current study was carried out and Figure 3.12 shows the schematic diagram of a typical helium porosimeter.



Figure 3.11: Helium Porosimeter

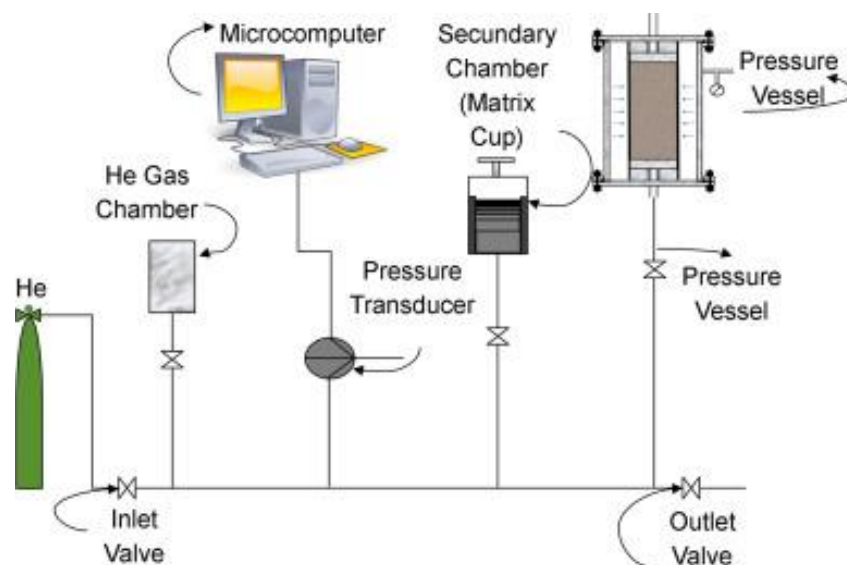


Figure 3.12: Schematic diagram of helium porosimeter [162]

3.4.5 Total Organic Carbon (TOC) Measurement

The total organic carbon (TOC) of four samples was calculated by a TC analyzer. The samples were powdered and dried at 60°C for 24 hours to dehydrate them. To discard the total inorganic carbon (TIC), hydrochloric acid with a concentration of 37% was used to treat 2 g each of all the samples. Then these samples were washed with distilled water and further dried for 12 hours at a temperature of 60°C. A minimal quantity of about 0.63 g of each sample was fed to the analyzer to measure the TOC. Figure 3.13 shows the TC analyzer used for this experiment.



Figure 3.13: Total organic carbon analyzer

3.5 Molecular Simulation and Modelling

This molecular simulation work can be divided into three major parts such as molecular shale model preparation, solubility of viscoelastic surfactant (VES) in supercritical carbon dioxide (Sc-CO₂), and thickening of Sc-CO₂, and investigation of preferential adsorption capacity of thickened Sc-CO₂ over CH₄ in molecular shale model. Firstly, the study was initiated by preparing a heterogeneous molecular shale model consisting of kerogen type II D, montmorillonite (MMT), illite, and quartz. Then, the molecular model has been validated against the properties such as density, the

weight percentage of elements, surface area, and cumulative volume of experimental shale samples (i.e., Eagle ford, Mancos, and Wolfcamp formations). Secondly, the solubility of VES (i.e., N-ETFOSA and N,N,N'-TM-1,3-PDA) in Sc-CO₂ was checked using Blend simulation and the viscosity of thickened Sc-CO₂ is measured using Forcite simulation. Experimental data from literature were also simulated to validate the viscosity simulation, Finally, preferential adsorption of thickened Sc-CO₂ over CH₄ is investigated by using Sorption module and Forcite simulation. To validate the adsorption simulation, experimental literature data was simulated.

3.5.1 Basic Molecular Simulation

Figure 3.14 presents an algorithm for performing molecular dynamics simulation. The inputs to the algorithm are the initial position and velocity vector defined by r and V . Then the energy, U is calculated by different models such as the Lennard-Jones model. The energy of deformation of bond lengths, bond angles, torsion angles, out-of-plane interactions, vibrational frequencies, non-bond interactions, and the dynamic properties of molecules have calculated the model under the assigned forcefields such as COMPASS, UNIVERSAL, CVFF, etc. Then the force, F is determined from the energy U by taking gradients. After that acceleration, a is calculated by Newton's law of motion, dividing the force of the elements by the mass of the elements. Then, using numerical integration, the acceleration is integrated into the new velocity, and the velocity is integrated into the new position for small-time change dt . Thus, this iteration cycle goes on to find the final position and velocity of the element.

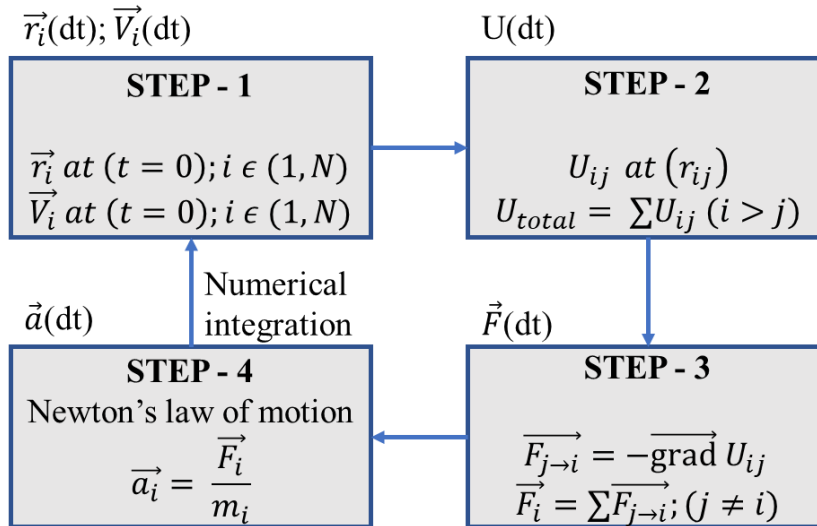


Figure 3.14: A basic molecular dynamic simulation cycle.

3.5.2 Molecular Shale Model Preparation

In this sub-section, the details of organic matter, clay minerals, non-clays minerals, and shale model parameters have been discussed. Moreover, the simulation work has also been described in detail.

3.5.2.1 Molecular shale model

The molecular shale model used in this study was proposed by Kawthar et al. [163] which consists of kerogen type II D, montmorillonite (MMT), illite, and quartz. At the start, an accurate and flexible forcefield is chosen for the study. Then the topology of the complex shale matrix comprising of Kerogen type -II, montmorillonite, and illite is generated. Figure 3.15 shows the structural unit cell of kerogen type II D, montmorillonite, illite, and quartz, respectively. Kerogen represents the organic matter found in shale, quartz represents non-clay minerals and illite, and MMT represents clay minerals. The type II D kerogen unit model used in this study has a chemical formula of $C_{175}H_{102}O_9N_4S$ and it was prepared by Ungerer et al. [164]. This model by Ungerer et al. [164] has also been adopted in other research works [165]. The MMT used in the shale model has a unit chemical formula of $Si_8Al_4O_{20}(OH)_4$. The illite in the model was

adopted from Gualtieri et al.'s [166] illite crystal structure with the main K⁺ interlayer species [167] while the quartz was obtained from the material studio database.

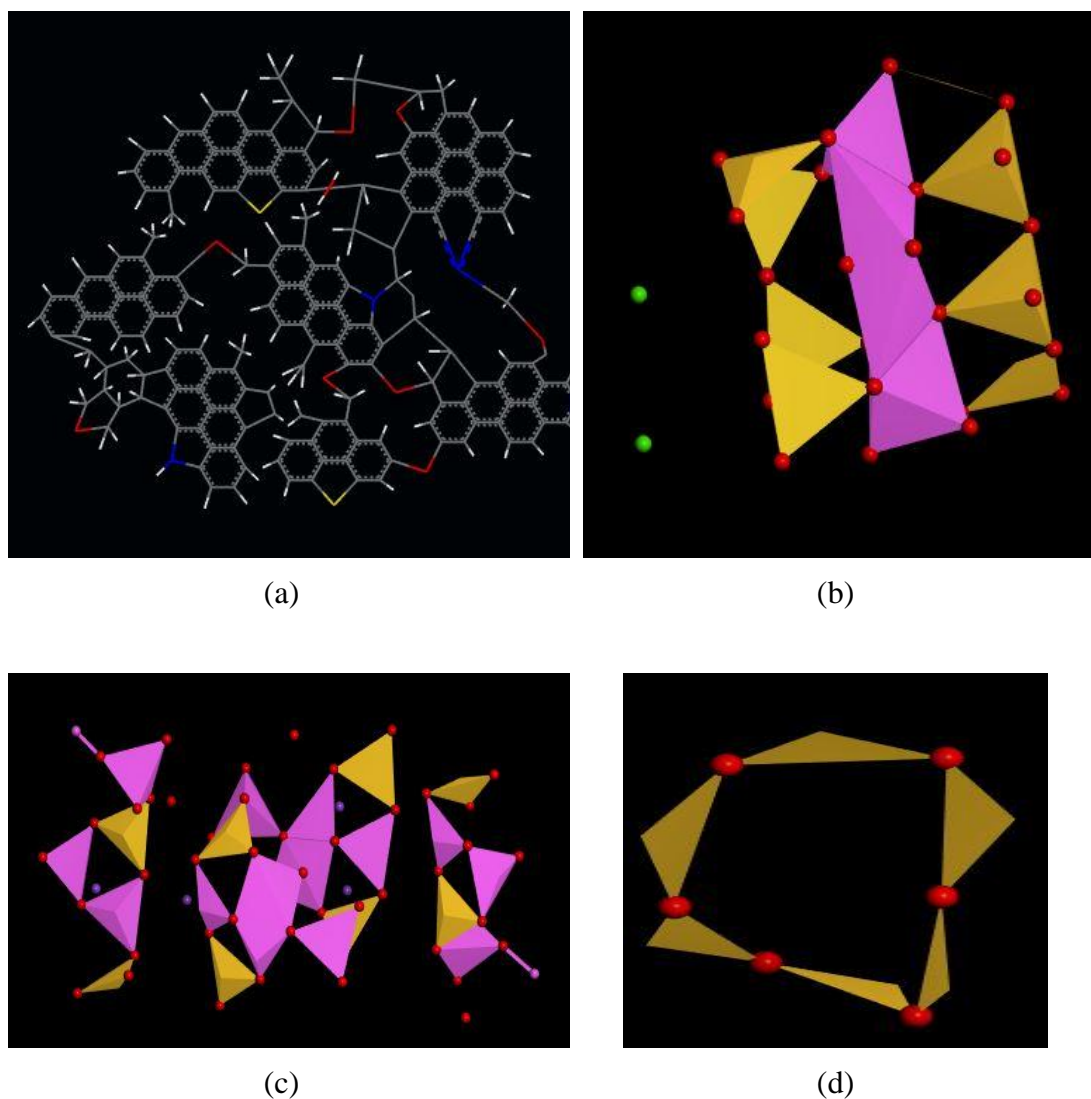


Figure 3.15: Structural unit cell of (a) kerogen type II D [164], (b) montmorillonite, (c) illite, and (d) quartz

The organic and inorganic content of shale are kerogen and clay surface have not been used as two distinctive surfaces rather a mixture is made out of kerogen type II D, montmorillonite, illite, and quartz to use as two surface layers. This was done using the amorphous packing option in the material studio and by choosing the UNIVERSAL forcefield. The amorphous packing task allows the packing of selected molecules into a 3D periodic structure in a specified composition. This task allows the creation of complex multiphase and or heterogeneous structures made up of different mineral types. Figure 3.16 demonstrates the molecular shale model in layers. Moreover, the

effect of confinement on the adsorption behavior of gases on the molecular shale model using the concentration profile was investigated in our previous paper because the model was developed into slit nanopores (size $50 \text{ \AA} = 5 \text{ nm}$) and these nanopores contribute to gas uptake.

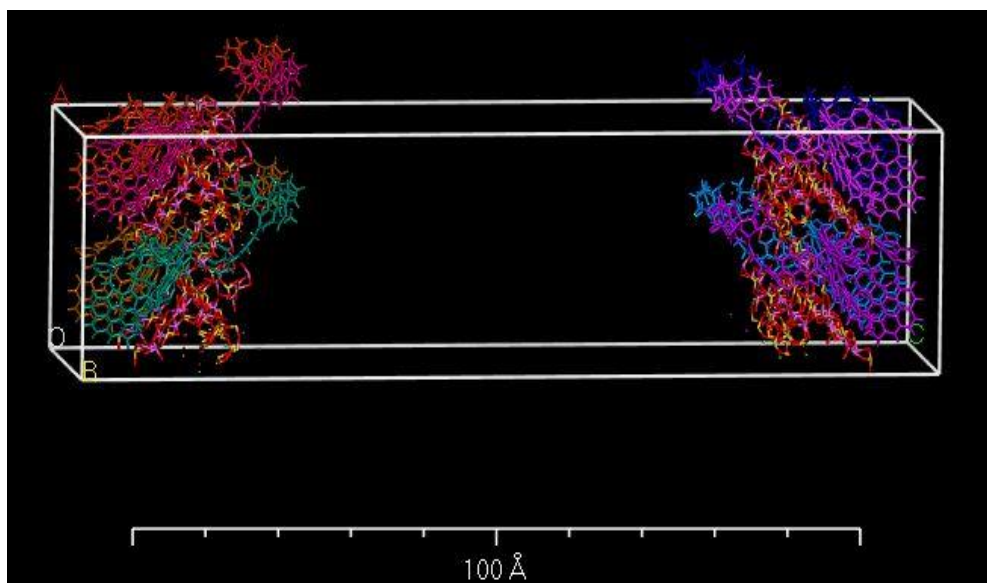


Figure 3.16: Final shale model in layers.

3.5.2.2 Simulation details

This simulation work was carried out using Accelrys supplied Material Studio software [168]. The atom-based summation, Ewald summation, and velocity Verlet algorithm have been used to optimize the geometry, to maintain the equilibrium and production phase, and to measure the time integrator algorithm, respectively. For organic and inorganic matters, COMPASS and UNIVERSAL force fields have been used, respectively. For atomic simulation studies, the COMPASS force field [169] is an optimized molecular potential that is appropriate for organic matters. The UNIVERSAL force field [170], on the other hand, has parameters for each atom of the periodic table with a maximum of 103 atomic numbers. This versatility enables the UNIVERSAL forcefield to extend to a wide variety of structures, demonstrated in assessments of inorganic molecules and metal complexes [171]. For the prediction of structural variations and vibrations, the COMPASS force field is applied to the cross-coupling term and the UNIVERSAL forcefield infers the topological evenness of the

simulated arrangement and therefore can be classified among non-reactive force fields [172, 173].

Taylor's Verlet expansion algorithm is used for the explicit measurement of velocity which can influence constant pressure simulation. This enables relatively long-term steps to be used as position (r), speed (v), and acceleration (a) which are simultaneously measured at a very high degree of accuracy. The software developer also uses this algorithm because it can conserve energy by numerically stable and time-reversible properties [174]. In the measurement of atomic motion, the Verlet algorithm was used.

Four key measures were included in the procedures for MD simulation. The molecular structure design and optimization was the first step. The construction of a simulation box, simulation of an equilibrium and production process, and finally the analysis of the trajectory output [175] are the next three respective steps. The Lorentz-Berthelot laws were applied to all the interaction parameters. Canonical ensemble NVT was used to keep N , V and T fixed. Kerogen, MMT, illite, and quartz atoms remain fixed throughout the simulation. After the ensemble achieves equilibrium, the pores stabilize to a certain value. Periodic boundary conditions apply to three directions.

The possible function of Lennard-Jones is used to define non-bonds, with a cut-off distance of 12\AA . The Particle Mesh Ewald (PME) method was used to measure long-range electrostatic forces and energies [176]. The Langevin system is used with a $5/\text{ps}$ damping factor to regulate the temperature [177]. The timestep and total operating time are 1 fs and 3 ns respectively. For balancing the NVT ensemble, the first two ns are used, and the second one ns is used for analysis. The sequence of building heterogeneous shale in the materials studio environment is shown in Figure 3.17. The shale model has the cell parameters $a=30.07\text{ \AA}$, $b=30.07\text{ \AA}$, and $c=119.17\text{ \AA}$ and a slit pore of 50\AA .

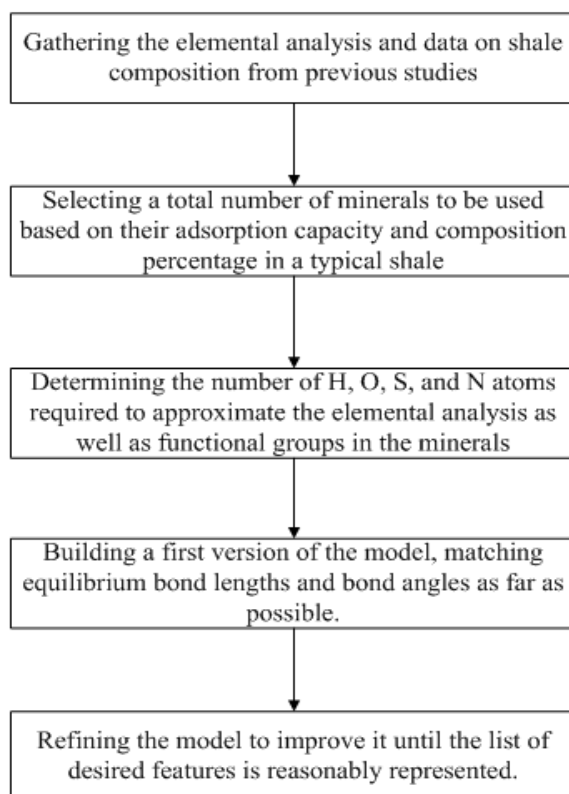


Figure 3.17: Sequential of building heterogeneous shale in Materials Studio environment.

3.5.3 Viscosity Enhancement of Sc-CO₂ using VES

This sub-section is consisted of details of solubility screening of VES in Sc-CO₂, viscosity calculation simulation, and the experimental validation of the viscosity simulation.

3.5.3.1 Solubility screening of VES in Sc-CO₂

Blend simulation was used to check the solubility of N-ETFOSA and N,N,N'-TM-1,3-PDA in Sc-CO₂ at a temperature and pressure of 305 K and 7400 KPa. Firstly, the structures of CO₂, N-ETFOSA, and N,N,N'-TM-1,3-PDA were made using the chemical formula and crosschecked with other features such as density. The chemical formulas of N-ETFOSA and N,N,N'-TM-1,3-PDA are C₁₀H₆F₁₇NO₂S and C₆H₁₆N₂, respectively. In a Blend calculation, polymer-polymer, polymer-solvent, or solvent-

solvent interactions are screened. In this case, surfactant-solvent interaction has been checked. The surfactant is defined by specifying head and tail atoms on a monomer repeat unit.

Before submitting to the Blends calculation, the geometries of the surfactant and gas structure have been optimized. Using the Forcite module geometry of the structures is optimized by choosing DREIDING forcefield and QEq charge. After the optimization of Sc-CO₂, N-ethyl perfluorooctyl sulfonamide, and N,N,N'-Trimethyl-1,3-propanediamine, the optimized 3D structures are used to run the Blends calculation. In the Blending operation, Sc-CO₂ was selected as the base, and N-ETFOSA and N,N,N'-TM-1,3-PDA were taken as the screen. The next stage is to adopt the task in Blend calculation which are Mixing, Binding energies, and Coordination number. In this study, Mixing was chosen for performing both coordination number and binding energy calculations which forecast interaction energy, chi parameter, and mixing energy. In the Mixing Task head and tail, atoms are set as noncontact in repeat units. Next, a request was made to save the lowest energy setting in Blends in a 3D atomistic trajectory document for all bases and screens. Setting the forcefield and charge to DREIDING and QEq the Blend calculation can then be made.

3.5.3.2 Viscosity measurement

Forcite module was used in measuring the viscosity in molecular simulation of CO₂, Sc-CO₂, N-ETFOSA, N, N, N'-TM-1,3-PDA, the mixture of CO₂ and N-ETFOSA, the mixture of Sc-CO₂ and N-ETFOSA, the mixture of CO₂ and N,N,N'-TM-1,3-PDA, and the mixture of Sc-CO₂ and N,N,N'-TM-1,3-PDA. In the first step, geometry optimizations of the structures were done using the UNIVERSAL forcefield, current charge, and setting the quality to fine. Atom-based summation method, Ewald summation method, and velocity Verlet algorithm were used as setting parameters for geometry optimization, equilibrium and production phase, and time integrator algorithm calculation. After the geometry optimization, energy simulation was run using the previous setup.

Available MDS are categorized by the ensemble names, NVE, NVT, NPT, and NPH, where N, T, E, V, H, and P are the constant number of molecules, constant temperature, constant energy, constant volume, constant enthalpy, and constant pressure. In the next step using the canonical ensemble (NVT), the Forcite dynamics are run in the previous setup except for the temperature. The temperature was set to 298 K for the gaseous state of CO₂ and liquid state of N-ETFOSA and 305 K for the supercritical state of CO₂. After completion, the amorphous cell was created. In this study, the density of CO₂, N-ETFOSA, and N,N,N'-TM-1,3-PDA is used as 0.001836 g/cm³ [154], 1.7 g/cm³ [155], and 0.793 g/cm³ [156], respectively.

The loading used for CO₂, Sc-CO₂, N-ETFOSA, and N,N,N'-TM-1,3-PDA are 100, 100, and 10, respectively. A loading ratio of 10:1 was used in the mixture of CO₂ and N-ETFOSA, CO₂ and N,N,N'-TM-1,3-PDA, Sc-CO₂ and N-ETFOSA, and Sc-CO₂ and N,N,N'-TM-1,3-PDA. After creating the amorphous cell again, the Forcite dynamics simulation was performed using isobaric isothermal ensemble (NPT) and the previous setup of forcefield and charge. The temperature and pressure were set to 298 K and 100 KPa for the gaseous state of CO₂ and liquid state of N-ETFOSA and N,N,N'-TM-1,3-PDA, and 305 K and 7400 KPa for the supercritical state of CO₂. After the completion of NPT ensembled Forcite dynamics simulation, Forcite shear simulation was done using the similar setup, pressure, and temperature. Thus, the viscosity of each structure and phase was determined.

3.5.3.3 Experimental validation of viscosity simulation

Validation helps to ensure that the model reflects the real field scenario precisely. The experimental work of Xiong et al has been imitated in simulation to validate the current viscosity simulation of this study [178]. In their study, they experimentally investigated the viscosity of Sc-CO₂ using 1 weight percent of poly(dimethylsiloxane) at temperatures such as 380 K, 400 K, and 420 K and pressure ranging from 40-60 MPa. For the validation, this experiment has been simulated at 380 K temperature and 45-60 MPa pressure. In the 3.5.3.2, the details of viscosity measurement using Forcite simulation are provided.

3.5.4 Adsorption Simulation Details

This sub-section comprises the details of adsorption simulation and the experimental validation of the adsorption simulation.

3.5.4.1 Adsorption simulation

At a temperature and pressure of 305 K and 10 kPa to 7400 kPa respectively, adsorption simulations were executed. After the topology of the molecular shale, the model was built, the Grand Canonical Monte Carlo method was implied to simulate the adsorption of methane, supercritical carbon dioxide, and thickened supercritical carbon dioxide using N-ETFOSA and N,N,N'-TM-1,3-PDA respectively on the molecular shale model built into slit pores. To calculate coulombic interactions, the Ewald summation approach and atom-based Van der Waals interactions were implemented, and an Andersen thermostat was imposed on the temperature control [179, 180]. For energy minimization and equilibration, stages have been calculated and analyzed by Forcite calculation where canonical ensemble NVT and isobaric isothermal ensemble NPT were used simultaneously. For attaining the equilibrium state at every pressure point of adsorption isotherm first 5×10^6 steps are executed and on the other hand 1×10^7 steps are required for the production stage. The adsorption capacity achieved from the simulation was fitted using the Langmuir adsorption model given in Equation 3.1.

$$n^a = n_{max}^a \frac{b}{1 + bp} \quad (3.1)$$

where, b = Langmuir constant, n^a = absolute adsorption capacity, n_{max}^a = Langmuir maximum adsorption capacity, and p = pressure.

3.5.4.2 Experimental validation of adsorption simulation

To validate the adsorption simulation, a comparison of the simulation result of CH₄ and CO₂ adsorption on the proposed shale model with experimental CH₄ and CO₂ adsorption data have been carried out. The experimental data for high-pressure CH₄ adsorption on Posidonia shale and for high-pressure CO₂ adsorption on Parana shale were obtained from the work of Rexer et al. [181] and Liu et al. [182], respectively.

The simulations were performed at a temperature of 318K for both and pressure of up to 12 and 16 MPa for CH₄ and CO₂, respectively. The result obtained from the simulation shows absolute adsorption capacity while excess adsorption capacity is obtained from the laboratory. Hence, Equation 3.2 has been used to obtain the excess adsorption isotherms and compare the simulation results with the experimental results [183],

$$n_{ex} = n_{ab} - \frac{\rho V}{M} \quad (3.2)$$

where n_{ex} is the excess adsorption, mol/kg; n_{ab} is the absolute adsorption, mol/kg; the V is the pore volume, m³/kg; the ρ is the equilibrium density of methane calculated using the Peng-Robinson equation, kg/m³; and M is the molar mass of the gas, kg/mol. In 3.5.4.1, the details of the adsorption simulation are provided.

3.6 Summary

This chapter provides an in-depth overview of the experimental and simulation methodology of the current study. In this study, experiments have been carried out to investigate the characteristics of shale samples from Eagle ford (EF-1, EF-2), Mancos (MC), and Wolfcamp (WF) shale. This characterization consists of imaging and qualitative analysis, mineralogy evaluation, determination of pore size distribution, micro surface area and micropore volume, measurement of porosity, matrix density, and total organic carbon. On the other hand, molecular simulation work can be divided into three major parts such as molecular shale model preparation, solubility of viscoelastic surfactant (VES) in supercritical carbon dioxide (Sc-CO₂) and thickening of Sc-CO₂, and investigation of preferential adsorption capacity of thickened Sc-CO₂ over CH₄ in molecular shale model.

CHAPTER 4

RESULTS AND DISCUSSION

4.1 Introduction

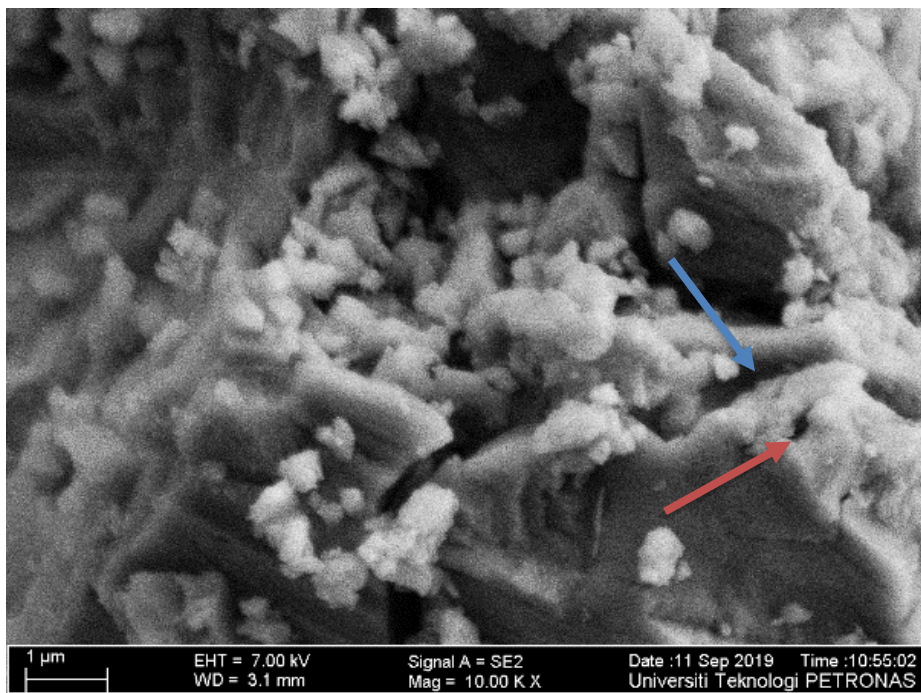
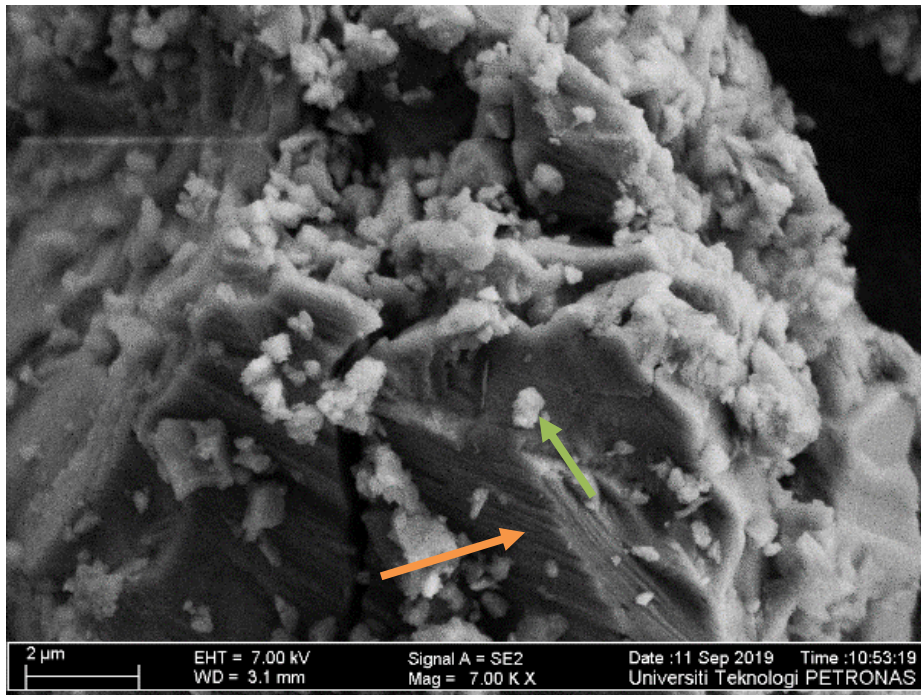
In this chapter, the characterization (imaging and qualitative analysis, elemental analysis, mineralogy analysis, pore size distribution, micro surface area, and micropore volume determination, porosity and density measurement, and total organic carbon determination) results of shale samples (EF-1, EF-2, MC, AND WF) have been thoroughly discussed. Then the simulation results of the solubility screening of VES in Sc-CO₂ and thickening of Sc-CO₂ have been investigated. Furthermore, for understanding the implication of Sc-CO₂ in waterless fracturing, the adsorption of thickened Sc-CO₂ and CH₄ on the molecular shale model has been studied and analyzed.

4.2 Characterization of Shale Samples and Model Validation

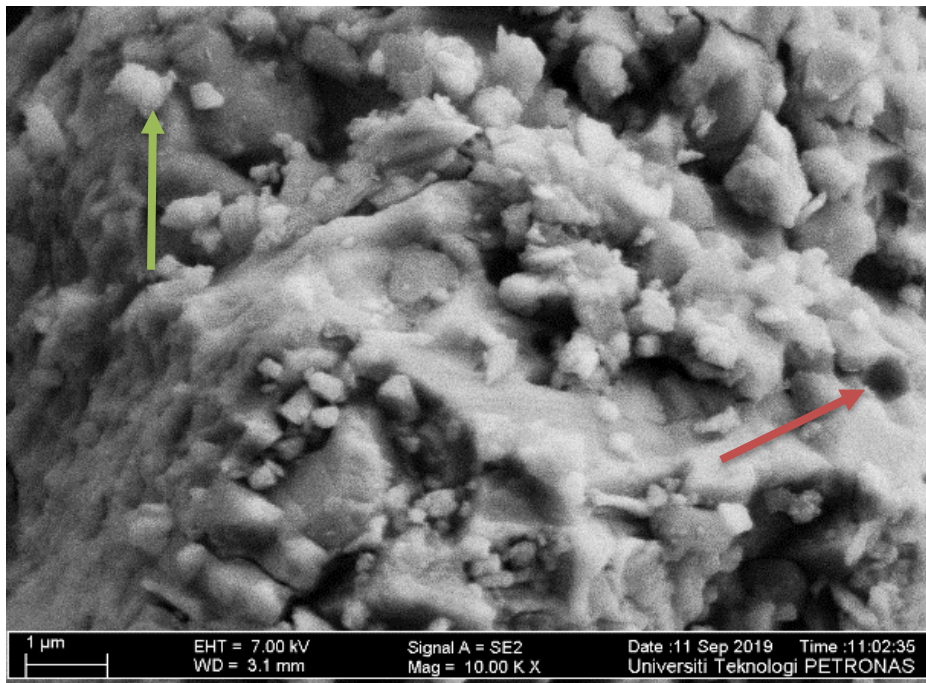
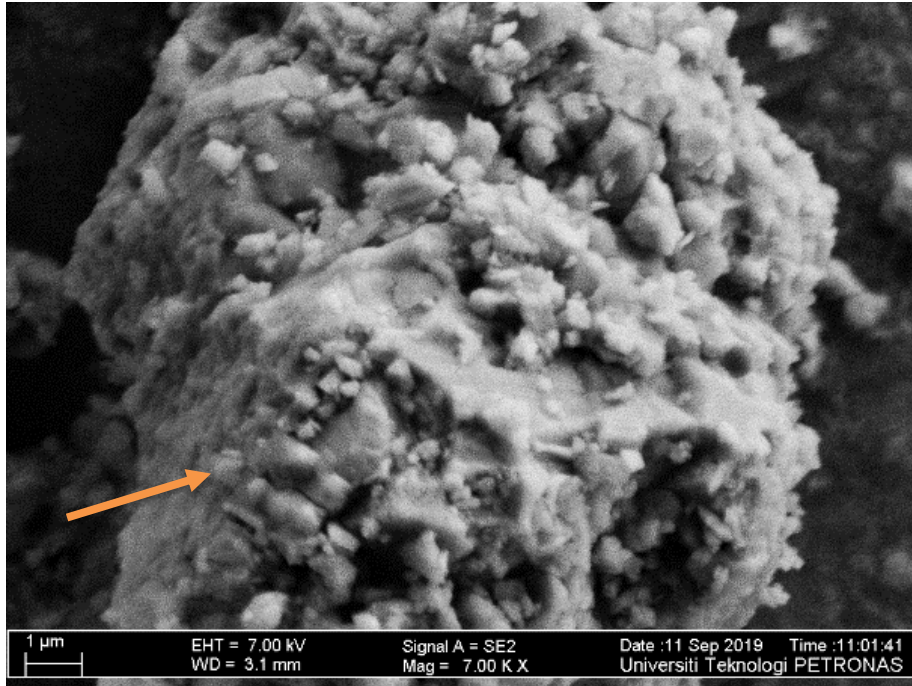
This section describes the characterization of shale samples such as Eagle ford (EF-1, EF-2), Mancos (MC), and Wolfcamp (WF). This characterization consists of imaging and qualitative analysis, identification of crystalline phases presents in the material, and determination of surface area, micropore volume, porosity matrix density, and total organic carbon content. These experimental studies involved the use of field-emission scanning electron microscope (FESEM), surface area analyzer and porosimetry system (SAP), Helium Porosimeter, and total carbon analyzer to characterize the shale samples. Later this characterization results have been utilized to validate the properties of the molecular shale model.

4.2.1 Imaging and Qualitative Analysis and Mineralogy Evaluation

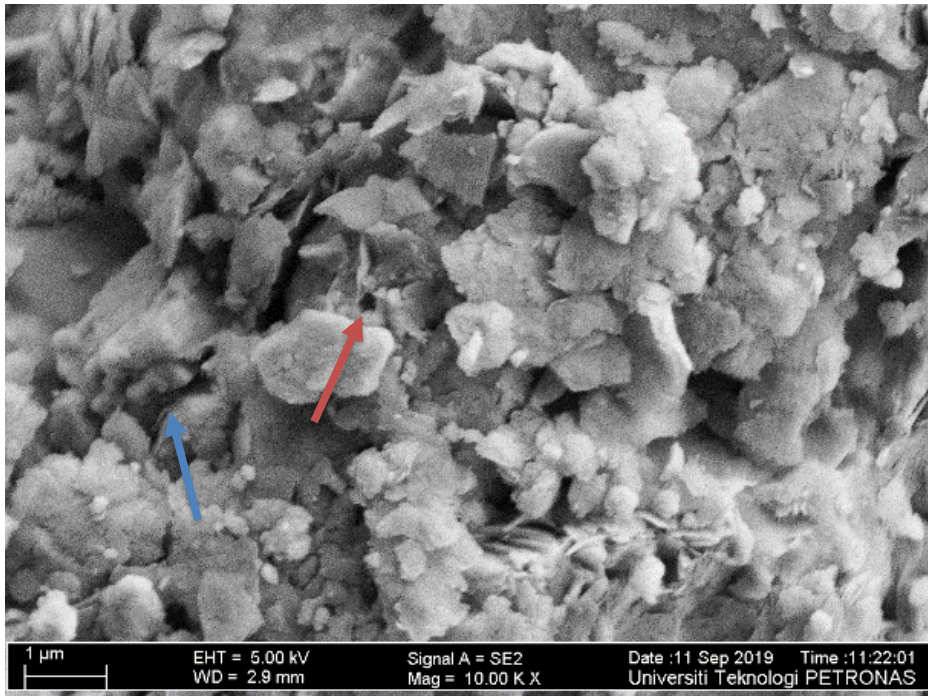
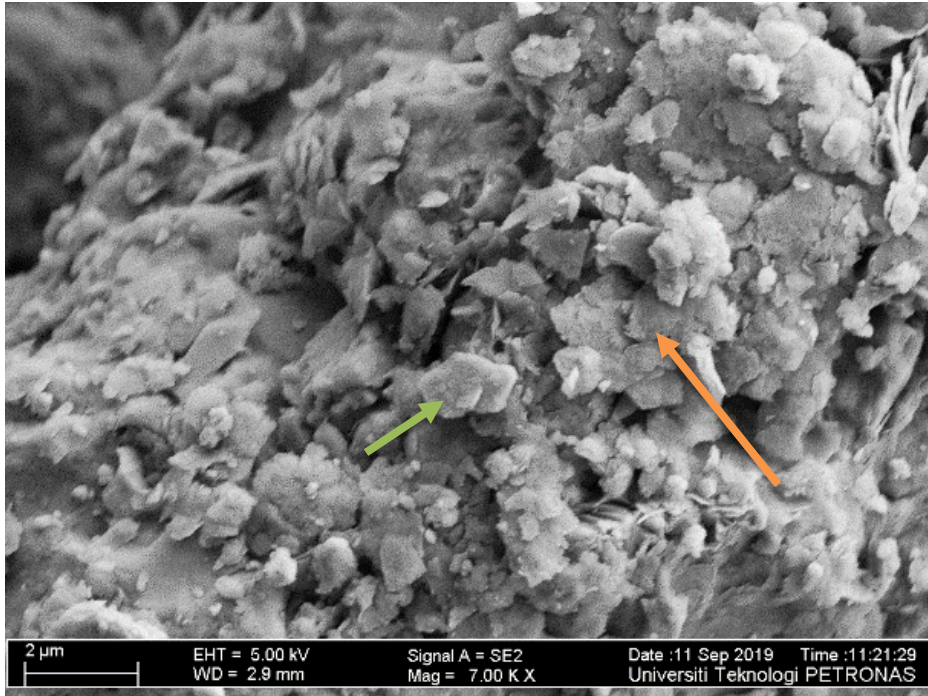
A field emission scanning electron microscope has been used to derive the images in Figure 4.1.



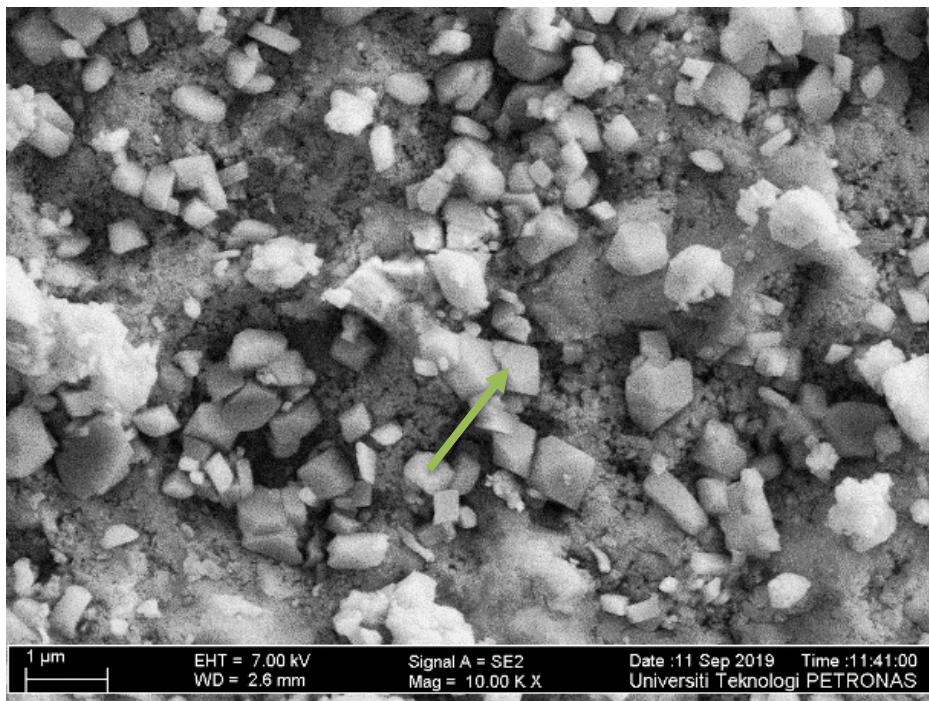
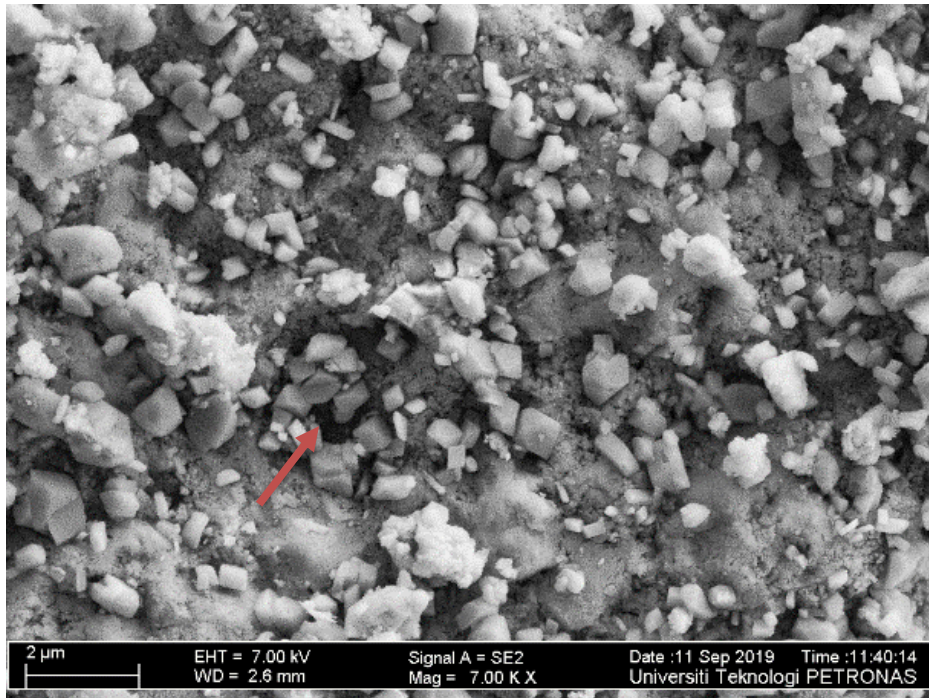
(a)



(b)



(c)



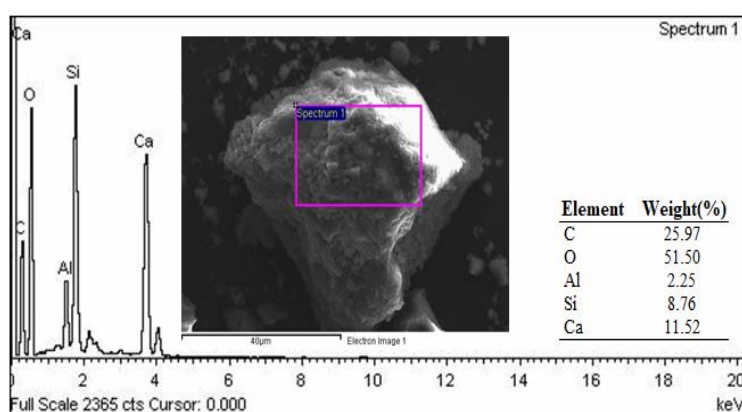
(d)

Figure 4.1: FESEM images of (a) EF-1, (b) EF-2, (c) MC, and (d) WF shale samples in 7K and 10K magnification (left to right) respectively

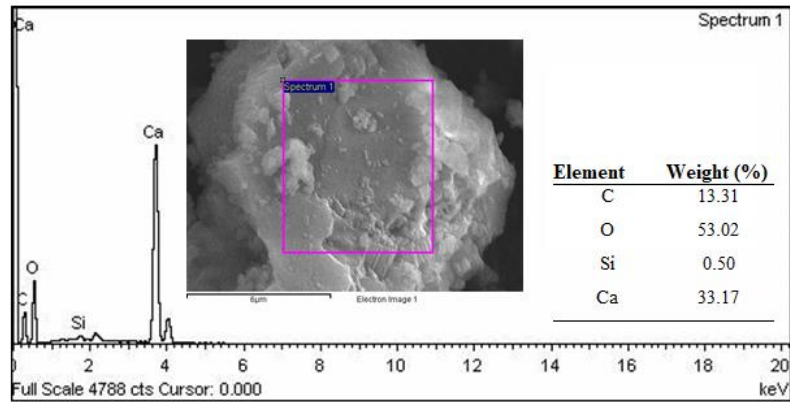
Table 4.1: Mineralogy of shale samples

Sample ID	Clay minerals (%)	Non-clay minerals (%)
EF-1	30.8	69.2
EF-2	34.5	65.5
MC	39.3	60.7
WF	29.2	70.8

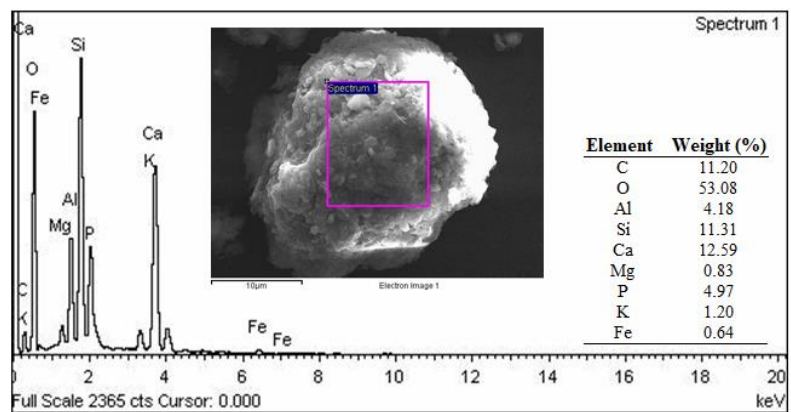
The sheet-like shape in Figure 4.1 shown by the orange arrow is an indication of the presence of clay minerals. From the EDX results, it can be seen that there is the presence of calcium, silicon, aluminum, potassium which are the major components of clay such as kaolinite and smectite. The cubic shape marked with the green arrow in the figure indicates the presence of non-clay minerals such as quartz which is also validated by the presence of silicon in EDX results. There are fractures and pores evident and marked with blue and red arrows. From Figure 4.1 according to the range pore size defined it can be said that these pores are mesopores (0.002 - 0.05 μm). The mineralogy of shale samples has been measured using XRD and the results are tabulated in Table 4.1. From the table, it can be seen that all these shale samples are richer in non-clay minerals than clay minerals. To compare the XRD results with the EDX spectra for all these samples has been presented in Figure 4.2. According to the respective spectrum of all these shale samples, there is the presence of C, O, Al, Si, Ca, Mg, Fe, and K which indicates the presence of organic matter, quartz, and clay minerals.



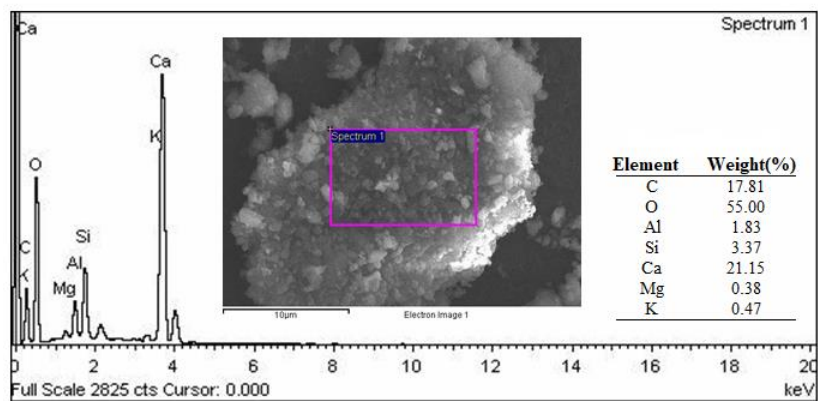
(a)



(b)



(c)



(d)

Figure 4.2: EDX spectra of (a) EF-1, (b) EF-2, (c) MC, and (d) WF shale samples showing elemental composition with an embedded FESEM images

4.2.2 Elemental Analysis

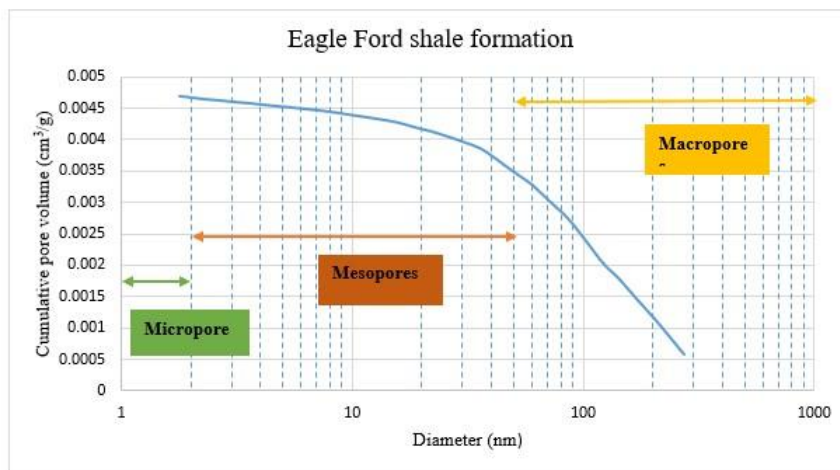
Table 4.2 shows the elemental analysis of shale samples using Energy Dispersive X-ray Analysis (EDX) and the simulated shale model as well. According to the experimental results, it can be seen that the carbon content of shale samples is not so high except EF-1. However, from EDX there is no trace of hydrogen that can be found which eliminates the possibility of the presence of organic matter. On the other hand, the molecular shale model has almost a similar carbon content as EF-1, but it also has the prominent presence of hydrogen. The higher amount of oxygen present in shale formation indicates organic debris decay. The simulated shale model has a lower amount of oxygen than the actual shale which also provides a better condition for oil gas generation [184]. In the case of clay minerals such as Aluminum, Silicon, Potassium simulated shale model has a resemblance to the actual experimental shale samples. Although the experimental results have a higher amount of calcium than the simulated model, this is due to the presence of other clay minerals in the actual shale sample which has not been taken into consideration in the simulation work. There is also the presence of sulfur in the simulated shale model which indicates impurity as the actual producing shale formation tends to have. Although there are only a few clay minerals considered in the molecular shale model yet from this analysis it can infer that it is one of the best possible matches with actual shale. This elemental analysis of the simulated shale model is validated by the experimental results and presenting a better prospect for future research.

Table 4.2: The experimental and simulated weight percentage of elements

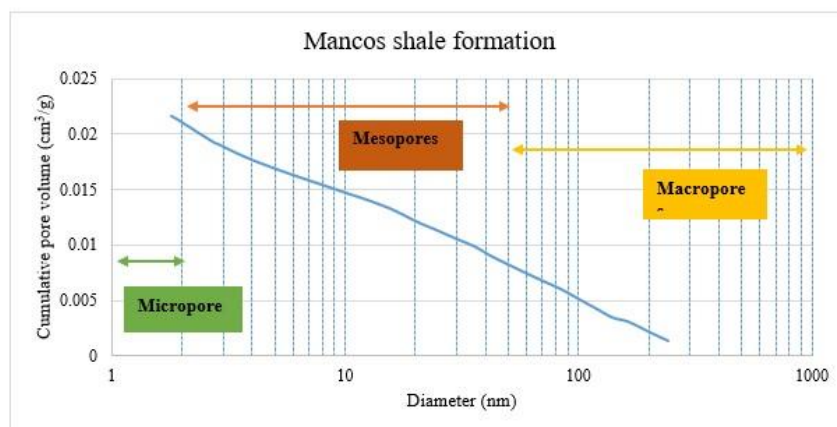
Elements	Weight percentage (%)				Molecular model	shale
	EF-1	EF-2	MC	WF		
Carbon (C)	25.97	13.31	11.2	17.81	25.14	
Oxygen (O)	51.5	53.02	53.08	55.0	37.5	
Hydrogen (H)	0	0	0	0	14.66	
Calcium (Ca)	11.52	33.17	12.59	21.15	0.57	
Aluminum (Al)	2.25	N/A	4.18	1.83	10.34	
Silicon (Si)	8.76	0.5	11.31	3.37	8.62	
Potassium (K)	N/A	N/A	1.2	0.47	2.3	
Magnesium (Mg)	N/A	N/A	0.83	0.38	N/A	
Phosphorus (P)	N/A	N/A	4.97	N/A	N/A	
Iron (Fe)	N/A	N/A	0.64	N/A	N/A	
Nitrogen (N)	N/A	N/A	N/A	N/A	0.57	
Sulphur (S)	N/A	N/A	N/A	N/A	0.29	

4.2.3 Micro Surface Area and Micro Pore Volume determination

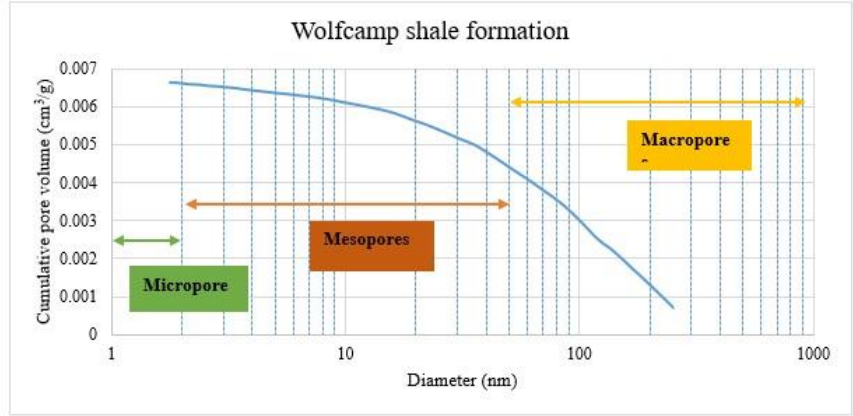
In Figure 4.3, it is shown that most of the pores of the Eagle Ford – 1, Mancos, and Wolfcamp shale samples lie within the range of mesopores (0.002 - 0.05 μm) and macropores ($>0.05 \mu\text{m}$). These results from SAP validate the results from FESEM imaging. The surface area and cumulative volume of the shale samples such as EF-1, MC, and WF have been calculated using Micromeritics ASAP 2020 and for the simulated shale model and its every component, these have been determined using the Atom Volumes & Surface function of Materials Studio. These results have been presented in Table 4.3. The simulated model has predicted the surface area and volume very much in the range of experimental values and this also provides another validation for the proposed model.



(a)



(b)



(c)

Figure 4.3: The pore size distribution of (a) EF-1, (b) MC, and (c) WF shale samples

Table 4.3: Surface area and cumulative volume of shale samples and shale model.

Sample	Surface area (m ² /g)	Cumulative volume (cm ³ /g)
EF-1	540.2255	0.4914
MC	368.8871	0.3757
WF	395.1289	0.3515
Simulated shale model	507.7438	0.4348

4.2.4 Porosity and Density Measurement

The density of the molecular model is an important criterion for determining its reasonableness [185, 186]. A typical shale has a density ranging from 2.06 - 2.67 g/cm³ [163], and the resulting model in this work was 2.3 g/cm³. The consistencies of these values with experimental data prove the validity of the model as well as the forcefield applied for the simulation. The experimental and simulated porosity and matrix density values have been shown in Table 4.4. Aguilera [187] and Wang and Reed [188] reported a porosity value of 12 for Haynesville shale which is relatively close to values reported in this study. The differences in experimental and simulation values may be due to the amorphous packing each of the minerals had to undergo to form the shale model. Probably, the minerals were not tightly bound together during the packing as much as would be expected in reality. Also, actual shale formations have more minerals than presented in this work. This aspect of our work requires further research which will be investigated in subsequent works.

Table 4.4: Experimental and simulated matrix density

Sample	Formation	Matrix density (g/cm ³)	Porosity (%)
EF-1	Eagle Ford	2.65	2.01
EF-2	Eagle Ford	2.66	2.87
MC	Mancos	2.72	7.40
WF	Wolfcamp	2.45	2.45
Simulated shale model	N/A	2.30	19.8

4.2.5 Total Organic Carbon (TOC)

Figure 4.4 shows the peak graph of total organic carbon (TOC) and in Figure 4.5 it is shown that WF has the highest TOC among these shale samples while MC has the lowest TOC. Higher TOC presence presumably relates to higher hydrophobicity and higher adsorption capacity. As a result, WF, EF-2, and EF-1 possess high adsorption capacity than MC.

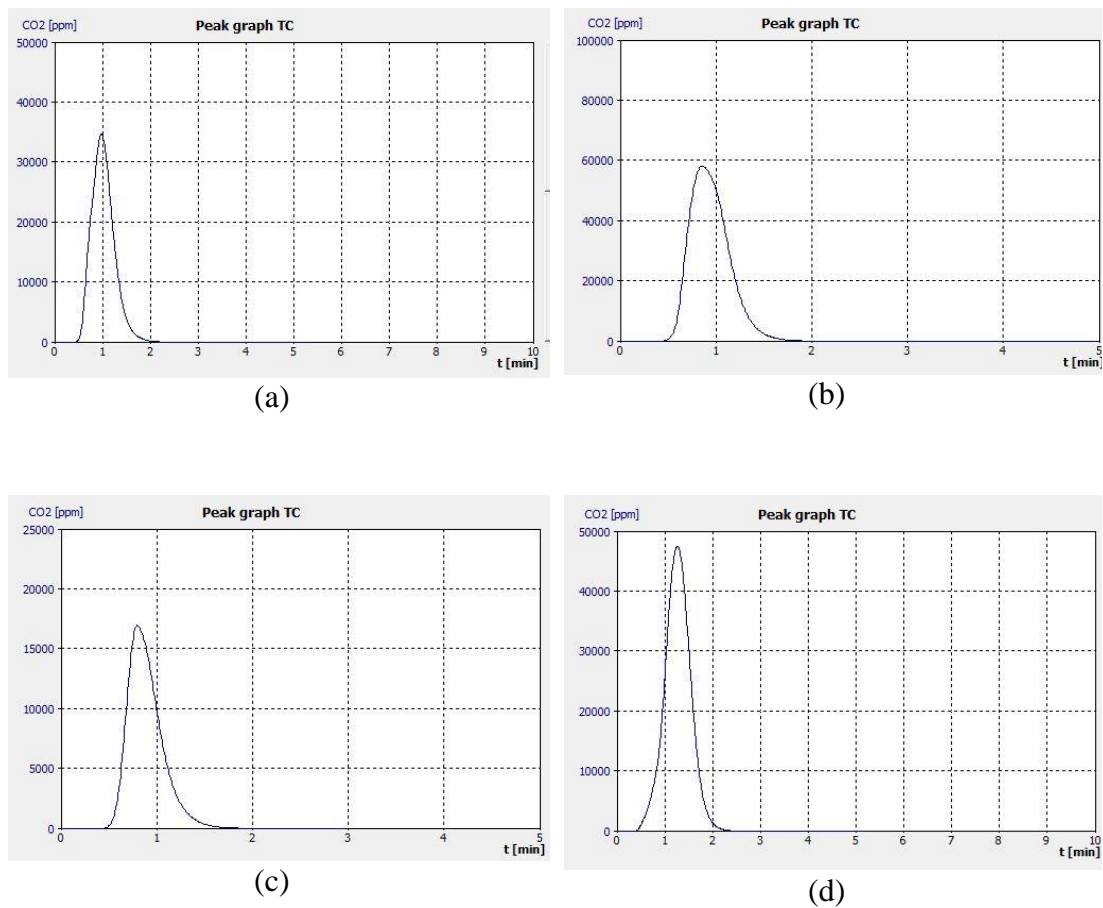


Figure 4.4: Peak graph of TOC of (a) EF-1, (b) EF-2, (c) MC, and (d) WF shale samples

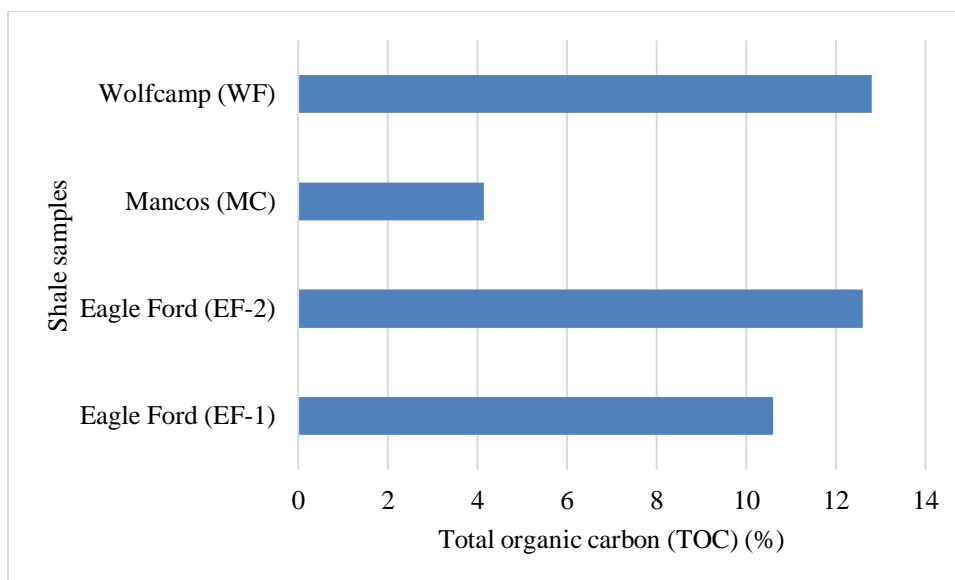


Figure 4.5: TOC percentage of shale samples

4.3 Molecular Simulation and Modelling

In this section the forcefield validation, solubility simulation, viscosity simulation, experimental validation of viscosity simulation, adsorption simulation, and experimental validation of adsorption simulation results have discussed in detail.

4.3.1 Forcefield Validation

In the methodology it has been discussed that the molecular shale model consists of organic matter (kerogen), clay minerals (montmorillonite and illite), and non-clay minerals (quartz). The characterization of EF-1, Ef-2, MC, and WF also shows the presence of clay and non-clay minerals. To assure the force field is correct, the geometric characteristics of each mineral and the resulting shale model's condensed-phase density are verified against NIST Chemistry Webbook [189] experimental results and the characterization results of the current study. The experimental bond angle and bond length of CO_2 are 180 and 1.162 whereas the simulated bond angle and bond length obtained by UNIVERSAL forcefield are 179.97 and 1.39. Similarly, the experimental bond angle and bond length of CH_4 are 109.5 and 1.087 whereas

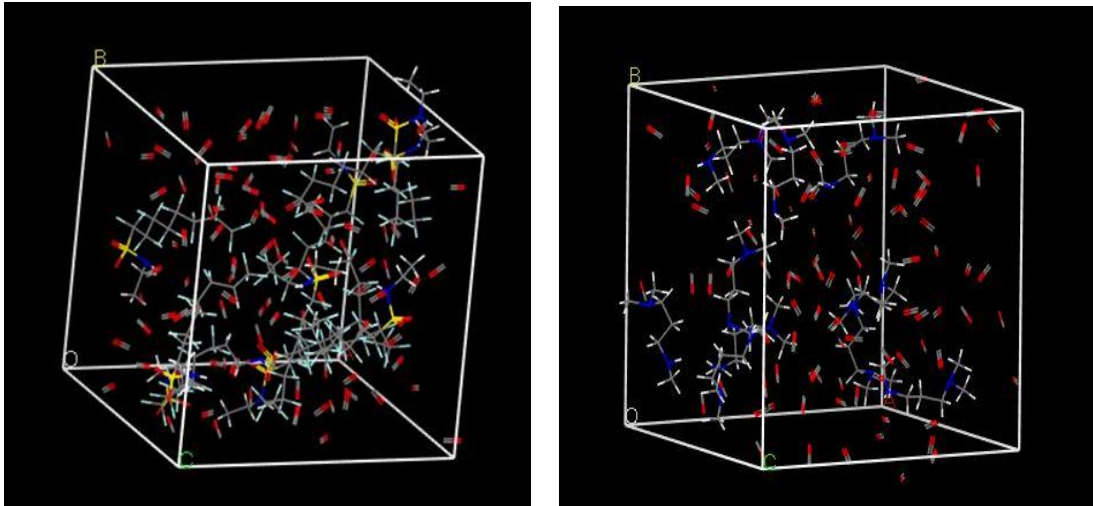
simulated bond angle and bond length are 109.47 and 1.14. Moreover, the simulated densities for individual components and the combined model using the UNIVERSAL force field [190] are quite close to testing data [185, 191] at ambient conditions. The simulated density of the postmature kerogen IID model is 1.185 g/cm³, which is fairly close to the experimental value of 1.181 g/cm³. The density of MMT ranges between 2 - 2.7 g/cm³ [191], the density of our model falls within this and it's 2.4g/cm³. Also, for illite, the simulated density was 2.7g/cm³ falling well within the experimental range of 2.6 - 2.9 g/cm³ [191]. For quartz, the experimental density ranges from 2.6 - 2.65 g/cm³ [191] whereas the simulated density is 2.61 g/cm³. A typical shale has a density ranging from 2.06 - 2.67 g/cm³ and the resulting model in this work was 2.3 g/cm³. The consistencies of these values with experimental data prove the validity of the model as well as the forcefield applied for the simulation.

4.3.2 Viscosity Enhancement of Carbon Dioxide using Viscoelastic Surfactant

In this sub-section the solubility of VES on Sc-CO₂ has been investigated. Moreover, the viscosity simulation result and the experimental validation of the viscosity simulation have also described in detail.

4.3.2.1 Solubility screening of VES in Sc-CO₂

In Figure 4.6 amorphous cells of Sc-CO₂ and N-ETFOSA mixture and Sc-CO₂ and N,N,N'-TM-1,3-PDA are presented. These figures inferred good solubility of Sc-CO₂ and VES. *Chi* is known as a material-specific polymer-solvent interaction parameter that is determined by the composition of the solvent as well as the solute. In terms of *Chi*, several thermodynamic properties of polymer solutions such as solubility/miscibility, balances of swelling, and other properties that rely on the blend composition are expressed.



(a)

(b)

Figure 4.6: An amorphous cell of the mixture of (a) Sc-CO₂ and N-ethyl perfluorooctyl sulfonamide, and (b) Sc-CO₂ and N,N,N'-Trimethyl-1,3-propanediamine.

Paul Flory [192] and Maurice Huggins [193] independently first popularized *Chi* as a unitless parameter for interaction in their polymer solutions' lattice model. *Chi* parameter had been used to investigate the polymer-polymer and polymer-solvent solubility [194, 195] in a molecular simulation study. A low *Chi* value provides a decrease in the free energy of the solution with the addition of solvent. Therefore, liquids with the smallest *Chi* are generally the strongest surfactant solvents [196]. N,N,N'-TM-1,3-PDA has a *Chi* parameter of 0.1199 on mixing with Sc-CO₂ while N-ETFOSA has a value of 4.9. These values indicate the N,N,N'-TM-1,3-PDA mixes more efficiently, and thus Sc-CO₂ is a better solvent for it than for N-ETFOSA.

4.3.2.2 Viscosity calculation

The proppant carrying capacity of Sc-CO₂ is relatively weaker than conventional fracturing fluid [197] and slickwater [198] due to its low viscosity. Increasing the viscosity of Sc-CO₂ will enhance its proppant carrying capacity and it will go one step further in the implementation of Sc-CO₂ as an alternative to the conventional fracturing fluid. Table 4.5 presents the simulation study of carbon dioxide and VES viscosity.

From the simulation, it is found that Sc-CO₂ has a final viscosity of 0.005 cP and adding the N-ETFOSA to Sc-CO₂ increases its final viscosity to 0.78 cP which is almost 156 times of actual viscosity. On the other hand, adding N,N,N'-TM-1,3-PDA to Sc-CO₂ increases the final viscosity to 0.179 cP which is 36 times greater than actual Sc-CO₂ viscosity. Fluorine has a high electron affinity and electronegativity, hence fluorocarbon with a carbon number greater than or equal four has higher CO₂-philicity as CO₂ also has a low dielectric constant [199]. Moreover, CO₂ and fluorocarbon surfactant tails have strong interactions [200]. As a result, N-ETFOSA thickens Sc-CO₂ better by possessing a high amount of fluorine between these two VES.

Table 4.5: The viscosity of different structures using Forcite Shear simulation.

Structure	Temperature (K)	Pressure (KPa)	Initial Viscosity (cP)	Final Viscosity (cP)	Average Viscosity (cP)
CO ₂	298	100	1.814 × 10 ⁻⁴	0.003	1.799 × 10 ⁻⁴
N-ETFOSA	298	100	0.156	0.289	0.218
N,N,N'-TM-1,3-PDA	298	100	0.211	1.528	0.545
Sc-CO ₂	305	7400	7.23 × 10 ⁻⁵	0.005	4.49 × 10 ⁻⁴
Sc- N-ETFOSA	305	7400	0.074	0.244	0.153
Sc- N,N,N'-TM-1,3-PDA	305	7400	1.25	3.406	0.01427
Sc-CO ₂ - N-ETFOSA mixture	305	7400	0.559	0.78	0.0915
Sc-CO ₂ -N,N,N'-TM-1,3-PDA mixture	305	7400	0.246	0.179	0.015

According to the Newton's law of viscosity fluid can be divided into two categories i.e., Newtonian, and non-Newtonian fluid. Shear rate is related to viscosity by the following equation.

$$\text{Shear stress} = \text{shear rate} * \text{viscosity}$$

In Newtonian fluid the viscosity is independent of the shear rate whereas in non-Newtonian fluid the viscosity is not constant and dependent on the shear rate. Moreover, when the viscosity of non-Newtonian fluid decreases with the increase of shear rate that behavior is known as shear thinning and when the viscosity of non-Newtonian fluid increases with the increase of shear rate is termed as shear thickening.

In the viscosity simulation the loading ratio of Sc-CO₂ and VES was 10:1. And the shear rate was kept constant at a steady rate of 0.1 ps⁻¹. However, at a temperature and pressure of 305 K and 7400 kPa a simulation study was carried out by increasing the shear rate from 0.1 ps⁻¹ to 1 ps⁻¹. Figure 4.7 shows that the viscosity of N-ETFOSA thickened Sc-CO₂ and N,N,N'-TM-1,3-PDA thickened Sc-CO₂ decrease along with the increase of shear rate. Therefore, this behavior can be characterized as shear thinning. Moreover, Sun et al. [201] investigated the rheological properties of CO₂ viscoelastic surfactant foam fracturing fluid and found it to be a shear thinning fluid.

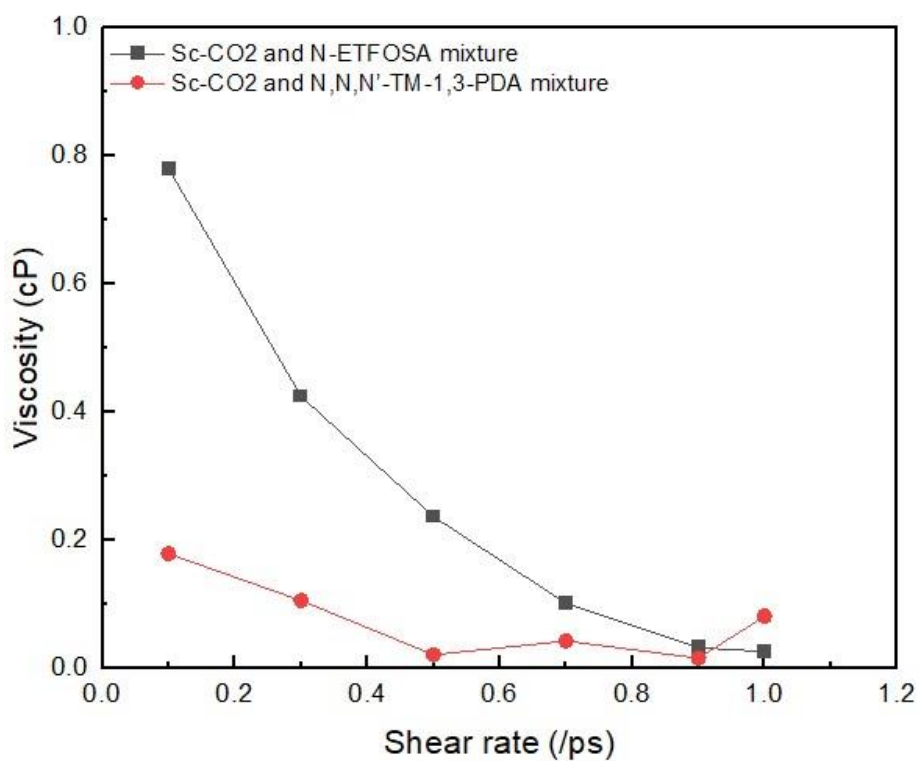


Figure 4.7: Viscosity as a function of shear rate at 305 K and 7400 kPa

4.3.2.3 Experimental validation of viscosity simulation

Table 4.6 presents the experimental and simulated viscosity results. Although the maximum deviation of the simulated viscosity result from the experimental result is 9.84% while the average deviation is 7.93%. Moreover, with the increasing temperature the deviation is also increasing (i.e., at temperature 380 K, 400 K, and 420 K the deviations are 7.72%, 7.83%, and 8.31% respectively). Furthermore, with increasing

temperature, the viscosity of fracturing fluid (i.e., water-based and Sc-CO₂) decreases [202, 203] whereas with increasing pressure the viscosity also increases [203]. The viscosity simulation results of this study also show a similar outcome. However, experimental and simulation results follow a similar trend as shown in Figure 4.8. This discrepancy between the experiment and the simulation may be caused by the differences between the real chemical interactions, thermal thinning of polymer, and the 3D molecular structure interactions of the simulation. Moreover, other properties such as molecular weight, shear rate need to be considered in a future study to mitigate this discrepancy.

Table 4.6: Comparison of experimental and simulated viscosity

Structure	Temperature (K)	Pressure (MPa)	Experimental Viscosity (cP) [178]	Simulated Viscosity (cP)		
				Initial Viscosity	Final Viscosity	Average Viscosity
Sc-CO ₂ - Poly(dimethylsiloxane) mixture	380	45	0.078	0.0418	0.0821	0.01074
Sc-CO ₂ - Poly(dimethylsiloxane) mixture	380	50	0.08	0.0586	0.0863	0.00524
Sc-CO ₂ - Poly(dimethylsiloxane) mixture	380	55	0.083	0.06401	0.0898	0.05765
Sc-CO ₂ - Poly(dimethylsiloxane) mixture	380	60	0.087	0.0712	0.0973	0.001214
Sc-CO ₂ - Poly(dimethylsiloxane) mixture	400	50	0.066	0.059	0.0719	0.02172
Sc-CO ₂ - Poly(dimethylsiloxane) mixture	400	55	0.073	0.065	0.079	0.00437
Sc-CO ₂ - Poly(dimethylsiloxane) mixture	400	60	0.079	0.069	0.084	0.00493
Sc-CO ₂ - Poly(dimethylsiloxane) mixture	420	50	0.061	0.042	0.067	0.01924
Sc-CO ₂ - Poly(dimethylsiloxane) mixture	420	55	0.064	0.049	0.07	0.00532
Sc-CO ₂ - Poly(dimethylsiloxane) mixture	420	60	0.07	0.054	0.074	0.00574

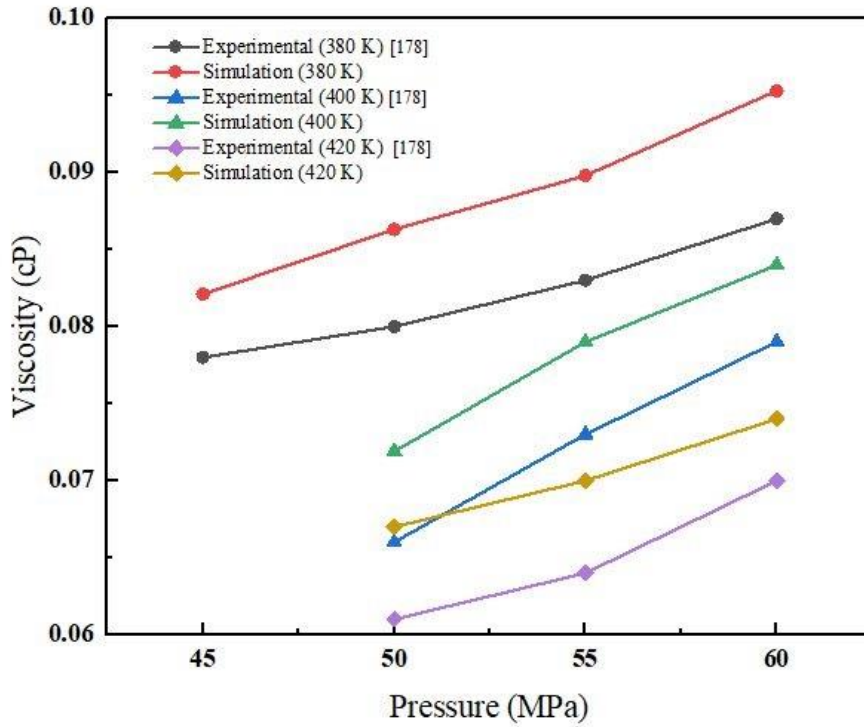


Figure 4.8: Viscosity variation with increasing pressure at 380, 400, and 420 K temperature

4.3.3 Adsorption Simulation

In this sub-section the detail result of adsorption simulation of thickened Sc-CO₂ and CH₄ on shale model and kerogen model has been discussed. Moreover, the experimental validation of the adsorption simulation has been provided. In addition, isosteric heat of thickened Sc-CO₂ and selectivity of thickened Sc-CO₂ over CH₄ on molecular shale have been described in detail.

4.3.3.1 Adsorption of thickened carbon dioxide

Adsorption simulation of Sc-CO₂, thickened Sc-CO₂, and CH₄ was carried out on molecular shale model and Figure 4.9 represents the adsorption isotherm of CO₂, thickened Sc-CO₂, and CH₄. These adsorption isotherms are for a temperature of 305 K and pressure ranging from 10 kPa to 7400 kPa. As seen in the figures, the adsorbed amount increases as pressure increases until a relatively higher pressure with

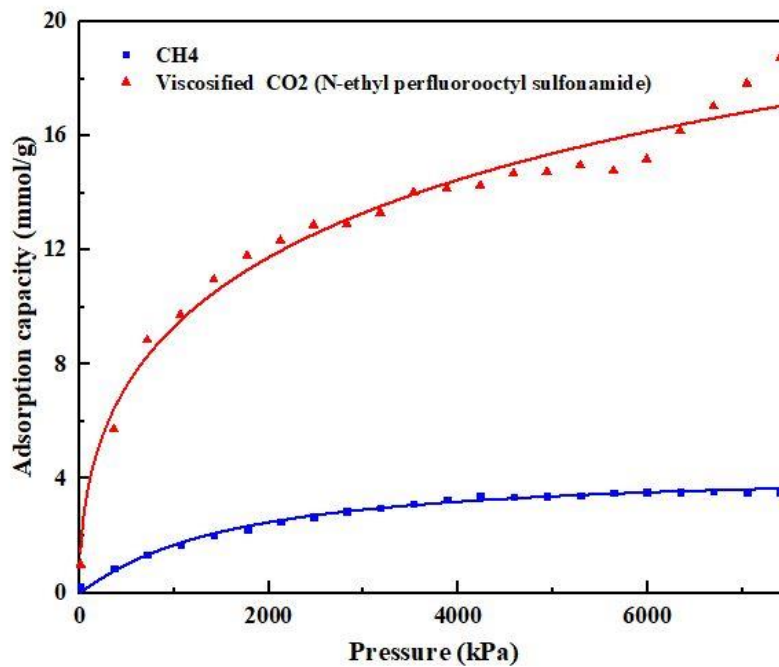
equilibrium is achieved. It does seem that methane achieves equilibrium faster than CO₂. Here in this study, it is found that the adsorption of CO₂ is almost similar to CH₄ at lower pressure. Chen et al. in 2020 proposed graphene – montmorillonite as a shale matrix and found that at a temperature of 323 K and pressure between 1-2 MPa (1000-2000 kPa) the adsorption capacity of CO₂ and CH₄ is almost similar [204]. From Figure 4.9 (c), it is found that as the pressure increases, the adsorption of CO₂ in the molecular shale model gets increased more than CH₄. Chen et al. also derived CO₂ adsorption capacity increases rapidly than CH₄ with increasing pressure [204].

According to Kawthar et al. in 2020 CH₄ and CO₂ had a maximum adsorption capacity of 2.8 and 4.2 mmol/g at a pressure and temperature of 17000 kPa and 318K [163]. Moreover, temperature changes affect adsorption. As the temperature increases, so does the momentum of the component's movement due to kinetic energy changes. Because of this, at higher temperatures, the adsorption rate is lower [181, 205, 206]. This reason satisfies the difference in adsorption rate in Figures 4.9 and 4.10 at the same pressure but at a different temperature such as 318 K and 305 K respectively. Thus, the adsorption result of this study is validated which allows accessing the accuracy of the used molecular shale model. From the isotherms in Figure 4.9, it can be observed that thickened Sc-CO₂ using both the VES have higher adsorption capacity than the result mentioned for CO₂ and thus higher affinity for shale formation. This further proves that thickened Sc-CO₂ can be used to displace CH₄, and shale exhibits preferential adsorption for thickened Sc-CO₂. The higher adsorption capacity of the thickened Sc-CO₂ implies that the addition of the VES that we have adopted in this study increases the affinity of Sc-CO₂ for shale and thus leaving fewer adsorption sites for methane. Consequently, the thickened Sc-CO₂ can increase methane desorption and ultimately production.

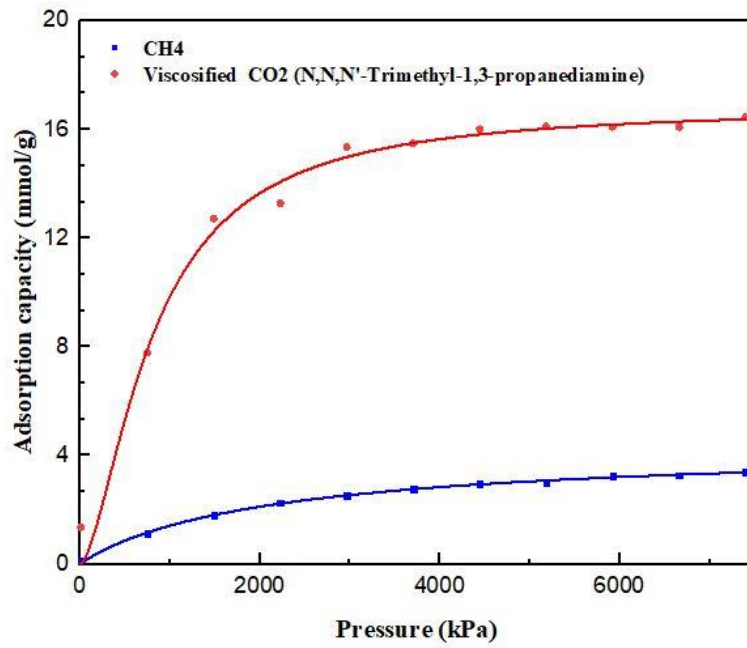
As discussed in sub-section 4.3.2.2, the final viscosity of Sc-CO₂ and N-ETFOSA mixture is 0.78 cP which is higher than the final viscosity of Sc-CO₂ and N,N,N'-TM-1,3-PDA mixture with the value of 0.179 cP. As the pressure increases the adsorption capacity of thickened Sc-CO₂ with N-ETFOSA was increased but for thickened Sc-CO₂ with N,N,N'-TM-1,3-PDA became almost linear. The presence of fluorine in N-ETFOSA provides better viscosity of Sc-CO₂ hence better adsorption in the molecular shale model. It is expected that the adsorption capacity correlates linearly with the

viscosity. According to adsorption isotherms, thickened Sc-CO₂ with higher viscosity has higher adsorption capacity, this could mean that the correlation between viscosity and adsorption capacity is as linear as expected. Although the mixture exhibits some adsorbate-adsorbent interactions with the adsorption surface, it is necessary to consider both the viscosity and its interaction with the adsorption site while selecting the optimal VES for use with Sc-CO₂.

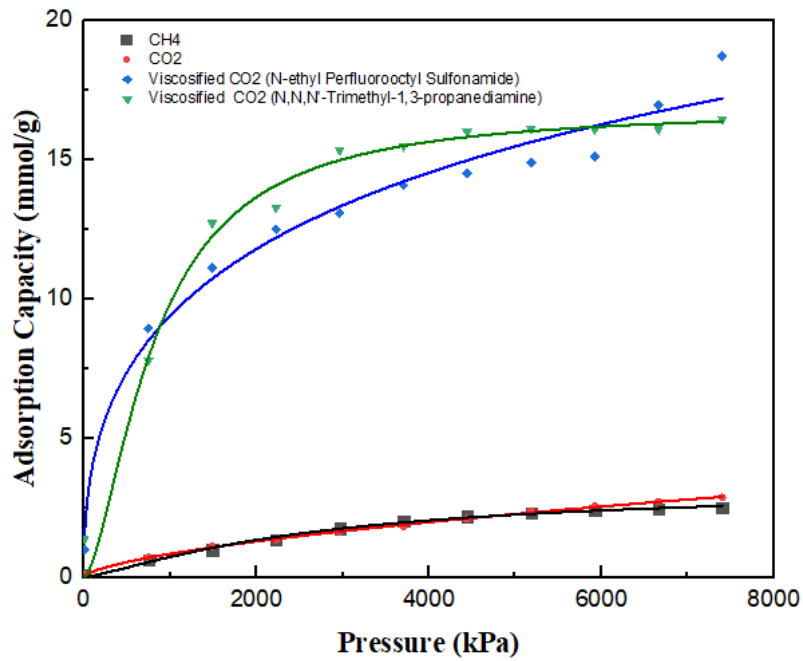
In Figure 4.10 the adsorption isotherm of CO₂ thickened Sc-CO₂, and CH₄ on the only type II-D kerogen has been presented. In comparison with the multi-component molecular shale model, thickened Sc-CO₂ with N,N,N'-TM-1,3-PDA shows half of its adsorption capacity in type II-D kerogen. Although thickened Sc-CO₂ with N-ETFOSA provides almost similar adsorption capacity in the molecular shale model which shows it has better interaction with the organic component of the shale. From Figure 4.8 (c) and 4.9 (c), it is found that CO₂ adsorption takes place more in the organic matter (i.e., kerogen) of the shale. The result of CO₂ and CH₄ adsorption in type II-D kerogen is in line with the result found by Huang et al. in 2018 [185] which also provides the validation of the simulation result of the current study.



(a)

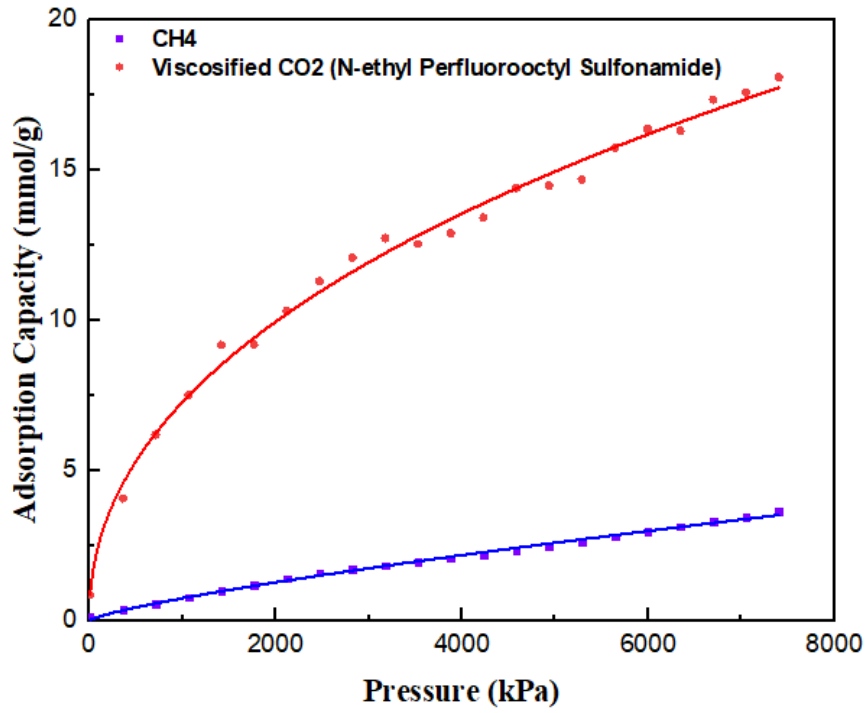


(b)

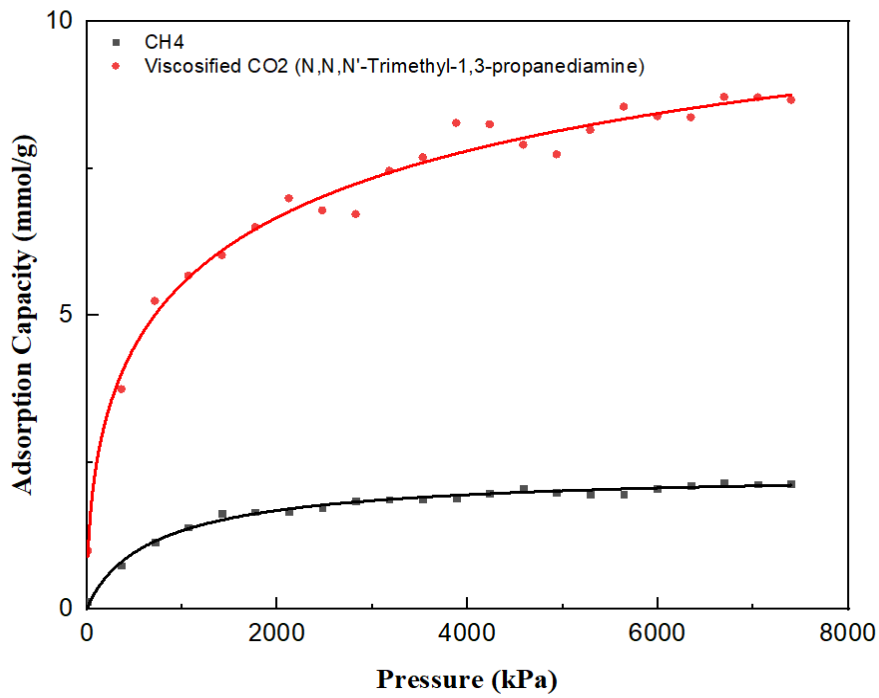


(c)

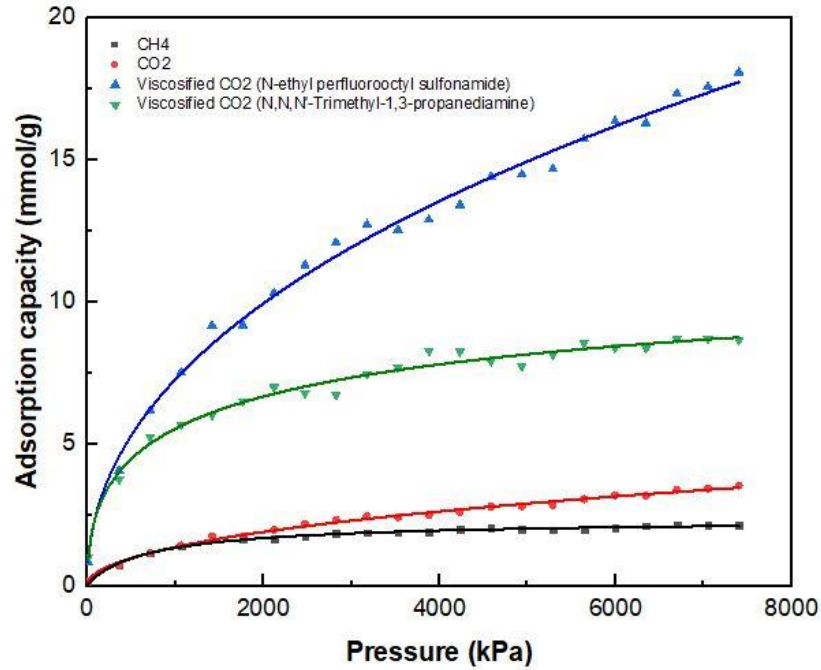
Figure 4.9: Adsorption isotherm of (a) thickened CO₂ using N-ETFOSA and CH₄, (b) thickened CO₂ using N,N,N'-TM-1,3-PDA, and CH₄, and (c) CO₂, thickened CO₂ using N-ETFOSA, thickened CO₂ using N,N,N'-TM-1,3-PDA, and CH₄ on molecular shale model (Langmuir fitting is represented by the line).



(a)



(b)



(c)

Figure 4.10: Adsorption isotherm of (a) thickened CO₂ using N-ETFOSA and CH₄, (b) thickened CO₂ using N,N,N'-TM-1,3-PDA, and CH₄, and (c) CO₂, thickened CO₂ using N-ETFOSA, thickened CO₂ using N,N,N'-TM-1,3-PDA, and CH₄ on type II-D kerogen model (Langmuir fitting is represented by the line).

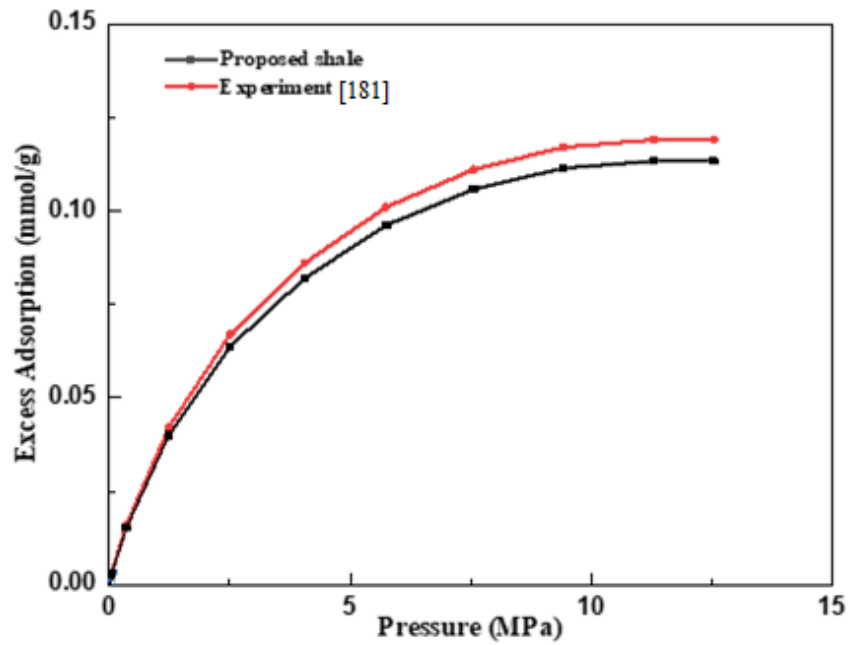
Additionally, the maximum adsorption capacity is also presented which is determined using the Langmuir model which was used to fit the adsorption isotherm. Table 4.7 shows the Langmuir fitting parameters of thickened Sc-CO₂ adsorption on the molecular shale model. Sc-CO₂ thickened with N-ETFOSA has higher n_{max} while methane consistently shows lower n_{max} . The results are as expected. The presence of VES increased the n_{max} of CO₂, thus, the addition of these thickeners helps to raise the effectiveness of using the CO₂ as a fracturing fluid. The n_{max} of methane reduces when it is adsorbed with thickened CO₂, this points to reduced adsorption on its part and thus increased ability of CO₂ to displace methane or preferentially occupy the adsorption sites.

Table 4.7: Langmuir fitting parameters for (a) CH₄ and Thickened CO₂ using N-ethyl perfluorooctyl sulfonamide, and (b) CH₄ and Thickened CO₂ using N,N,N'-Trimethyl-1,3-propanediamine adsorption on molecular shale model.

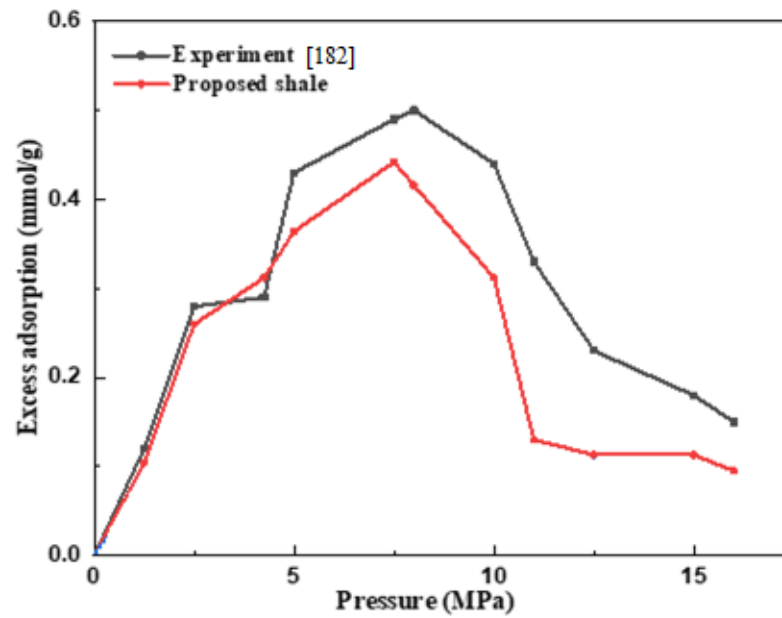
Molecular Shale Model					
		(a)		(b)	
		CH ₄	Thickened CO ₂ using N-ETFOSA	CH ₄	Thickened CO ₂ using N,N,N'-TM-1,3-PDA
LMAC	n^a_{max}	4.15	21.02	4.10	16.26
Langmuir constant	b	0.0002	0.01	0.0002	0.00006
R-square		0.992	0.970	0.996	0.984

4.3.3.2 Experimental validation of adsorption simulation

Figure 4.11 shows the comparison of excess adsorption capacity of CH₄ and CO₂ on shale samples and the molecular shale model. Quantitatively, the differences between the experimental values and the molecular shale model values of CH₄ and CO₂ adsorption are as low as 4.7% and 7% at some pressure points. This shows that the proposed model exhibits similar adsorption behavior and values as would be expected of an actual shale sample. This further proves the accuracy and rationality of the model and also the adsorption simulation. It also shows that the model can be adopted in shale adsorption studies as it mitigates the problem of excessive disparity between simulation and experimental adsorption data.



(a)



(b)

Figure 4.11: Comparison of the excess adsorption capacity of (a) CH₄, and (b) CO₂ on shale samples between simulation results and experimental results

4.3.4 Isotheric Heat of Thickened Carbon Dioxide

To understand the thermodynamic behavior of the fluids, the isotheric heat is reported as shown in Figure 4.12. The isotheric heat seems to increase as coverage increases for all the fluids although methane and CO₂ show very minimal increase. At increased coverage, enhanced heat associates with the effects of adsorbate-adsorbate interactions. The limit isotheric heat is presented in Table 4.8, which represents the isotheric heat at zero coverage which demonstrates the adsorption enthalpy between adsorbate and adsorbent without the effects of adsorbate-adsorbate interactions. These values increase in the order of thickened CO₂ using N-ETFOSA > thickened CO₂ using N,N,N'-TM-1,3-PDA > CH₄ > CO₂. This order aligns with adsorption capacity. Average isotheric heat was also computed as shown in Table 4.8. The trend in the values corresponds with the trend in limit isotheric heat with the value of thickened CO₂ using N-ETFOSA being the highest and CO₂ being the lowest. Indicating again, the higher adsorption affinity and also the positive effect of VES on the adsorption of CO₂ and desorption of CH₄.

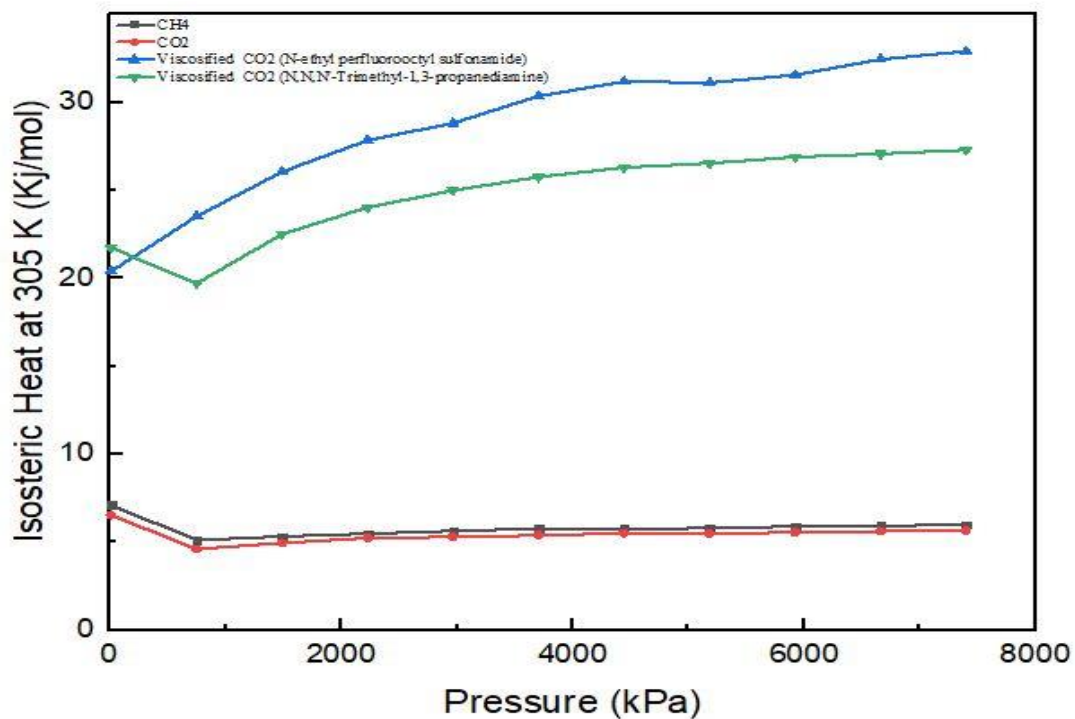


Figure 4.12: Isotheric heat on molecular shale model

Table 4.8: Average and limit isosteric heat of CH₄, CO₂, and thickened CO₂ on molecular shale model

	Molecular Shale Model	
	Average Isosteric Heat	Limit Isosteric Heat
CH ₄	5.808	7.121
CO ₂	5.449	6.543
Thickened CO ₂ using N-ETFOSA	28.735	20.389
Thickened CO ₂ using N,N,N'-TM-1,3-PDA	24.798	21.737

4.3.5 Selectivity of Thickened Carbon Dioxide over Methane

The selectivity of thickened carbon dioxide over methane was calculated using Equation 4.1 [179]. According to Figure 4.13, the selectivity ranges from 1 to 9.5 in this study. At lower pressure points (< 7000 kPa), the selectivity of CO₂ thickened with N,N,N'-TM-1,3-PDA was higher than others. Above 7000 kPa pressure thickened CO₂ using N-ETFOSA shows better selectivity than others which is an indication that at high-pressure high-temperature conditions this will thicken the CO₂ better. This is consistent with other results such as viscosity and isosteric heat. Also, the selectivity generally increases with pressure. The energetic heterogeneity of different surfaces determines selectivity. A higher selectivity suggests preferential adsorption of thickened carbon dioxide and it occupies more energetic sites and displaces methane. Results of selectivity are highly correlated with the isotherms shown in Figure 4.13. The isotherms show that the quantity of thickened CO₂ adsorbed on the surfaces is higher than CH₄ and therefore there is the selectivity of more than one for thickened CO₂ over CH₄.

$$SV\left(\frac{CO_2}{CH_4}\right) = \frac{X_{VCO_2}/X_{CH_4}}{Y_{VCO_2}/Y_{CH_4}} \quad (4.1)$$

Where $SV(CO_2/CH_4)$ is presented as the selectivity of thickened carbon dioxide over methane, the mole fraction of i in the bulk phase, and the adsorption phase is represented by Y_i and X_i , respectively.

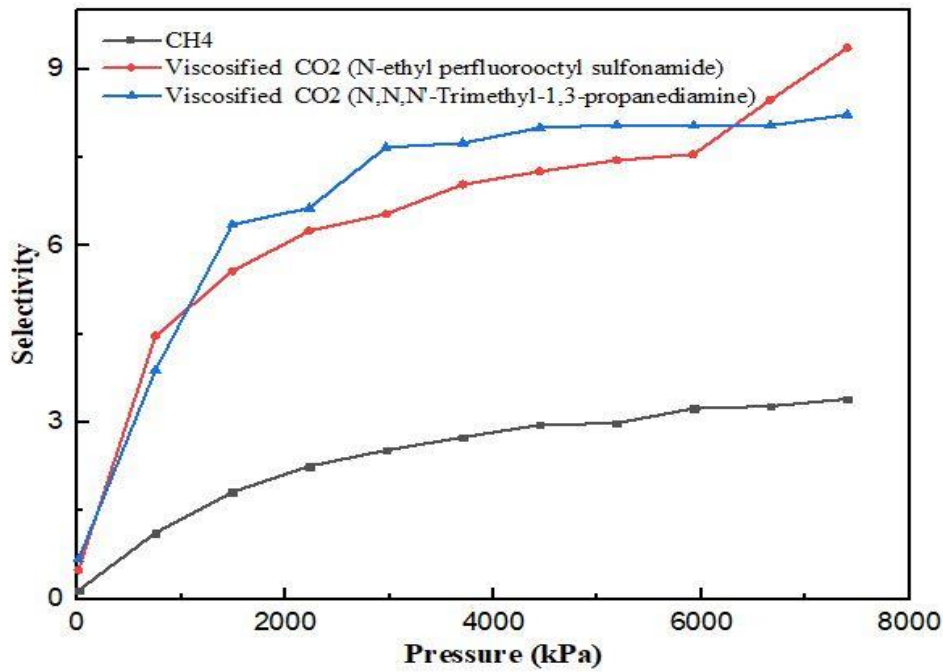


Figure 4.13: Thickened CO₂/CH₄ selectivity on molecular shale model

4.4 Summary

In this chapter, the characterization results of shale samples and simulation results of Sc-CO₂ thickening and adsorption of thickened Sc-CO₂ over CH₄ on the molecular shale model have been disclosed. The characterizations of actual shale samples (EF-1, EF-2, MC, and WF) provides enough evidence to validate the molecular shale model properties. Thickening of Sc-CO₂ using N-ethyl perfluorooctyl sulfonamide and N,N,N'-Trimethyl-1,3-propanediamine increases the viscosity of Sc-CO₂ by 156 and 36 times, respectively than the actual viscosity of Sc-CO₂. The adsorption study shows that thickened Sc-CO₂ has a higher adsorption capacity than CH₄ which increases CH₄ desorption profoundly.

CHAPTER 5

CONCLUSIONS AND RECOMMENDATIONS

5.1 Conclusions

Waterless fracturing technologies are gaining attention due to the dire need to protect water resources and ever-increasing environmental concerns. However, to derive the utmost advantage from these technologies and to avoid risks, in-depth understanding is important. In general, waterless fracturing technologies have a high initial cost but over a longer period of a run, these technologies deliver outstanding economic performances. The most promising among waterless fracturing fluids is SC-CO₂. Nevertheless, considering the Sc-CO₂ fracturing operation, poor proppant carrying capacity, high frictional resistance, large displacement, filtration loss, sand plugging, and lack of proper adsorption isotherm of Sc-CO₂ are the potential limitations. Therefore, to exercise Sc-CO₂ fracturing technology in the field, one must overcome these problems.

In this study, a heterogeneous molecular shale model consisting of kerogen type II D, montmorillonite, illite, and quartz has been developed and later validated by characterizing shale samples from Eagle ford, Mancos, and Wolfcamp formations. According to the EDX results, it can be seen that the carbon content of shale samples is not so high except EF-1 and there is also no trace of hydrogen which eliminates the possibility of the presence of organic matter. On the other hand, the molecular shale model has almost a similar carbon content as EF-1, but it also has the prominent presence of hydrogen. Moreover, from pore size distribution it is found that most of the pores are fall in the mesopore category. The surface area and volume of the proposed shale model were found to be 507.7438 m²/g and 0.4348 cm³/g, respectively, which are in the range of experimental values. Properties such as the density of the proposed shale model were predicted to be 2.3 g/cm³ by the simulation. Experimental results show that the matrix density of shale samples ranges between 2.45 g/cm³ to 2.72 g/cm³ which is

very much in line with the simulation result. A slight variation in porosity between samples and the molecular model was observed due to the amorphous packing of each mineral. Thus, it can be outlined that the first objective of this study has been achieved.

Moreover, to eradicate the poor proppant carrying capacity of Sc-CO₂, a simulation study has been carried out to thicken it using VES. N-ETFOSA and N,N,N'-TM-1,3-PDA are used as thickening agents of Sc-CO₂ at a temperature of 298 K – 305 K and pressure varying from 10 kPa – 7400 kPa. Although the molecular simulation studies show that N,N,N'-TM-1,3-PDA provides better solubility in CO₂ than N-ETFOSA, the first and later one increases the viscosity of Sc-CO₂ by 36 and 156 times, respectively than the actual viscosity of Sc-CO₂. Moreover, viscosity simulation has been validated by simulating the experimental data from the work of Xiong et al. and it is found that the maximum deviation of simulation results from experimental work is 9.84% while the average deviation is 7.93%. Therefore, it can be inferred that the thickening of Sc-CO₂ using VES has been achieved.

Furthermore, a simulation study of the preferential adsorption of thickened Sc-CO₂ over CH₄ on a molecular shale model has been performed to investigate CH₄ desorption and potential CO₂ sequestration. The results from adsorption isotherms and isosteric heats, show that N-ETFOSA thickened Sc-CO₂ perform better than N,N,N'-TM-1,3-PDA thickened Sc-CO₂. This is due to the presence of a high amount of fluorine in N-ETFOSA which has made it more compatible with Sc-CO₂. Comparing the adsorption trends, it is inferred that Sc-CO₂ thickened with N-ETFOSA has a higher adsorption capacity when the pressure increases. Accordingly, at higher pressure N-ETFOSA thickened Sc-CO₂ shows better selectivity over methane and N,N,N'-TM-1,3-PDA thickened Sc-CO₂ on the molecular shale model. In addition, adsorption simulation has also been validated by simulating the experimental data from the work of Rexer et al. and Liu et al. The differences between the experimental values and the molecular shale model values of CH₄ and CO₂ adsorption are as low as 4.7% and 7% at some pressure points. Thus, the preferential adsorption of thickened Sc-CO₂ over CH₄ on the molecular shale model has been analyzed. Moreover, taking all the determinant factors into consideration it can be inferred from the results that N-ETFOSA is a better choice

of VES for Sc-CO₂ thickening than N,N,N'-TM-1,3-PDA and thus enhancing its proppant carrying capacity.

5.2 Recommendations

In respect to the result analysis and extensive literature review, some recommendations are listed to make this study more viable in terms of field applications.

- There are ample scopes to make the molecular shale model better. The presence of other minerals except which have been used in the molecular shale model needs further investigation.
- In presence of formation water, binary gas, or higher hydrocarbon preferential adsorption of Sc-CO₂ over CH₄ requires further investigation both at the experimental and molecular levels.
- Moisture content and salinity are also some important aspects that need due consideration in the future study and betterment of the molecular shale model.
- This study has been carried out at a temperature of 305 K and pressure ranging from 10 kPa to 7400 kPa. Higher temperature and pressure need to be attained to simulate the harsh reservoir conditions in a better way.
- The environmental impact of using the VES needs to be checked. As the world is turning towards green and sustainable technology, environmental concerns need to be kept in the selection criteria of choosing green VES.

LIST OF PUBLICATIONS

ISI-indexed Journal Papers:

1. **Muhammed Rashik Mojid**, Berihun Mamo Negash, Hesham Abdulelah, Shiferaw Regassa Jufar, Kawthar Adewumi Babatunde, “A state – of – art review on waterless gas shale fracturing technologies”, **Journal of Petroleum Science and Engineering**, (JCR Q1, IF-4.346), Elsevier, Volume-196, Pages-108048, January 2021, Publication date: 19/10/2020

DOI: <https://doi.org/10.1016/j.petrol.2020.108048>

2. Kawthar Adewumi Babatunde, Berihun Mamo Negash, **Muhammed Rashik Mojid**, Tigwaba Y. Ahmed, Shiferaw Regassa Jufar, “Molecular simulation study of CO₂/CH₄ adsorption on realistic heterogeneous shale surfaces”, **Applied Surface Science**, (JCR Q1, IF-6.707), Elsevier, Volume-543, Pages-148789, March 2021, Publication date: 21/12/2020

DOI: <https://doi.org/10.1016/j.apsusc.2020.148789>

3. **Muhammed Rashik Mojid**, Berihun Mamo Negash, Kawthar Adewumi Babatunde, Tigwaba Y. Ahmed, Shiferaw Regassa Jufar, “Effects of Viscoelastic Surfactant on Supercritical Carbon Dioxide Thickening for Gas Shale Fracturing”, **Energy & Fuels**, (SCOPUS Q1, JCR Q2, IF-3.605), American Chemical Society, Volume-35, Issue-19, Pages-(15842-15855), Publication date: 17/09/2021

DOI: <https://doi.org/10.1021/acs.energyfuels.1c01215>

Conference Paper:

1. **Muhammed Rashik Mojid**, Berihun Mamo Negash, Kawthar Adewumi Babatunde, Shiferaw Regassa Jufar, “Evaluation of N-Ethyl Perfluorooctyl Sulfonamide as a thickener of supercritical carbon dioxide” **International Conference on Earth Resources (ICER) ETSCON 2021**, (In Press).

REFERENCES

- [1] S. K. Sunjay, Nikhil Jain, "Shale Gas: An Unconventional Gas Reservoir " 2014.
- [2] J. P. Vermeylen, *Geomechanical studies of the Barnett shale, Texas, USA*. Stanford University, 2011.
- [3] U. Eia, "Review of emerging resources: US Shale gas and shale oil plays," *Energy Information Administration, US Department of Energy*, 2011.
- [4] U. USEIA, "Energy Information Administration. 2013." "Technically Recoverable Shale Oil and Shale Gas Resources: An Assessment of 137 Shale Formations in 41 Countries Outside the United States." Washington DC: US Department of Energy," ed: US Department of Energy. Washington DC, 2013.
- [5] Y. Li, D. DiCarlo, X. Li, J. Zang, and Z. Li, "An experimental study on application of nanoparticles in unconventional gas reservoir CO₂ fracturing," *Journal of Petroleum Science and Engineering*, vol. 133, pp. 238-244, 2015.
- [6] J. Zhao, L. Ren, C. Shen, and Y. Li, "Latest research progresses in network fracturing theories and technologies for shale gas reservoirs," *Natural Gas Industry B*, vol. 5, no. 5, pp. 533-546, 2018.
- [7] Energy Information Administration of the United States of America. "Frequently Asked Questions (FAQs) - U.S. Energy Information Administration (EIA)." <https://www.eia.gov/tools/faqs/faq.php?id=907&t=8> (accessed 27 November, 2021).
- [8] R. D. Vidic, S. L. Brantley, J. M. Vandenbossche, D. Yoxtheimer, and J. D. Abad, "Impact of shale gas development on regional water quality," *Science*, vol. 340, no. 6134, p. 1235009, 2013.
- [9] J. Wang, M. Liu, Y. Bentley, L. Feng, and C. Zhang, "Water use for shale gas extraction in the Sichuan Basin, China," *Journal of environmental management*, vol. 226, pp. 13-21, 2018.
- [10] S. Ahmed, A. S. Hanamertani, and M. R. Hashmet, "CO₂ Foam as an Improved Fracturing Fluid System for Unconventional Reservoir," in *Exploitation of Unconventional Oil and Gas Resources-Hydraulic Fracturing and Other Recovery and Assessment Techniques*: IntechOpen, 2019.
- [11] K. Osaki, "US Energy Information Administration (EIA): 2019 Edition US Annual Energy Outlook report (AEO2019)," *Haikan Gijutsu*, vol. 61, no. 8, pp. 32-43, 2019.
- [12] J. D. Arthur, B. K. Bohm, B. J. Coughlin, M. A. Layne, and D. Cornue, "Evaluating the environmental implications of hydraulic fracturing in shale gas reservoirs," in *SPE Americas E&P environmental and safety conference*, 2009: OnePetro.
- [13] T. Guo, S. Zhang, Z. Qu, T. Zhou, Y. Xiao, and J. Gao, "Experimental study of hydraulic fracturing for shale by stimulated reservoir volume," *Fuel*, vol. 128, pp. 373-380, 2014.
- [14] R. W. Howarth, R. Santoro, and A. Ingraffea, "Methane and the greenhouse-gas footprint of natural gas from shale formations," *Climatic change*, vol. 106, no. 4, p. 679, 2011.
- [15] A. Rogala, J. Krzysiek, M. Bernaciak, and J. Hupka, "Non-aqueous fracturing technologies for shale gas recovery," *Physicochemical Problems of Mineral Processing*, vol. 49, 2013.

- [16] T. Jacobs, "Energized fractures: shale revolution revisits the energized fracture," *Journal of Petroleum Technology*, vol. 66, no. 06, pp. 48-56, 2014.
- [17] L. He, W. Feng, J. ZHANG, M. Siwei, and D. Yongwei, "Fracturing with carbon dioxide: Application status and development trend," *Petroleum exploration and development*, vol. 41, no. 4, pp. 513-519, 2014.
- [18] G. Moridis, "Literature review and analysis of waterless fracturing methods," Lawrence Berkeley National Lab.(LBNL), Berkeley, CA (United States), 2018.
- [19] Z. Huang, C. Shi, J. Xu, S. Kilic, R. M. Enick, and E. J. Beckman, "Enhancement of the viscosity of carbon dioxide using styrene/fluoroacrylate copolymers," *Macromolecules*, vol. 33, no. 15, pp. 5437-5442, 2000.
- [20] A. Omeiza and A. J. A. J. E. A. S. Samsuri, "Viscoelastic surfactants application in hydraulic fracturing, it's set back and mitigation—an overview," vol. 9, no. 1, pp. 25-29, 2006.
- [21] S. Li and D. Zhang, "How effective is carbon dioxide as an alternative fracturing fluid?," *SPE Journal*, 2018.
- [22] J. McClain *et al.*, "Characterization of polymers and amphiphiles in supercritical CO₂ using small angle neutron scattering and viscometry," in *ABSTRACTS OF PAPERS OF THE AMERICAN CHEMICAL SOCIETY*, 1996, vol. 211: AMER CHEMICAL SOC 1155 16TH ST, NW, WASHINGTON, DC 20036, pp. 145-PMSE.
- [23] R. D. Gdanski, D. D. Fulton, and C. Shen, "Fracture face skin evolution during cleanup," in *SPE Annual Technical Conference and Exhibition*, 2006: Society of Petroleum Engineers.
- [24] R. Barati, R. D. Hutchins, T. Friedel, J. A. Ayoub, M.-N. Dessinges, and K. W. England, "Fracture impact of yield stress and fracture-face damage on production with a three-phase 2D model," *SPE production & operations*, vol. 24, no. 02, pp. 336-345, 2009.
- [25] R. T. Whalen, "Viscoelastic surfactant fracturing fluids and a method for fracturing subterranean formations," ed: Google Patents, 2000.
- [26] Y. Chen, T. L. Pope, and J. C. Lee, "Novel CO₂-emulsified viscoelastic surfactant fracturing fluid system," in *SPE European Formation Damage Conference*, 2005: Society of Petroleum Engineers.
- [27] X. Tang, N. Ripepi, N. P. Stadie, L. Yu, and M. R. Hall, "A dual-site Langmuir equation for accurate estimation of high pressure deep shale gas resources," *Fuel*, vol. 185, pp. 10-17, 2016/12/01/ 2016, doi: <https://doi.org/10.1016/j.fuel.2016.07.088>.
- [28] J. S. Cong Chen, Yi Zhanga, Jianshu Mu, Weizhong Li, Yongchen Song, "Adsorption characteristics of CH₄ and CO₂ in organic-inorganic slit pores," *Fuel*, 2020, doi: 10.1016/j.fuel.2019.116969.
- [29] L. Gandossi and U. Von Estorff, "An overview of hydraulic fracturing and other formation stimulation technologies for shale gas production," *Eur. Commisison Jt. Res. Cent. Tech. Reports*, vol. 26347, 2013.
- [30] W. Gogarty and G. Haws, "LPG micellar solutions as fracturing fluids," *US Patent, US3818993*, pp. 6-25, 1974.
- [31] R. L. Gay, R. J. Schlott, and J. E. Burroughs, "Gelling agents for hydrocarbon compounds," ed: Google Patents, 1978.
- [32] D. A. Huddleston, "Hydrocarbon geller and method for making the same," ed: Google Patents, 1989.

- [33] G. G. Geib, "Hydrocarbon gels useful in formation fracturing," ed: Google Patents, 2000.
- [34] D. B. Acker and F. Malekahmadi, "Delayed release breakers in gelled hydrocarbons," ed: Google Patents, 2001.
- [35] J. Dawson, S. Kesavan, and H. Van Le, "Breaker system for fracturing fluids used in fracturing oil bearing formations," ed: Google Patents, 2004.
- [36] D. N. Loree, "Liquified petroleum gas fracturing system," ed: Google Patents, 2013.
- [37] D. P. Leblanc, T. Martel, D. G. Graves, E. Tudor, and R. Lestz, "Application of propane (LPG) based hydraulic fracturing in the McCully Gas Field, New Brunswick, Canada," in *North American Unconventional Gas Conference and Exhibition*, 2011: Society of Petroleum Engineers.
- [38] L. W. Gatlin, G. E. Walden, E. McMillan, and R. A. Gatlin, "Low temperature hydrocarbon gel," ed: Google Patents, 2013.
- [39] T. P. Wilson and M. J. Wanner, "Delayed hydrocarbon gel crosslinkers and methods for making and using same," ed: Google Patents, 2012.
- [40] J. Mao *et al.*, "Application and optimization: Non-aqueous fracturing fluid from phosphate ester synthesized with single alcohol," *Journal of Petroleum Science and Engineering*, vol. 147, pp. 356-360, 2016.
- [41] H. B. Mahmud, M. Ermila, Z. Bennour, and W. M. Mahmud, "A Review of Fracturing Technologies Utilized in Shale Gas Resources," in *Shale Gas Production-Lessons Learned*: IntechOpen, 2020.
- [42] L. Ren, R. Lin, and J. Zhao, "Stimulated reservoir volume estimation and analysis of hydraulic fracturing in shale gas reservoir," *Arabian Journal for Science and Engineering*, vol. 43, no. 11, pp. 6429-6444, 2018.
- [43] R. Zhang, B. Hou, Y. Zeng, J. Zhou, and Q. Li, "Investigation on Hydraulic Fracture Initiation and Propagation with LPG Fracturing in Shale Formation based on True Tri-Axial Laboratory Experiments," in *IADC/SPE Asia Pacific Drilling Technology Conference and Exhibition*, 2018: Society of Petroleum Engineers.
- [44] T. M. Soni, "LPG-based fracturing: an alternate fracturing technique in shale reservoirs," in *IADC/SPE Asia Pacific Drilling Technology Conference*, 2014: Society of Petroleum Engineers.
- [45] Z. Zhang, J. Mao, X. Yang, J. Zhao, and G. S. Smith, "Advances in waterless fracturing technologies for unconventional reservoirs," *Energy Sources, Part A: Recovery, Utilization, and Environmental Effects*, vol. 41, no. 2, pp. 237-251, 2019.
- [46] D. S. Gupta and H. D. Brannon, "Method of fracturing with liquefied natural gas," ed: Google Patents, 2014.
- [47] L. W. Gatlin, G. E. Walden, and E. McMillan, "Crosslinking composition for hydrocarbon gels," ed: Google Patents, 2015.
- [48] M. Prodanovic and K. P. Johnston, "Development of nanoparticle-stabilized foams to improve performance of water-less hydraulic fracturing," National Energy Technology Lab.(NETL), Pittsburgh, PA, and Morgantown, WV ..., 2017.
- [49] J. Gaydos and P. Harris, "Foam fracturing: theories, procedures and results," in *SPE Unconventional Gas Recovery Symposium*, 1980: Society of Petroleum Engineers.

- [50] S. R. Grundmann and D. L. Lord, "Foam stimulation," *Journal of Petroleum Technology*, vol. 35, no. 03, pp. 597-602, 1983.
- [51] P. C. Harris, D. E. Klebenow, and P. D. Kundert, "Constant-Internal-phase design improves stimulation results," *SPE production engineering*, vol. 6, no. 01, pp. 15-19, 1991.
- [52] E. Watkins, C. Wendorff, and B. Ainley, "A new crosslinked foamed fracturing fluid," in *SPE Annual Technical Conference and Exhibition*, 1983: Society of Petroleum Engineers.
- [53] M. Craighead, M. Hossaini, and E. Freeman, "Foam fracturing utilizing delayed crosslinked gels," in *SPE Annual Technical Conference and Exhibition*, 1985: Society of Petroleum Engineers.
- [54] S. D. Khade and S. N. Shah, "New rheological correlations for guar foam fluids," *SPE Production & Facilities*, vol. 19, no. 02, pp. 77-85, 2004.
- [55] Q. Sun and S. Hutzler, "Lattice gas simulations of two-dimensional liquid foams," *Rheologica acta*, vol. 43, no. 5, pp. 567-574, 2004.
- [56] W. Wanniarachchi, P. Ranjith, and M. Perera, "Shale gas fracturing using foam-based fracturing fluid: a review," *Environmental Earth Sciences*, vol. 76, no. 2, p. 91, 2017.
- [57] J. Liu, G. Liu, and L. Ma, "Material data sheet of Chemistry and Chemical Engineering, M," ed: Beijing, Chemical Industry Press, 2002.
- [58] Z. Li, H. Xu, and C. Zhang, "Liquid nitrogen gasification fracturing technology for shale gas development," *Journal of Petroleum Science and Engineering*, vol. 138, pp. 253-256, 2016.
- [59] C. Cai, G. Li, Z. Huang, and F. Gao, "Thermal cracking effect of liquid nitrogen on shale and its application analysis in hydraulic fracturing," *Zhongguo Shiyou Daxue Xuebao (Ziran Kexue Ban)/Journal of China University of Petroleum (Edition of Natural Science)*, Article vol. 40, no. 1, pp. 79-85, 2016, doi: 10.3969/j.issn.1673-5005.2016.01.011.
- [60] R. T. Jacobsen, R. B. Stewart, and M. Jahangiri, "Thermodynamic properties of nitrogen from the freezing line to 2000 K at pressures to 1000 MPa," *Journal of Physical and Chemical Reference Data*, vol. 15, no. 2, pp. 735-909, 1986.
- [61] W. Lin, "Mechanical properties of Mesaverde sandstone and shale at high pressures.[Colorado and Wyoming]," Lawrence Livermore National Lab., CA (USA), 1983.
- [62] D. Tran, A. Settari, and L. Nghiem, "Initiation and propagation of secondary cracks in thermo-poroelastic media," in *46th US Rock Mechanics/Geomechanics Symposium*, 2012: American Rock Mechanics Association.
- [63] B. McDaniel, S. R. Grundmann, W. D. Kendrick, D. R. Wilson, and S. W. Jordan, "Field applications of cryogenic nitrogen as a hydraulic fracturing fluid," in *SPE annual technical conference and exhibition*, 1997: Society of Petroleum Engineers.
- [64] W. G. Halbert, "Method of increasing the permeability of a subterranean hydrocarbon bearing formation," ed: Google Patents, 1971.
- [65] S. R. Grundmann, G. D. Rodvelt, G. A. Dials, and R. E. Allen, "Cryogenic nitrogen as a hydraulic fracturing fluid in the devonian shale," in *SPE Eastern Regional Meeting*, 1998: Society of Petroleum Engineers.

- [66] D. Gupta and D. Bobier, "The history and success of liquid CO₂ and CO₂/N₂ fracturing system," *SPE*, vol. 40016, pp. 15-18, 1998.
- [67] H. Crawford, G. Neill, B. Bucy, and P. Crawford, "Carbon dioxide-a multipurpose additive for effective well stimulation," *Journal of Petroleum Technology*, vol. 15, no. 03, pp. 237-242, 1963.
- [68] M. L. Sinal and G. Lancaster, "Liquid CO fracturing: advantages and limitations," *Journal of Canadian Petroleum Technology*, vol. 26, no. 05, 1987.
- [69] R. S. Bullen and A. T. Lillies, "Carbon dioxide fracturing process and apparatus," ed: Google Patents, 1983.
- [70] S. B. Hawthorne, C. D. Gorecki, J. A. Sorensen, E. N. Steadman, J. A. Harju, and S. Melzer, "Hydrocarbon mobilization mechanisms from upper, middle, and lower Bakken reservoir rocks exposed to CO₂," in *SPE Unconventional Resources Conference Canada*, 2013: Society of Petroleum Engineers.
- [71] A. Settari, R. Bachman, and D. Morrison, "Numerical simulation of hydraulic fracturing treatments with low-viscosity fluids," *Journal of Canadian Petroleum Technology*, vol. 26, no. 05, 1987.
- [72] S. W. Luk and J. L. Grisdale, "High proppant concentration/high CO₂ ratio fracturing system," ed: Google Patents, 1996.
- [73] R. Mazza, "Liquid-free CO₂/sand stimulations: an overlooked technology-production update," in *SPE Eastern Regional Meeting*, 2001: Society of Petroleum Engineers.
- [74] S. Campbell, N. Fairchild Jr, and D. Arnold, "Liquid CO₂ and sand stimulations in the lewis shale, San Juan Basin, New Mexico: A case study," in *SPE rocky mountain regional/low-permeability reservoirs symposium and exhibition*, 2000: Society of Petroleum Engineers.
- [75] M. G. Tulissi and R. E. May, "A comparison of results of three different CO₂ energized frac fluids: a case history," in *SPE Gas Technology Symposium*, 2002: Society of Petroleum Engineers.
- [76] C. Palmer and Z. Sito, "Nitrogen and carbon dioxide fracturing fluids for the stimulation of unconventional shale plays," *AGH Drilling, Oil, Gas*, vol. 30, no. 1, pp. 191--198, 2013.
- [77] L. H. Burke, G. W. Nevison, and W. E. Peters, "Improved unconventional gas recovery with energized fracturing fluids: Montney example," in *SPE Eastern Regional Meeting*, 2011: Society of Petroleum Engineers.
- [78] X. Song *et al.*, "Fracturing with carbon dioxide: from microscopic mechanism to reservoir application," *Joule*, vol. 3, no. 8, pp. 1913-1926, 2019.
- [79] D. Gupta and P. S. Carman, "Associative polymer system extends the temperature range of surfactant gel frac fluids," in *SPE International Symposium on Oilfield Chemistry*, 2011: Society of Petroleum Engineers.
- [80] J. M. Matter and P. B. Kelemen, "Permanent storage of carbon dioxide in geological reservoirs by mineral carbonation," *Nature Geoscience*, vol. 2, no. 12, pp. 837-841, 2009.
- [81] C. Fang, W. Chen, and M. Amro, "Simulation study of hydraulic fracturing using super critical CO₂ in shale," in *Abu Dhabi International Petroleum Exhibition and Conference*, 2014: Society of Petroleum Engineers.
- [82] D. Mo, B. Jia, J. Yu, N. Liu, and R. Lee, "Study nanoparticle-stabilized CO₂ foam for oil recovery at different pressure, temperature, and rock samples," in *SPE Improved Oil Recovery Symposium*, 2014: Society of Petroleum Engineers.

- [83] B. Jia, J.-S. Tsau, and R. Barati, "A review of the current progress of CO₂ injection EOR and carbon storage in shale oil reservoirs," *Fuel*, vol. 236, pp. 404-427, 2019.
- [84] H. Wang, G. Li, and Z. Shen, "A feasibility analysis on shale gas exploitation with supercritical carbon dioxide," *Energy Sources, Part A: Recovery, Utilization, and Environmental Effects*, vol. 34, no. 15, pp. 1426-1435, 2012.
- [85] Y. Jiang *et al.*, "Experimental study of supercritical CO₂ fracturing on initiation pressure and fracture propagation in shale under different triaxial stress conditions," *Journal of Natural Gas Science and Engineering*, vol. 55, pp. 382-394, 2018.
- [86] P. Pei, K. Ling, J. He, and Z. Liu, "Shale gas reservoir treatment by a CO₂-based technology," *Journal of Natural Gas Science and Engineering*, vol. 26, pp. 1595-1606, 2015.
- [87] P. Peng, Y. Ju, Y. Wang, S. Wang, and F. Gao, "Numerical analysis of the effect of natural microcracks on the supercritical CO₂ fracturing crack network of shale rock based on bonded particle models," *International Journal for Numerical and Analytical Methods in Geomechanics*, vol. 41, no. 18, pp. 1992-2013, 2017.
- [88] G.-Q. Tang* *et al.*, "An Experimental Study on Supercritical CO₂ Injection in Fractured Tight Reservoir to Enhance Oil Recovery," in *Unconventional Resources Technology Conference, San Antonio, Texas, 1-3 August 2016*, 2016: Society of Exploration Geophysicists, American Association of Petroleum ..., pp. 602-618.
- [89] W. Sun *et al.*, "Thickening Supercritical CO₂ with pi-Stacked Co-Polymers: Molecular Insights into the Role of Intermolecular Interaction," *Polymers (Basel)*, vol. 10, no. 3, Mar 6 2018, doi: 10.3390/polym10030268.
- [90] J. Zhou *et al.*, "Supercritical CO₂ fracking for enhanced shale gas recovery and CO₂ sequestration: results, status and future challenges," *Advances in Geo-Energy Research*, vol. 3, no. 2, pp. 207-224, 2019.
- [91] R. S. Middleton *et al.*, "Shale gas and non-aqueous fracturing fluids: Opportunities and challenges for supercritical CO₂," *Applied Energy*, vol. 147, pp. 500-509, 2015, doi: 10.1016/j.apenergy.2015.03.023.
- [92] J. Zhou *et al.*, "Influence of supercritical CO₂ Exposure on CH₄ and CO₂ Adsorption behaviors of shale: Implications for CO₂ Sequestration," *Energy & fuels*, vol. 32, no. 5, pp. 6073-6089, 2018.
- [93] X. Li and Y. Kang, "Enhanced shale gas recovery using supercritical carbon dioxide," *Science*, pp. 1893-2018, 2018.
- [94] T. Ishida, T. Niwa, K. Aoyagi, A. Yamakawa, Y. Chen, and D. Fukahori, "AE Monitoring of hydraulic fracturing laboratory experiment with supercritical and liquid state CO₂," in *ISRM International Symposium (EUROCK 2012)*, 2012, pp. 28-30.
- [95] S. Inui, T. Ishida, Y. Nagaya, Y. Nara, Y. Chen, and Q. Chen, "AE monitoring of hydraulic fracturing experiments in granite blocks using supercritical CO₂, water and viscous oil," in *48th US Rock Mechanics/Geomechanics Symposium*, 2014: American Rock Mechanics Association.
- [96] X. Wang, J. Wu, and J. Zhang, "Application of CO₂ fracturing technology for terrestrial shale gas reservoirs," *Nat. Gas Ind*, vol. 34, pp. 64-67, 2014.

- [97] S. Zhenyun, S. Weidong, Y. Yanzeng, L. Yong, L. Zhihang, and W. Xiaoyu, "Experimental studies of CO₂/sand dry-frac process," *Natural Gas Industry*, vol. 34, no. 6, pp. 55-59, 2014.
- [98] H.-J. Huo, R.-h. Wang, H.-J. Ni, Y.-x. Li, C.-y. Tan, and S. Xue, "Study of critical annulus up-returning velocity of cuttings carried by supercritical CO₂ in deviated well," *Journal of CO₂ Utilization*, vol. 20, pp. 105-112, 2017.
- [99] M. S. Dahayanake, J. Yang, J. H. Niu, P.-J. Derian, R. Li, and D. Dino, "Viscoelastic surfactant fluids and related methods of use," ed: Google Patents, 2001.
- [100] S. Zhang, Y. She, and Y. Gu, "Evaluation of polymers as direct thickeners for CO₂ enhanced oil recovery," *Journal of Chemical & Engineering Data*, vol. 56, no. 4, pp. 1069-1079, 2011.
- [101] P. C. Harris and S. J. Heath, "Friction reducers for fluids comprising carbon dioxide and methods of using friction reducers in fluids comprising carbon dioxide," ed: Google Patents, 2006.
- [102] H. Wang *et al.*, "Key problems and solutions in supercritical CO₂ fracturing technology," *Frontiers in Energy*, pp. 1-6, 2019.
- [103] M. Wang, K. Huang, W. Xie, and X. Dai, "Current research into the use of supercritical CO₂ technology in shale gas exploitation," *International Journal of Mining Science and Technology*, 2018, doi: 10.1016/j.ijmst.2018.05.017.
- [104] S. Rani, E. Padmanabhan, and B. K. Prusty, "Review of gas adsorption in shales for enhanced methane recovery and CO₂ storage," *Journal of Petroleum Science and Engineering*, vol. 175, pp. 634-643, 2019, doi: 10.1016/j.petrol.2018.12.081.
- [105] Q. Li, H. Xing, J. Liu, and X. Liu, "A review on hydraulic fracturing of unconventional reservoir," *Petroleum*, vol. 1, no. 1, pp. 8-15, 2015, doi: 10.1016/j.petlm.2015.03.008.
- [106] R. Barati and J.-T. Liang, "A review of fracturing fluid systems used for hydraulic fracturing of oil and gas wells," *Journal of Applied Polymer Science*, vol. 131, no. 16, pp. n/a-n/a, 2014, doi: 10.1002/app.40735.
- [107] A. Rogala, J. Krzysiek, M. Bernaciak, and J. J. P. P. o. M. P. Hupka, "Non-aqueous fracturing technologies for shale gas recovery," vol. 49, 2013.
- [108] M. S. Santos, L. F. M. Franco, M. Castier, and I. G. Economou, "Molecular Dynamics Simulation of n-Alkanes and CO₂ Confined by Calcite Nanopores," *Energy & Fuels*, vol. 32, no. 2, pp. 1934-1941, 2018, doi: 10.1021/acs.energyfuels.7b02451.
- [109] K. Zeng, P. Jiang, Z. Lun, and R. Xu, "Molecular Simulation of Carbon Dioxide and Methane Adsorption in Shale Organic Nanopores," *Energy & Fuels*, vol. 33, no. 3, pp. 1785-1796, 2018, doi: 10.1021/acs.energyfuels.8b02851.
- [110] E. Heidaryan, T. Hatami, M. Rahimi, and J. Moghadasi, "Viscosity of pure carbon dioxide at supercritical region: Measurement and correlation approach," *The Journal of Supercritical Fluids*, vol. 56, no. 2, pp. 144-151, 2011, doi: 10.1016/j.supflu.2010.12.006.
- [111] S. Rani, B. K. Prusty, and S. K. Pal, "Adsorption kinetics and diffusion modeling of CH₄ and CO₂ in Indian shales," *Fuel*, vol. 216, pp. 61-70, 2018, doi: 10.1016/j.fuel.2017.11.124.

- [112] P. Gullapalli, J.-S. Tsau, and J. P. Heller, "Gelling behavior of 12-hydroxystearic acid in organic fluids and dense CO₂," in *SPE International Symposium on Oilfield Chemistry*, 1995: Society of Petroleum Engineers.
- [113] J. DeSimone, Z. Guan, and C. Elsbernd, "Synthesis of fluoropolymers in supercritical carbon dioxide," *Science*, vol. 257, no. 5072, pp. 945-947, 1992.
- [114] R. M. Enick, E. J. Beckman, C. Shi, Z. Huang, J. Xu, and S. Kilic, "Direct thickeners for carbon dioxide," in *SPE/DOE Improved Oil Recovery Symposium*, 2000: Society of Petroleum Engineers.
- [115] G. Ramadhan, G. Hirasaki, and Q. P. Nguyen, "Foaming Behavior of CO₂-Soluble, Viscoelastic Surfactant in Homogenous Porous Media," in *SPE Improved Oil Recovery Conference*, 2018: Society of Petroleum Engineers.
- [116] J. F. Gadberry, M. D. Hoey, R. Franklin, G. del Carmen Vale, and F. Mozayeni, "Surfactants for hydraulic fracturing compositions," ed: Google Patents, 1999.
- [117] G. J. Tustin *et al.*, "Synthesis and characterisation of water soluble ferrocenes: Molecular tuning of redox potentials," *Journal of Organometallic Chemistry*, vol. 692, no. 23, pp. 5173-5182, 2007.
- [118] J. De Heer, "The principle of le chatelier and braun," *Journal of Chemical Education*, vol. 34, no. 8, p. 375, 1957.
- [119] E. Achife and J. Ibemesi, "Applicability of the Freundlich and Langmuir adsorption isotherms in the bleaching of rubber and melon seed oils," *Journal of the American Oil Chemists' Society*, vol. 66, no. 2, pp. 247-252, 1989.
- [120] Y. S. Ho, "Selection of optimum sorption isotherm," *Carbon*, vol. 42, no. 10, pp. 2115-2116, 2004.
- [121] K. Y. Foo and B. H. Hameed, "Insights into the modeling of adsorption isotherm systems," *Chemical engineering journal*, vol. 156, no. 1, pp. 2-10, 2010.
- [122] O. Redlich and D. L. Peterson, "A useful adsorption isotherm," *Journal of Physical Chemistry*, vol. 63, no. 6, pp. 1024-1024, 1959.
- [123] M. Khalfaoui, S. Knani, M. Hachicha, and A. B. Lamine, "New theoretical expressions for the five adsorption type isotherms classified by BET based on statistical physics treatment," *Journal of colloid and interface science*, vol. 263, no. 2, pp. 350-356, 2003.
- [124] C. Tien, "Adsorption Calculation and Modeling, ed," *H. Brenner*, 1994.
- [125] Z. Jin and A. Firoozabadi, "Flow of methane in shale nanopores at low and high pressure by molecular dynamics simulations," *J Chem Phys*, vol. 143, no. 10, p. 104315, Sep 14 2015, doi: 10.1063/1.4930006.
- [126] J. Bear, *Dynamics of fluids in porous media*. Courier Corporation, 2013.
- [127] M. O. Eshkalak, U. Aybar, and K. Sepehrnoori, "An economic evaluation on the re-fracturing treatment of the US shale gas resources," in *SPE Eastern Regional Meeting*, 2014: Society of Petroleum Engineers.
- [128] M. Godec, G. Koperna, R. Petrusak, and A. Oudinot, "Potential for enhanced gas recovery and CO₂ storage in the Marcellus Shale in the Eastern United States," *International Journal of Coal Geology*, vol. 118, pp. 95-104, 2013.
- [129] S. M. Kang, E. Fathi, R. J. Ambrose, I. Y. Akkutlu, and R. F. Sigal, "Carbon dioxide storage capacity of organic-rich shales," *Spe Journal*, vol. 16, no. 04, pp. 842-855, 2011.
- [130] J. Song and D. Zhang, "Comprehensive review of caprock-sealing mechanisms for geologic carbon sequestration," *Environmental science & technology*, vol. 47, no. 1, pp. 9-22, 2013.

- [131] D. Zhang and J. Song, "Mechanisms for geological carbon sequestration," *Procedia IUTAm*, vol. 10, no. 0, pp. 319-327, 2014.
- [132] S. Boosari, U. Aybar, and M. O. Eshkalak, "Carbon dioxide storage and sequestration in unconventional shale reservoirs," 2015.
- [133] Y.-B. Chang, B. K. Coats, and J. S. Nolen, "A compositional model for CO₂ floods including CO₂ solubility in water," in *Permian Basin Oil and Gas Recovery Conference*, 1996: Society of Petroleum Engineers.
- [134] E. Lindeberg and D. Wessel-Berg, "Vertical convection in an aquifer column under a gas cap of CO₂," *Energy Conversion and management*, vol. 38, pp. S229-S234, 1997.
- [135] C. A. Rochelle, I. Czernichowski-Lauriol, and A. Milodowski, "The impact of chemical reactions on CO₂ storage in geological formations: a brief review," *Geological Society, London, Special Publications*, vol. 233, no. 1, pp. 87-106, 2004.
- [136] D. N. Espinoza, S. Kim, and J. Santamarina, "CO₂ geological storage—Geotechnical implications," *KSCE Journal of Civil Engineering*, vol. 15, no. 4, pp. 707-719, 2011.
- [137] M. O. Eshkalak, E. W. Al-Shalabi, A. Sanaei, U. Aybar, and K. Sepehrnoori, "Simulation study on the CO₂-driven enhanced gas recovery with sequestration versus the re-fracturing treatment of horizontal wells in the US unconventional shale reservoirs," *Journal of Natural Gas Science and Engineering*, vol. 21, pp. 1015-1024, 2014.
- [138] J. I. Drever, *The geochemistry of natural waters*. prentice Hall Englewood Cliffs, 1988.
- [139] D. White *et al.*, "Greenhouse gas sequestration in abandoned oil reservoirs: The International Energy Agency Weyburn pilot project," *GSA today*, vol. 14, no. 7, pp. 4-10, 2004.
- [140] L. Li, C. A. Peters, and M. A. Celia, "Upscaling geochemical reaction rates using pore-scale network modeling," *Advances in water resources*, vol. 29, no. 9, pp. 1351-1370, 2006.
- [141] I. Gaus, M. Azaroual, and I. Czernichowski-Lauriol, "Reactive transport modelling of the impact of CO₂ injection on the clayey cap rock at Sleipner (North Sea)," *Chemical Geology*, vol. 217, no. 3-4, pp. 319-337, 2005.
- [142] L. Algive, S. Bekri, and O. Vizika-kavvadias, "Reactive pore network modeling dedicated to the determination of the petrophysical property changes while injecting CO₂," in *SPE annual technical conference and exhibition*, 2009: Society of Petroleum Engineers.
- [143] É. Brosse, C. Magnier, and B. Vincent, "Modelling fluid-rock interaction induced by the percolation of CO₂-enriched solutions in core samples: the role of reactive surface area," *Oil & gas science and technology*, vol. 60, no. 2, pp. 287-305, 2005.
- [144] U. Aybar, W. Yu, M. O. Eshkalak, K. Sepehrnoori, and T. Patzek, "Evaluation of production losses from unconventional shale reservoirs," *Journal of Natural Gas Science and Engineering*, vol. 23, pp. 509-516, 2015.
- [145] U. Aybar, "Investigation of analytical models incorporating geomechanical effects on production performance of hydraulically and naturally fractured unconventional reservoirs," 2014.

- [146] H. de Coninck and S. M. Benson, "Carbon Dioxide Capture and Storage: Issues and Prospects," *Annual Review of Environment and Resources*, vol. 39, no. 1, pp. 243-270, 2014, doi: 10.1146/annurev-environ-032112-095222.
- [147] Z. Tao and A. Clarens, "Estimating the carbon sequestration capacity of shale formations using methane production rates," *Environ Sci Technol*, vol. 47, no. 19, pp. 11318-25, Oct 1 2013, doi: 10.1021/es401221j.
- [148] H. T. Schaef *et al.*, "CO₂ utilization and storage in shale gas reservoirs: experimental results and economic impacts," *Energy Procedia*, vol. 63, pp. 7844-7851, 2014.
- [149] S. Mery and C. Sinayuc, "Analysis of carbon dioxide sequestration in shale gas reservoirs by using experimental adsorption data and adsorption models," *Journal of Natural Gas Science and Engineering*, vol. 36, pp. 1087-1105, 2016.
- [150] J. Mullen, "Petrophysical characterization of the Eagle Ford Shale in south Texas," in *Canadian Unconventional Resources and International Petroleum Conference*, 2010: Society of Petroleum Engineers.
- [151] J. McLennan, J. Roegiers, and W. Marx, "The Mancos Formation: an evaluation of the interaction of geological conditions, treatment characteristics and production," in *SPE/DOE Low Permeability Gas Reservoirs Symposium*, 1983: Society of Petroleum Engineers.
- [152] M. A. Engle *et al.*, "Geochemistry of formation waters from the Wolfcamp and "Cline" shales: Insights into brine origin, reservoir connectivity, and fluid flow in the Permian Basin, USA," *Chemical Geology*, vol. 425, pp. 76-92, 2016.
- [153] H.-J. Lehmler, V. R. Rao, D. Nauduri, J. D. Vargo, and S. Parkin, "Synthesis and structure of environmentally relevant perfluorinated sulfonamides," *Journal of fluorine chemistry*, vol. 128, no. 6, pp. 595-607, 2007.
- [154] P. J. Linstrom and W. G. Mallard, "The NIST Chemistry WebBook: A chemical data resource on the internet," *Journal of Chemical & Engineering Data*, vol. 46, no. 5, pp. 1059-1063, 2001.
- [155] M. Ayers, "ChemSpider: the free chemical database," *Reference Reviews*, 2012.
- [156] S. Kim *et al.*, "PubChem 2019 update: improved access to chemical data," *Nucleic acids research*, vol. 47, no. D1, pp. D1102-D1109, 2019.
- [157] G.-J. Janssen, "Information on the FESEM (Field-emission Scanning Electron Microscope)," 2010.
- [158] S. Talapatra, "Investigation of Antimicrobial Potential of Nisin Against *Bacillus thuringiensis*," 2015.
- [159] C. R. Brundle, C. A. Evans, and S. Wilson, *Encyclopedia of materials characterization: surfaces, interfaces, thin films*. Gulf Professional Publishing, 1992.
- [160] S. Kemp, G. Turner, and D. Wagner, "Initial testing and a laboratory manual for the Micromeritics Gemini VI physisorption system," 2009.
- [161] O. Torsæter and M. Abtahi, "Experimental reservoir engineering laboratory workbook," *Department of Petroleum Engineering and Applied Geophysics, Norwegian University of Science and Technology (NTNU), Trondheim*, 2003.
- [162] G. L. P. de Oliveira *et al.*, "Pore volume compressibilities of sandstones and carbonates from Helium porosimetry measurements," *Journal of Petroleum Science and Engineering*, vol. 137, pp. 185-201, 2016.

- [163] K. A. Babatunde, "Molecular Simulation Study of CO₂/CH₄ Adsorption on Realistic Heterogeneous Shale Surfaces," *Applied Surface Science*, p. 148789, 2020.
- [164] P. Ungerer, J. Collell, and M. Yiannourakou, "Molecular modeling of the volumetric and thermodynamic properties of kerogen: Influence of organic type and maturity," *Energy & Fuels*, vol. 29, no. 1, pp. 91-105, 2015.
- [165] S. Wang, Q. Feng, M. Zha, F. Javadpour, and Q. Hu, "Supercritical methane diffusion in shale nanopores: effects of pressure, mineral types, and moisture content," *Energy & fuels*, vol. 32, no. 1, pp. 169-180, 2018.
- [166] A. F. Gualtieri *et al.*, "Structural characterization of the clay mineral illite-1M," *Journal of Applied Crystallography*, vol. 41, no. 2, pp. 402-415, 2008.
- [167] A. T. Brünger and M. Nilges, "Computational challenges for macromolecular structure determination by X-ray crystallography and solution NMR spectroscopy," *Quarterly reviews of biophysics*, vol. 26, no. 1, pp. 49-125, 1993.
- [168] M. Meunier, "Introduction to materials studio," in *EPJ Web of Conferences*, 2012, vol. 30: EDP Sciences, p. 04001.
- [169] H. Sun, P. Ren, and J. Fried, "The COMPASS force field: parameterization and validation for phosphazenes," *Computational and Theoretical Polymer Science*, vol. 8, no. 1-2, pp. 229-246, 1998.
- [170] A. K. Rappé, C. J. Casewit, K. Colwell, W. A. Goddard III, and W. M. Skiff, "UFF, a full periodic table force field for molecular mechanics and molecular dynamics simulations," *Journal of the American chemical society*, vol. 114, no. 25, pp. 10024-10035, 1992.
- [171] A. Rappe, K. Colwell, and C. Casewit, "Application of a universal force field to metal complexes," *Inorganic Chemistry*, vol. 32, no. 16, pp. 3438-3450, 1993.
- [172] L. Jaillet, S. Artemova, and S. Redon, "IM-UFF: Extending the universal force field for interactive molecular modeling," *Journal of Molecular Graphics and Modelling*, vol. 77, pp. 350-362, 2017.
- [173] M. F. Schlecht, *Molecular Modeling on the PC with 3.5 Disk*. John Wiley & Sons, Inc., 1998.
- [174] A. H. Farmahini, "Molecular dynamics simulation studies of piperazine activated MDEA absorption solution with methane and carbon dioxide," The University of Bergen, 2010.
- [175] N. Harun and E. E. Masiren, "Molecular dynamic simulation of CO₂ absorption into mixed aqueous solutions MDEA/PZ," *Chemical Engineering Research Bulletin*, pp. 1-11, 2017.
- [176] T. Darden, D. York, and L. Pedersen, "Particle mesh Ewald: An N · log (N) method for Ewald sums in large systems," *The Journal of chemical physics*, vol. 98, no. 12, pp. 10089-10092, 1993.
- [177] A. T. Brünger, *X-PLOR: version 3.1: a system for x-ray crystallography and NMR*. Yale University Press, 1992.
- [178] Y. Xiong and E. Kiran, "Miscibility, density and viscosity of poly (dimethylsiloxane) in supercritical carbon dioxide," *Polymer*, vol. 36, no. 25, pp. 4817-4826, 1995.

- [179] X.-Q. Liu *et al.*, "Molecular simulation of CH₄, CO₂, H₂O and N₂ molecules adsorption on heterogeneous surface models of coal," *Applied Surface Science*, vol. 389, pp. 894-905, 2016.
- [180] H. Sui, F. Zhang, Z. Wang, D. Wang, and Y. Wang, "Effect of Kerogen Maturity, Water Content for Carbon Dioxide, Methane, and Their Mixture Adsorption and Diffusion in Kerogen: A Computational Investigation," *Langmuir*, vol. 36, no. 33, pp. 9756-9769, 2020.
- [181] T. F. Rexer, E. J. Mathia, A. C. Aplin, and K. M. Thomas, "High-pressure methane adsorption and characterization of pores in Posidonia shales and isolated kerogens," *Energy & Fuels*, vol. 28, no. 5, pp. 2886-2901, 2014.
- [182] S. Liu, B. Sun, J. Xu, H. Li, and X. Wang, "Study on Competitive Adsorption and Displacing Properties of CO₂ Enhanced Shale Gas Recovery: Advances and Challenges," *Geofluids*, vol. 2020, 2020.
- [183] J. W. Gibbs, "The collected works of J. Willard Gibbs," Yale Univ. Press, 1948.
- [184] J. G. Speight, *Shale gas production processes*. Gulf Professional Publishing, 2013.
- [185] L. Huang *et al.*, "Molecular simulation of adsorption behaviors of methane, carbon dioxide and their mixtures on kerogen: effect of kerogen maturity and moisture content," *Fuel*, vol. 211, pp. 159-172, 2018.
- [186] Y. Liu, J. Hou, and C. Wang, "Absolute adsorption of CH₄ on shale with the simplified local-density theory," *SPE Journal*, vol. 25, no. 01, pp. 212-225, 2020.
- [187] R. Aguilera, "Shale gas reservoirs: Theoretical, practical and research issues," *Petroleum Research*, vol. 1, no. 1, pp. 10-26, 2016.
- [188] F. P. Wang and R. M. Reed, "Pore Networks and Fluid Flow in Gas Shales," presented at the SPE Annual Technical Conference and Exhibition, New Orleans, Louisiana, 2009/1/1/, 2009. [Online]. Available: <https://doi.org/10.2118/124253-MS>.
- [189] W. Acree Jr and J. S. Chickos, "Phase transition enthalpy measurements of organic and organometallic compounds. Sublimation, vaporization and fusion enthalpies from 1880 to 2010," *Journal of Physical and Chemical Reference Data*, vol. 39, no. 4, p. 043101, 2010.
- [190] A. K. Rappe, C. J. Casewit, K. S. Colwell, W. A. Goddard, and W. M. Skiff, "UFF, a full periodic table force field for molecular mechanics and molecular dynamics simulations," *Journal of the American Chemical Society*, vol. 114, no. 25, pp. 10024-10035, 1992/12/01 1992, doi: 10.1021/ja00051a040.
- [191] D. Barthelmy, "Mineralogy database, webmineral," *Online under*, <http://www.webmineral.com>, 2007.
- [192] P. J. Flory, "Molecular size distribution in three dimensional polymers. I. Gelation1," *Journal of the American Chemical Society*, vol. 63, no. 11, pp. 3083-3090, 1941.
- [193] M. L. Huggins, "The viscosity of dilute solutions of long-chain molecules. IV. Dependence on concentration," *Journal of the American Chemical Society*, vol. 64, no. 11, pp. 2716-2718, 1942.
- [194] D. J. Kozuch, W. Zhang, and S. T. Milner, "Predicting the Flory-Huggins χ parameter for polymers with stiffness mismatch from molecular dynamics simulations," *Polymers*, vol. 8, no. 6, p. 241, 2016.

- [195] H. Lin and B. D. Freeman, "Gas and vapor solubility in cross-linked poly (ethylene glycol diacrylate)," *Macromolecules*, vol. 38, no. 20, pp. 8394-8407, 2005.
- [196] R. A. Orwoll and P. A. Arnold, "Polymer–solvent interaction parameter χ ," in *Physical properties of polymers handbook*: Springer, 2007, pp. 233-257.
- [197] Y. Zhou, H. Ni, Z. Shen, and M. Wang, "Study on proppant transport in fractures of supercritical carbon dioxide fracturing," *Energy & Fuels*, vol. 34, no. 5, pp. 6186-6196, 2020.
- [198] B. Sun, J. Wang, Z. Wang, Y. Gao, and J. Xu, "Calculation of proppant-carrying flow in supercritical carbon dioxide fracturing fluid," *Journal of Petroleum Science and Engineering*, vol. 166, pp. 420-432, 2018.
- [199] J. Peach and J. Eastoe, "Supercritical carbon dioxide: a solvent like no other," *Beilstein journal of organic chemistry*, vol. 10, no. 1, pp. 1878-1895, 2014.
- [200] Y. Zhao, J. Zhang, B. Han, J. Song, J. Li, and Q. Wang, "Metal–organic framework nanospheres with well-ordered mesopores synthesized in an ionic liquid/CO₂/surfactant system," *Angewandte Chemie International Edition*, vol. 50, no. 3, pp. 636-639, 2011.
- [201] X. Sun, X. Liang, S. Wang, and Y. Lu, "Experimental study on the rheology of CO₂ viscoelastic surfactant foam fracturing fluid," *Journal of Petroleum Science and Engineering*, vol. 119, pp. 104-111, 2014.
- [202] E. M. M. Khair, Z. Shicheng, M. Shanbo, and Z. Mei, "Performance and application of new anionic D3F-AS05 viscoelastic fracturing fluid," *Journal of Petroleum Science and Engineering*, vol. 78, no. 1, pp. 131-138, 2011.
- [203] S. Ahmed, K. A. Elraies, M. R. Hashmet, and M. S. Alnarabiji, "Empirical modeling of the viscosity of supercritical carbon dioxide foam fracturing fluid under different downhole conditions," *Energies*, vol. 11, no. 4, p. 782, 2018.
- [204] C. Chen, J. Sun, Y. Zhang, J. Mu, W. Li, and Y. Song, "Adsorption characteristics of CH₄ and CO₂ in organic-inorganic slit pores," *Fuel*, vol. 265, p. 116969, 2020.
- [205] J. Tan *et al.*, "Shale gas potential of the major marine shale formations in the Upper Yangtze Platform, South China, Part II: Methane sorption capacity," *Fuel*, vol. 129, pp. 204-218, 2014.
- [206] T. Wang *et al.*, "Experimental study of water vapor adsorption behaviors on shale," *Fuel*, vol. 248, pp. 168-177, 2019.